NASA Technical Memorandum 103962

# Navier-Stokes Simulations of Unsteady Transonic Flow Phenomena

C. A. Atwood, Ames Research Center, Moffett Field, California

August 1992

National Aeronautics and
Space Administration

**Ames Research Center**
Moffett Field, California 94035-1000

# Abstract

Numerical simulation of two classes of unsteady flows are obtained via the Navier-Stokes equations: a blast-wave/target interaction problem class and a transonic cavity flow problem class. The method developed for the viscous blast-wave/target interaction problem assumes a laminar, perfect gas implemented in a structured finite-volume framework. The approximately factored implicit scheme uses Newton subiterations to obtain the spatially and temporally second-order accurate time history of the interaction of blast-waves with stationary targets. The inviscid flux is evaluated using either of two upwind techniques, while the full viscous terms are computed by central differencing. Comparisons of unsteady numerical, analytical, and experimental results are made in two- and three-dimensions for Couette flows, a starting shock-tunnel, and a shock-tube blockage study. The results show accurate wave speed resolution and nonoscillatory discontinuity capturing of the predominantly inviscid flows. Viscous effects were increasingly significant at large post-interaction times.

While the blast-wave/target interaction problem benefits from high-resolution methods applied to the Euler terms, the transonic cavity flow problem requires the use of an efficient scheme implemented in a geometrically flexible overset mesh environment. Hence, the Reynolds averaged Navier-Stokes equations implemented in a diagonal form are applied to the cavity flow class of problems. Comparisons between numerical and experimental results are made in two-dimensions for free shear layers and both rectangular and quieted cavities, and in three-dimensions for Stratospheric Observatory For Infrared Astronomy (SOFIA) geometries. The acoustic behavior of the rectangular and three-dimensional cavity flows compare well with experiment in terms of frequency, magnitude, and quieting trends. However, there is a more rapid

decrease in computed acoustic energy with frequency than observed experimentally owing to numerical dissipation. In addition, optical phase distortion due to the time-varying density field is modelled using geometrical constructs. The computed optical distortion trends compare with the experimentally inferred result, but underpredicts the fluctuating phase difference magnitude.

# Acknowledgements

My thanks are extended to Professor R.W. MacCormack, whose blend of personal warmth and clarity of thought rejuvenated my interest in computational physics. Drs. T.L. Holst and W.R. Van Dalsem have earned my gratitude for granting me the opportunity to grow in the superlative research environment of the Applied Computational Fluids Branch. My appreciation is also due to the members of the branch who have offered their standards, support, and even critical feedback, thus shaping my abilities as an engineer and scientist. Most importantly, I am indebted to my family and friends for instilling the values which provide the motive drive underneath my efforts.

This research, performed at Stanford University and NASA Ames Research Center, was supported by grants NCC-2-540 and NCC-2-677.

# Nomenclature

| | |
|---|---|
| $A, B, C$ | inviscid flux Jacobians |
| $c$ | speed of sound |
| $c_p, c_v$ | specific heats at constant pressure and volume |
| $C_p$ | coefficient of pressure, $\frac{p-p_\infty}{q_\infty}$ |
| $< C'_p >$ | fluctuating coefficient of pressure, $\left[\frac{1}{N}\sum_i^N\left(\frac{p'_i}{q_\infty}\right)^2\right]^{\frac{1}{2}}$ |
| $e$ | total energy per unit volume |
| $E, F, G$ | flux vectors |
| $f$ | frequency |
| $\vec{F}$ | flux tensor of second order |
| $h$ | enthalpy per unit mass |
| $\mathbf{i}, \mathbf{j}, \mathbf{k}$ | Cartesian unit vectors |
| $J$ | coordinate transformation Jacobian |
| $k$ | coefficient of thermal conductivity or wave number, $\frac{2\pi}{\lambda}$ |
| $K$ | ratio of convection by freestream speed |
| $L$ | characteristic length |
| $m$ | stage number |
| $\dot{m}$ | mass flow rate |
| $M$ | Mach number or viscous flux Jacobian |
| $n$ | index of refraction |
| $\mathbf{n}$ | surface normal |
| $OPD$, $OPL$ | optical path difference, length |
| $p$ | instantaneous static pressure |
| $Pr$ | Prandtl number |

| | |
|---|---|
| $PSD$ | power spectral density, $dB$ |
| $q$ | velocity magnitude or dynamic pressure |
| $\mathbf{q}$ | heat transfer vector |
| $Q$ | vector of dependent variables |
| $r$ | velocity ratio, $\frac{u_1}{u_2}$ |
| $\mathbf{r}$ | position vector in physical space |
| $R$ | specific gas constant |
| $Re$ | Reynolds number |
| $\mathbf{s}$ | outward-directed surface normal |
| $s_x, s_y, s_z$ | Cartesian components of surface normal |
| $St$ | Strouhal number, $\frac{f\theta}{u_1+u_2}$ |
| $SPL$ | sound power level, $dB$ |
| $t$ | time |
| $\mathbf{t}$ | tangential |
| $T$ | absolute temperature |
| $T^{-1}, T$ | matrices of left and right eigenvectors or of the transformation |
| $u, v, w$ | Cartesian velocity components or parametric surface coordinates |
| $U, V, W$ | contravariant velocity components |
| $\mathcal{V}$ | cell volume |
| $x, y, z$ | Cartesian physical space coordinates |
| Å | angstrom, $10^{-10}\ m$ |
| $\alpha$ | angle of attack |
| $\beta$ | compression parameter, or the Gladstone-Dale constant, $(n-1)_{STP}$ |
| $\gamma$ | ratio of specific heats |
| $\epsilon$ | internal energy per unit mass |
| $\zeta$ | bulk coefficient of viscosity |
| $\theta$ | angle subtending the ray and surface normal or momentum thickness |
| $\kappa$ | ratio of coefficient of thermal conductivity to the specific heat at constant volume |
| $\lambda$ | eigenvalue, second coefficient of viscosity, or wavelength |
| $\Lambda$ | diagonal matrix of eigenvalues, $\lambda_i$ |

| | |
|---|---|
| $\mu$ | dynamic or first coefficient of viscosity |
| $\nu$ | Courant-Friedrichs-Lewy number |
| $\xi, \eta, \zeta$ | curvilinear space coordinates |
| $\rho$ | density |
| $\sigma$ | spreading rate parameter |
| $\tau$ | computational temporal coordinate |
| $\tau_{ij}$ | viscous stress tensor |
| $\phi$ | flux influence parameter |
| $\overline{(\ )}$ | mean quantity |
| $<\ >$ | root mean square quantity |
| $(\ )'$ | fluctuating quantity, $f = \overline{f} + f'$ |
| $(\tilde{\ })$ | dimensional quantity |

**Superscripts**

| | |
|---|---|
| $j$ | wave family |
| $m$ | subiteration level |
| $n$ | time level |

**Subscripts**

| | |
|---|---|
| $BL$ | Baldwin-Lomax |
| $i, j, k$ | $\xi, \eta, \zeta$ direction indices |
| $i$ | incident |
| $n$ | normal |
| $NS$ | Navier-Stokes |
| $r$ | refracted |
| $STP$ | standard temperature and pressure |
| $T$ | total quantity |
| $TL$ | Thin-Layer |
| $x, y, z$ | partial with respect to Cartesian coordinate |
| $\xi, \eta, \zeta$ | partial with respect to curvilinear coordinate |
| $\infty$ | freestream quantity |

# Contents

**Abstract** iii

**Acknowledgements** v

**Nomenclature** vii

**1 Introduction** 1
- 1.1.1 Blast-Wave Problem 2
- 1.1.2 Cavity Flow Effort 4
- 1.1.3 Aero-Optics Work 6

**2 Numerical Method** 9
- 2.1 The Governing Equations 9
- 2.2 Turbulence Model 12
- 2.3 Transformation to Curvilinear Coordinates 15
- 2.4 Upwind Schemes 20
  - 2.4.1 Flux Vector Splitting 22
  - 2.4.2 Flux Difference Splitting 24
  - 2.4.3 Roe Averaging 26
  - 2.4.4 Higher-Order Extensions 26
  - 2.4.5 Viscous Terms 29
  - 2.4.6 Factorization 31
  - 2.4.7 Newton Iterative Technique 32
- 2.5 Diagonal Scheme 34

2.6 Geometry Treatment . . . 35

**3 Boundary Conditions** **39**

**4 Geometrical Aero-Optics** **45**

**5 Results and Discussion** **50**

5.1 Blast-Wave Results . . . 50

5.1.1 Couette Flow . . . 50

5.1.2 Shock Tunnel Start-up Problem . . . 51

5.1.3 Shock Tube Blockage Study . . . 54

5.2 Cavity Flow Results . . . 64

5.2.1 Free Shear Layer . . . 64

5.2.2 Two-Dimensional Rectangular Cavity . . . 65

5.2.3 Two-Dimensional Treated Cavity . . . 72

5.2.4 2-D Treated Cavity: Aero-Optical Effects . . . 78

5.2.5 Clean Configuration . . . 87

5.2.6 Configuration 25 . . . 88

5.2.7 Configuration 100 . . . 93

5.2.8 Configuration 100: Aero-Optical Effects . . . 101

**6 Conclusions** **105**

6.1.1 Blast-Wave Problem . . . 105

6.1.2 Cavity Flow Problem . . . 106

6.1.3 Aero-Optical Effort . . . 106

6.1.4 Future Directions . . . 107

**Bibliography** **108**

# List of Figures

1 Proposed Large Blast/Thermal Simulator facility [1] . . . . . . . . . . . 2
2 Artist's concept of the SOFIA configuration . . . . . . . . . . . . . . . 4
3 Hexahedral cell and stencil . . . . . . . . . . . . . . . . . . . . . . . 17
4 Riemann problem schematic . . . . . . . . . . . . . . . . . . . . . . . 24
5 Geometry acquisition: (a) model, (b) laser digitized configuration, and (c) grids . . . . . . . . . . . . . . . . . . . . . . . . . . . . . . 36
6 Flux computation at a cell face or wall . . . . . . . . . . . . . . . . 39
7 Geometric optics: (a) partitioning of hexahedrons into tetrahedrons, and (b) intersection and refraction procedure . . . . . . . . . . . . . 46
8 Couette flow case: (a) impulsively started and (b) oscillating plate . . 51
9 Shock tunnel case: 300 × 60 cell grid . . . . . . . . . . . . . . . . . 52
10 Shock tunnel case: shadowgraph comparison for a Mach 3 planar shock 53
11 Hemicylinder case: experimental configuration and pressure transducer locations . . . . . . . . . . . . . . . . . . . . . . . . . . . . . . 55
12 Hemicylinder case: central region of the 78 × 50 × 25 cell (a) inviscid and (b) viscous grids . . . . . . . . . . . . . . . . . . . . . . . . . 56
13 Hemicylinder case: symmetry plane of the central part of the viscous grid . . . . . . . . . . . . . . . . . . . . . . . . . . . . . . . . . 57
14 Hemicylinder case: experimental [91] and inviscid computation pressure histories . . . . . . . . . . . . . . . . . . . . . . . . . . . . . 59
15 Hemicylinder case: experimental [91] and viscous computation pressure histories . . . . . . . . . . . . . . . . . . . . . . . . . . . . . 60

16 Viscous hemicylinder case: symmetry plane pressure [atm.] and Mach contours at (a) t=1.1ms, (b) t=1.7ms, and (c) t=6.2ms 61

17 Viscous hemicylinder case: instantaneous streamlines at (a) t=1.1ms, (b) t=1.7ms, and (c) t=6.2ms 62

18 Hemicylinder case: schematic of shock interaction 63

19 Shear layer case: (a) velocity profiles of differing grid resolution compared to similarity and (b) variation of spread rate with velocity parameter 65

20 2-d cavity: topology and grids 66

21 2-d cavity: instantaneous Mach number and pressure [kPa] contours 67

22 Rossiter's feedback model 69

23 2-d cavity: pressure history and power spectra comparison 70

24 2-d cavity: variation of mean and oscillatory pressures 71

25 Comparison of experimental and numerical schlieren images with knife edge vertical 72

26 U.S. Army Airborne Optical Adjunct [94] 73

27 2-d treated cavity: near field grids 74

28 Streamfunction near a stagnation region 75

29 2-d treated cavity: instantaneous Mach number contours and mean profiles at (a) low and (b) high lip-blowing rate 77

30 2-d treated cavity: power spectra, low lip-blowing rate 79

31 2-d treated cavity: power spectra, high lip-blowing rate 80

32 2-d treated cavity: mean and oscillatory coefficients of pressure 81

33 2-d treated cavity: $\frac{<\rho'>}{\rho_\infty}$ profiles with (a) low and (b) high lip-blowing 82

34 2-d treated cavity, low lip-blowing rate: instantaneous contours of (a) $\frac{\rho'}{\rho_\infty}$ and (b) $\frac{\rho}{\rho_\infty}$ with schematic of optical model 83

35 2-d treated cavity: contours of $OPD'(x,t)[\ in.]$ along aperture, low lip-blowing rate 83

36 2-d treated cavity: streamwise variation of optical path difference quantities 85

37 Clean configuration: pressure coefficient comparison 89

38 Configuration 25: wind tunnel and numerical models . . . . . . . . . . 90
39 Configuration 25: Mach number contours at y=0 . . . . . . . . . . . . 90
40 Configuration 25: pressure histories and power spectra . . . . . . . . . 91
41 Comparison of sound pressure levels . . . . . . . . . . . . . . . . . . . . 92
42 Telescope location and grids . . . . . . . . . . . . . . . . . . . . . . . . 94
43 Configuration 100: cavity region topology . . . . . . . . . . . . . . . . . 95
44 Configuration 100: instantaneous Mach number contours and mean profiles . . . . . . . . . . . . . . . . . . . . . . . . . . . . . . . . . . . . 96
45 Configuration 100: streamlines along the treated aperture . . . . . . . . 96
46 Experimentally [16] observed surface flow pattern . . . . . . . . . . . . 97
47 Configuration 100: pressure history and power spectra on cavity wall 98
48 Configuration 100: pressure history and power spectra on primary mirror 99
49 Configuration 100: pressure history and power spectra on secondary mirror . . . . . . . . . . . . . . . . . . . . . . . . . . . . . . . . . . . . 100
50 Configuration 100: instantaneous density field and optical refraction model . . . . . . . . . . . . . . . . . . . . . . . . . . . . . . . . . . . . 102
51 Configuration 100: density fluctuation at crossflow center of aperture 103
52 Configuration 100: comparison of wavefront distortion . . . . . . . . . 104

# Chapter 1

# Introduction

Performance envelopes of vehicles and structures which interact with the atmosphere are often limited by unsteady aerodynamic effects. Specific examples which are addressed here range from the blast-wave/target interaction problem, where peak overpressures are many times quiescent conditions, to the seeing problem, where density fluctuations contribute to image degradation. Only recently have advances in computing power and numerical algorithms provided the potential, complementary to experimental studies, for the timely design of effective configurations. However, the use of unsteady computations in the design phase is presently at an immature stage of development. The objective of this effort is to demonstrate computational technologies as applied to current topics of interest in the unsteady, compressible perfect gas regime. It is hoped that, through comparison to accepted experimental data, computational methods can make significant contributions to the design of systems which interact with unsteady flows.

In these studies, two solution methods to the Navier-Stokes equations are presented and applied to several test cases. The cases pertain to the blast-wave/target interaction or the transonic cavity flow problem classes. The method used to model the strongly unsteady blast-wave flows concentrates on resolution of the complex physics through the use of characteristic-based schemes. In contrast, for the transonic cavity flow problem, the combination of complex geometries and large problem size requires the use of an efficient integration scheme. Comparison of the numerical and experimental results will provide a reference base of unsteady numerical results for use in configuration design.

### 1.1.1 Blast-Wave Problem

The study of the effects of blast-wave impingement upon vehicles and structures is of practical consideration in the determination of their survivability. The experimental study of the blast-wave/target interaction problem requires the use of expensive above ground tests or facilities such as the U.S. Army Large Blast/Thermal Simulator (LB/TS) facility depicted in Fig. 1. Moreover, experiments can suffer from limited phase durations, and deduction of the physics of the flowfield is difficult because of practicalities in data acquisition methods. Visualization of the propagating wavefronts allows separation of pressure peaks due to wave reflection from shock tube walls from the pressure history. These pressure spikes can then, for example, be removed from structural frequency excitation analyses. Therefore, the information obtained via numerical simulation can be used for design from dynamic similitude conditions, and to augment data obtained in the test facilities.

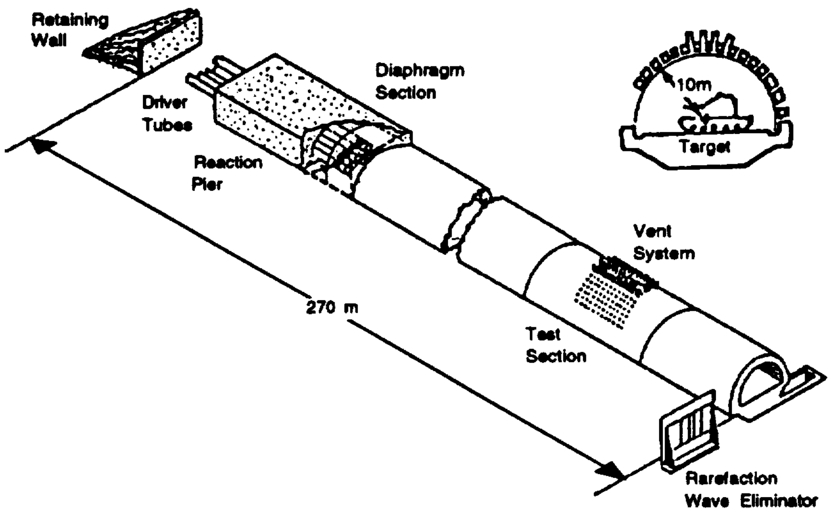

Figure 1: Proposed Large Blast/Thermal Simulator facility [1]

The simulation of the blast-wave problem has been studied in varying degrees of physical complexity, from self-similar Euler to two-dimensional viscous flows. The simulation of the blast-wave problem using the Euler equations was studied by Kutler, Sakell, and Aiello [2] in 1975, where the intersection of a planar shock with a wedge in supersonic flight was modelled using the MacCormack scheme [3]. The self-similar nature of these types of flow with respect to time was used to obtain two- and later three-dimensional cone solutions [4]. In addition, Kutler and Shankar [5] used a shock-fitting procedure for the regular diffraction of a planar shock by a wedge, which is also self-similar. Although good results can be obtained using discontinuity fitting methods, coding complexities have generally hindered their application for complex situations.

A general solution of the truly time-dependent inviscid interaction problem was modelled by Champney, Chaussee, and Kutler [6] in 1982. Shock diffraction over several simple two- and three-dimensional geometries were presented using the MacCormack and Beam-Warming schemes [7]. Mark and Kutler [8] performed a two-dimensional simulation of a shock passing over a simplified profile of a truck. However, inaccuracies due to discontinuity smearing and oscillations led to the development and application of explicit and implicit high-resolution schemes in the mid-1980's. Several two-dimensional problems using these high-resolution methods were presented by Yee [9] and Hisley and Molvik [10]. Recently, Löhner [11] has obtained solutions for complex geometries via an adaptive unstructured approach. The geometric flexibility of an unstructured grid method offers great potential, however the use of stretched tetrahedral grids required for efficient computation of viscous flows is a current topic of research.

The solution of the Navier-Stokes equations in the high Reynolds number regime requires the use of fine grids to resolve thin viscous layers. The concomitant stiffness arising from the difference in length scales suggests the use of implicit schemes. Bennett, Abbett, and Wolf [12] applied a Beam-Warming scheme [7] with the Baldwin-Lomax [13] turbulence model to the problems of a developing boundary-layer behind a moving shock and shock diffraction over a cylinder. Molvik [14] used implicit high-resolution methods to obtain two-dimensional solutions for the unsteady development of a boundary-layer, the cylinder diffraction problem, and intersection of a planar shock with a missile in supersonic flight.

The purpose of this effort is to address the general three-dimensional, viscous blast-wave problem. The techniques developed here utilize total variation diminishing (TVD) upwind and upwind-biased schemes to resolve the discontinuous flow features without the oscillations prevalent in the more conventional central difference methods. Wave speeds are resolved adequately at large Courant numbers through the use of time conservative differencing and Newton subiterations.

### 1.1.2 Cavity Flow Effort

The Stratospheric Observatory For Infrared Astronomy (SOFIA) will be a three meter class Cassegrain telescope which utilizes a Boeing 747SP as an observation platform. An artist's concept of the observatory, which is a follow-on to the Kuiper Airborne Observatory, is shown in Fig. 2. This airborne system, currently being studied by the United States' NASA and Germany's DARA, offers capabilities which augment land and space-based options in several ways. First, the mission flexibility of a long-range mobile platform lends astronomers freedom to investigate transient astronomical phenomena on a global basis. Second, atmospheric attenuation of some wavelengths of interest provide motivation for a platform which operates above the tropopause. Third, the cost of maintaining and upgrading observation technologies is lower than would be incurred with an orbiting configuration.

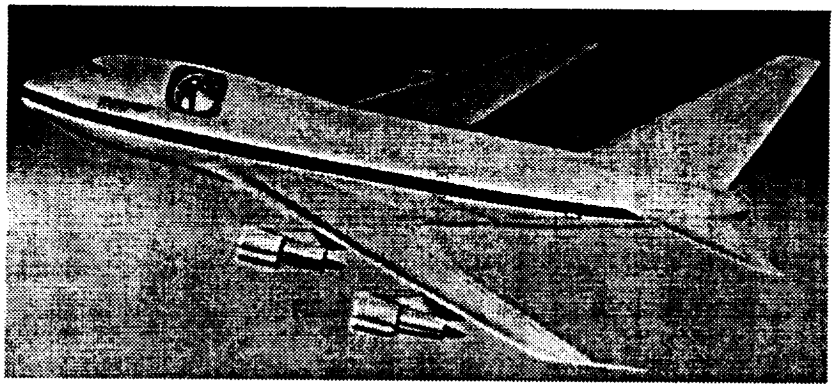

Figure 2: Artist's concept of the SOFIA configuration

Nevertheless, the use of an aircraft-based observatory presents some challenges. The limited bandwidth of solid materials in the infrared frequency ranges of interest preclude their use as windows. The temperature of the window material would also contribute to background radiation levels. Therefore, the telescope cavity must remain open to the freestream. Empirical evidence has shown that violent shear layer oscillations with concomitantly dangerous levels of acoustic loading occur for untreated, or rectangularly shaped, open cavity configurations [15, 16]. Hence, there is a need to develop cavity flow control treatments to suppress the flow unsteadiness, both to reduce the risk of injury to the crew and to obtain high-quality seeing. Towards these objectives, both experimental and computational fluid dynamics (EFD and CFD) analyses will be used in the design cycle. The purpose of this work is to develop and apply numerical tools for use in the design of the next generation airborne observatory.

The driven cavity problem has been a subject of much research, both experimental [15-29] and numerical [30-40], owing to its wide practical applicability. The buffeting and sound production of bomb bays, slotted wind-tunnel walls, transition-delaying airfoil cavities, and deflected control surfaces are examples of the range of problems. The effort here is focused upon the transonic regime, and previous efforts in these flow speeds are reviewed by Komerath, Ajuha, and Chambers [41] and Rockwell and Naudascher [42]. Some of the research which is pertinent to the transonic aero-window problem is highlighted below.

In 1955, Karamcheti [17] studied subsonic and low supersonic flow over rectangular cavities, in which the inverse relationship between cavity length, L, and dominant resonant frequency, as well the acoustic intensity and radiation directivity was reported. In the same year, Roshko [18] documented skin friction and pressure distribution along the cavity walls. The three-dimensional low subsonic study of Maull and East [20] showed that spanwise cells can modestly perturb $C_p$ distributions from the idealized infinitely wide cavity. Rossiter [15], in 1964, related cavity resonance to the edge-tone phenomenon, and deduced a model applicable to the transonic regime of concern here. In this study, Rossiter also demonstrated that a cavity leading edge spoiler drastically reduced acoustic levels. The work of Heller and Bliss [24] demonstrated that the cavity feedback mechanism can also be suppressed by geometry modifications at the shear layer impingement region. These wind tunnel tests have provided valuable insight into the governing flow mechanisms, but dynamic similitude was typically not achieved. The dangerous behavior of cavity flows generally precludes the use of flight tests to verify scaling laws. Numerical simulation offers the potential for safely scaling sub-scale tests to flight conditions.

Toward this objective, numerical efforts of the type which can model the viscous flowfield about a geometrically complicated structure was begun in 1979 by Hankey and Shang [30]. Using MacCormack's scheme, the dominant resonant mode of a rectangular cavity was accurately predicted. Om [37] used the same scheme to compute flow about quieted two-dimensional cavities. In 1987, Suhs [34] used a block implicit scheme to obtain the viscous flow about a parallelepiped cutout. The overset mesh method which was the precursor to that used herein was utilized. Dougherty et al. [39] have recently completed a detailed study of two-dimensional cavities using a high resolution scheme. They computed distinct spectral peaks which have been observed experimentally.

The present effort builds on past numerical studies by validating the ability to predict free shear layers, and both untreated and treated two- and three-dimensional cavity configurations with an efficient scheme in an overset mesh framework. Comparison of computed flowfields to experimental and analytical results allows assessment of cavity load prediction capabilities. Prediction of the acoustic intensity levels and frequencies are of primary interest for safety reasons. However, estimation of optical distortion is required to determine mission effectiveness.

### 1.1.3 Aero-Optics Work

The study of the effect of a fluid field upon an optical field, dubbed aero-optics, has been extensive over the past four decades. Applications include imaging of re-entry vehicles or, as in this study, of astronomical bodies through the atmosphere. Many experimental and theoretical approaches to the optical distortion problem have been investigated, those of which are pertinent to this transonic aero-window problem are summarized here. The experimental efforts can be grouped into two categories: direct measurement methods and techniques based on aerodynamically inferred quantities. Results obtained via the latter method are more prevalent because of practical difficulties in direct measurement techniques [43]. In fact, only aerodynamically inferred distortion levels will used for validation in the present work.

Although early experimental and theoretical efforts assumed incoherent statistical turbulence [44, 45, 46], recent studies have begun to examine the effect of shear layer structures on electromagnetic field distortion. Using a passive scalar field from a direct numerical simulation, Truman and Lee [47] found an optimum viewing angle normal to the hairpin vortices in the homogeneous sheared fluid region. They also found analysis via non-refracting geometric optics to be equivalent to the parabolized Helmholtz representation of light. Although this class of studies provides excellent insight into the effects of small-scale structure on the electromagnetic field, it is clear that the expense of such methods precludes their near-term use for the problems under consideration here.

The study of large scale structures in shear layers has been an active topic of research since they were observed by Brown and Roshko in 1974 [48]. Only recently has the effect of these structures on the optical field been studied. In 1990, Chew and Christiansen [49, 50] experimentally observed the effect of shear layer structures on beam propagation. Tsai and Christiansen [51] used an Euler simulation to determine the optical characteristics of a perturbed free shear layer. The use of a growing sinusoidal phase plate to represent the effect of vortical structures on an optical field was hypothesized. Wissler and Roshko [52] recently performed an experimental study of the motion of a thin light beam caused by passage through a shear layer. They postulated that spanwise steering asymptotes to a higher level than the streamwise component.

The numerical modelling of the optical effect of a cavity-spanning shear layer was presented by Cassady et al. [53] in 1987. They found their two-dimensional solution to result in poor prediction of optical distortion. Farris and Clark [54, 55] used time-mean quantities and empirical evidence to ascertain the fluctuating density levels required for optical analysis.

The present effort attempts to determine what portion of the optical path distortion can be resolved using cell sizes required to obtain an accurate flowfield solution. Computed optical distortion levels are compared to flight and wind tunnel measurements for two- and three-dimensional quieted cavities, respectively. The following chapters address the methods used to predict the unsteady flows, the modelling of turbulence, and the optical distortion.

# Chapter 2

# Numerical Method

## 2.1 The Governing Equations

The Navier-Stokes equations may be expressed in integral conservation law form, coupled with the continuity and energy equations as

$$\frac{\partial}{\partial t}\left(\frac{1}{\mathcal{V}}\int_{\mathcal{V}} Q d\mathcal{V}\right) + \frac{1}{\mathcal{V}}\oint_{S} \vec{F} \cdot ds = 0 \tag{1}$$

where body forces have been neglected and the cell volumes are time invariant. Here $\mathcal{V}$ is the volume of an arbitrary fluid packet, $\vec{F} = E_{NS}\mathbf{i} + F_{NS}\mathbf{j} + G_{NS}\mathbf{k}$ is the flux tensor of second order, and $ds$ is an outward directed normal of a differential surface area. The vectors may be written in Cartesian coordinates as

$$Q = [\rho, \rho u, \rho v, \rho w, e]^T$$

$$E_{NS} = \begin{bmatrix} \rho u \\ \rho u^2 + p + \tau_{xx} \\ \rho uv + \tau_{xy} \\ \rho uw + \tau_{xz} \\ (e+p)u + \tau_{xx}u + \tau_{xy}v + \tau_{xz}w + q_x \end{bmatrix}$$

$$F_{NS} = \begin{bmatrix} \rho v \\ \rho v u + \tau_{yx} \\ \rho v^2 + p + \tau_{yy} \\ \rho v w + \tau_{yz} \\ (e+p)v + \tau_{yx}u + \tau_{yy}v + \tau_{yz}w + q_y \end{bmatrix}$$

$$G_{NS} = \begin{bmatrix} \rho w \\ \rho w u + \tau_{zx} \\ \rho w v + \tau_{zy} \\ \rho w^2 + p + \tau_{zz} \\ (e+p)w + \tau_{zx}u + \tau_{zy}v + \tau_{zz}w + q_z \end{bmatrix}$$

where each flux can be partitioned into inviscid and viscous portions. The density, pressure, and velocity components are respectively given by $\rho, p, u, v,$ and $w$. The viscous stresses are composed of the terms:

$$\begin{aligned}
\tau_{xx} &= -2\mu\frac{\partial u}{\partial x} - \lambda\left(\frac{\partial u}{\partial x} + \frac{\partial v}{\partial y} + \frac{\partial w}{\partial z}\right) \\
\tau_{yy} &= -2\mu\frac{\partial v}{\partial y} - \lambda\left(\frac{\partial u}{\partial x} + \frac{\partial v}{\partial y} + \frac{\partial w}{\partial z}\right) \\
\tau_{zz} &= -2\mu\frac{\partial w}{\partial z} - \lambda\left(\frac{\partial u}{\partial x} + \frac{\partial v}{\partial y} + \frac{\partial w}{\partial z}\right) \\
\tau_{xy} &= \tau_{yx} = -\mu\left(\frac{\partial u}{\partial y} + \frac{\partial v}{\partial x}\right) \\
\tau_{xz} &= \tau_{zx} = -\mu\left(\frac{\partial u}{\partial z} + \frac{\partial w}{\partial x}\right) \\
\tau_{yz} &= \tau_{zy} = -\mu\left(\frac{\partial v}{\partial z} + \frac{\partial w}{\partial y}\right)
\end{aligned}$$

The total energy per unit volume, $e$, is related to the internal energy per unit mass, $\epsilon$, by $e = \rho\epsilon + \rho q^2/2$. The perfect gas equation of state, $p = \rho RT$, completes the system. In addition, for thermally and calorically perfect gases, the internal energy per unit mass and the enthalpy per unit mass can be expressed solely as functions of temperature:

$$d\epsilon = c_v dT, \quad dh = c_p dT$$

Finally, for a calorically perfect gas the specific heats are constant, leaving $\epsilon = c_v T + const.$, and $h = c_p T + const.$, where the additive constants may be set to zero. The ratio of specific heats and specific gas constant are

$$\gamma = \frac{c_p}{c_v} = \frac{7}{5} \text{ for air}, \quad R = c_p - c_v$$

and the thermodynamic variables are related using

$$h_T = \frac{(e+p)}{\rho}, \quad e = \frac{p}{\gamma - 1} + \frac{\rho}{2}(u^2 + v^2 + w^2)$$

where $h_T$ is the total enthalpy per unit mass.

Fourier's law for heat transfer by conduction is assumed; hence, the heat transfer can be expressed as

$$\begin{aligned} \mathbf{q} &= -k\nabla T = -(q_x\mathbf{i} + q_y\mathbf{j} + q_z\mathbf{k}) \\ &= -\kappa\left(\frac{\partial \epsilon}{\partial x}\mathbf{i} + \frac{\partial \epsilon}{\partial y}\mathbf{j} + \frac{\partial \epsilon}{\partial z}\mathbf{k}\right) \end{aligned}$$

where $\kappa = k/c_v = \gamma\mu/Pr$. The Prandtl number for air, which is a function only of the gas, relates the diffusion of momentum to the diffusion of heat, and is fixed at $Pr = 0.72$.

The relationship between the first ($\mu$), second ($\lambda$), and bulk ($\zeta$) viscosity coefficients is $\zeta = \frac{2}{3}\mu + \lambda$. The bulk viscosity coefficient is set to zero in accordance with Stokes' hypothesis, resulting in $\lambda = -\frac{2}{3}\mu$. This hypothesis is invoked here based on the assumption that the relative effects of the shearing stress is much larger than those caused by the dilational stress effects, not on the theory for monatomic gases [56]. By using the kinetic theory of gases, the physical phenomena of thermal conductivity and viscosity can be expressed in terms of the thermodynamic states. Viscosity is related to the thermodynamic state using Sutherland's formula:

$$\mu = \frac{C_1 T^{\frac{3}{2}}}{T + C_2}$$

where $C_1$ and $C_2$ are specific to the gas in question.

## 2.2 Turbulence Model

Current limitations in computing power relegate most engineering computations to the use of grids which are too coarse to resolve all of the pertinent scales of motion. Reynolds averaging of the Navier-Stokes equations decomposes the flow into slowly and rapidly varying components [57]. The slowly varying component is resolved from the spatial and time integration step sizes, while the rapidly fluctuating component is modelled. Although the blast-wave computations did not model turbulence, the turbulence model used in the cavity flow problems is outlined here for completeness.

The effective or eddy viscosity due to additional turbulent mixing can be related to mean stresses using the Boussinesq approximation. The total effective viscosity is then given by $\mu_{total} = \mu_{molecular} + \mu_{turbulent} = \mu + \mu_t$. The Reynolds stress resulting from the Boussinesq assumption is

$$\overline{\rho u_i' u_j'} = \mu_t \left( \frac{\partial \overline{u_i}}{\partial x_j} + \frac{\partial \overline{u_j}}{\partial x_i} \right) - \frac{2}{3} \delta_{ij} \left( \mu_t \frac{\partial \overline{u_k}}{\partial x_k} \right)$$

where $\overline{(\;)}$ denotes a time mean. The eddy viscosity is given by $\mu_t \propto \rho \ell v$ where the length and velocity scales are given by $\ell$ and $v$. Alternatively, the expression for the eddy viscosity given by Prandtl is $\mu_t \propto \rho \ell^2 |\omega|$, where the magnitude of vorticity is

$$|\omega| = \sqrt{\left( \frac{\partial u}{\partial y} - \frac{\partial v}{\partial x} \right)^2 + \left( \frac{\partial v}{\partial z} - \frac{\partial w}{\partial y} \right)^2 + \left( \frac{\partial w}{\partial x} - \frac{\partial u}{\partial z} \right)^2}$$

The local density is specified by Morkovin's hypothesis, which states that compressibility does not affect the scales of the turbulent motion.

The algebraic turbulence model of Baldwin and Lomax [13], as modified and implemented by Buning [58], is described below. This description is included to clearly show how the modified model constant used in the computed cavity shear layers is determined. The description assumes flow in the $(x, y)$ plane with the freestream aligned with the $x$ coordinate.

### Treatment of Wall Bounded Flows

In Prandtl's mixing length hypothesis the turbulent eddy size is limited by the proximity to the wall, giving $\ell = ky$, where the von Kármán constant $k = 0.4$. The addition of Van Driest wall damping results in

$$\ell = ky\left(1 - e^{-y^+/A^+}\right)$$

where $A^+ = 26$, $y^+ = \frac{\sqrt{\rho_w \tau_w} y}{\mu_w}$, and the wall shear stress is $\tau_w = \left(\mu \frac{\partial u}{\partial y}\right)_w$.

The Baldwin-Lomax two-layer model uses the Prandtl-Van Driest model for the inner layer, and is given by

$$\mu_t = \begin{cases} \rho \ell^2 |\omega| & y \leq y_{crossover} \quad \text{Prandtl-Van Driest} \\ \rho C_{cp} K F_{wake} F_{Kleb} & y > y_{crossover} \quad \text{outer region} \end{cases}$$

where $y$ is the distance from the wall, $y_{crossover}$ is the location of the first intersection of inner and outer values of $\mu_t$, the Clauser constant is $K = 0.0168$, $C_{cp} = 1.6$, and

$$F_{wake} = \min \begin{cases} y_{max} F_{max} \\ C_{wk} y_{max} \frac{u_{dif}^2}{F_{max}} \end{cases}$$

where $C_{wk} = 1.0$. The quantities $F_{max}$ and its location $y_{max}$ are found from

$$F(y) = y|\omega|\left(1 - e^{-y^+/A^+}\right)$$

where the exponential term is dropped in wakes. The search for the $F_{max}$ term ends when $F(y)$ drops below a specified percent of the first peak away from the wall, or at overset mesh boundaries. The Klebanoff intermittency function is specified according to

$$F_{Kleb}(y) = \left[1 + 5.5\left(\frac{C_{Kleb} y}{y_{max}}\right)^6\right]^{-1}$$

where $C_{Kleb} = 0.3$. The total velocity difference is given by

$$u_{dif} = \sqrt{(u^2 + v^2)}_{max} - \sqrt{(u^2 + v^2)}_{min}$$

and the latter term is taken as zero at the wall.

### Treatment of Free Shear Flows

The eddy viscosity in the shear layer was computed as outlined by Buning [58]. Development of the free shear layer model begins by using $F(y) = y|\omega|$, as suggested by Baldwin and Lomax [13] for wake regions. This results in

$$\begin{aligned} F_{wake} &= C_{wk}\frac{y_{max}u_{dif}^2}{F_{max}} \\ &= C_{wk}\left(\frac{u_{dif}}{|\omega|_{max}}\right)^2 |\omega|_{max} \\ &\propto \ell^2|\omega| \end{aligned}$$

where specification of $C_{wk}$ is discussed below and the velocity difference is modified to be half the total velocity difference between the streams in the specified shear layer region

$$u_{dif} = \sqrt{(u^2+v^2)}_{max} - \sqrt{(u^2+v^2)}_{|\omega|_{max}}$$

Finally, the Klebanoff intermittency function is modified to

$$F_{Kleb}(y) = \left[1 + 5.5\left(\frac{C_{Kleb}|y - y_{|\omega|_{max}}|}{y_w}\right)^6\right]^{-1}$$

where the shear layer width is given by $y_w = u_{dif}/|\omega|_{max}$. The free shear layer model is now given by

$$\mu_t = \rho K C_{cp} C_{wk}\frac{u_{dif}^2}{|\omega|_{max}} \qquad (2)$$

after dropping the intermittency function for the analysis below.

The magnitude of the eddy viscosity in the free shear layer model can be altered by specification of $C_{wk}$. The remainder of this section shows how $C_{wk}$ is chosen based on empirical and analytic information.

Görtler's shear layer solution is given by

$$u = \frac{u_1+u_2}{2}\left[1 + \frac{u_2-u_1}{u_2+u_1}erf(\eta)\right],\ erf(\eta) = \frac{2}{\sqrt{\pi}}\int_0^x e^{-\eta^2}d\eta,\ \eta = \frac{\sigma y}{x}$$

where $u_1$ and $u_2$ are the velocities of the slow and fast streams and $\eta$ is the similarity coordinate (See Fig. 19). The spreading parameter $\sigma$ is inversely related to the spreading rate, $db/dx$, where $b$ is a measure of the shear layer width. The value of the spreading parameter when the velocity of one of the streams is zero is $\sigma_0$.

Görtler's solution can be used to determine the maximum vorticity magnitude in a free shear layer as follows:

$$\begin{aligned} |\omega| &= \left|\frac{\partial u}{\partial y}\right| = \left|\frac{\partial u}{\partial \eta}\frac{\partial \eta}{\partial y}\right| \\ &= \left|\frac{\sigma}{x\sqrt{\pi}}\Delta u e^{-\eta^2}\right|, \Delta u = (u_2 - u_1) \\ |\omega|_{max} &= \frac{\sigma}{x\sqrt{\pi}}\Delta u \end{aligned}$$

Now, using Prandtl's mixing length assumption and scaling laws for jet boundaries, eddy viscosity can also be expressed as

$$\begin{aligned} \mu_t &\propto \rho l^2 |\omega| \\ &\propto \rho l^2 \frac{\Delta u}{b} \\ &= K_0 \rho b \Delta u \end{aligned} \tag{3}$$

where $K_0 = \frac{x}{4b\sigma_0^2}$.

Setting Eqs. 2 and 3 equal results in

$$C_{wk} = (\sigma_0 K C_{cp} \sqrt{\pi})^{-1}$$

and only $\sigma_0$ remains to be specified. Estimates of $\sigma_0$ from empirical evidence is quite variable, ranging from 9.0 to 13.5 primarily dependent upon whether the upstream boundary layer is turbulent or laminar [48, 59, 60]. For this series of cavity flow efforts $\sigma_0$ was set to 11.0, which appears to be the result from the highest quality experiments, resulting in a value of $C_{wk} = 1.91$. Previous numerical investigations appear to indicate that capture of resonance is not strongly dependent upon the turbulence model in the cavity [30, 34, 36].

## 2.3 Transformation to Curvilinear Coordinates

In order to adequately resolve the solid boundary/fluid interaction, it is common to transform the governing equations into curvilinear coordinates which can be body-conformal. Specifically, the body is constrained to lie at a constant $\xi, \eta$, or $\zeta$ level.

For a stationary grid, this transformation can be expressed as

$$\tau = t, \ \xi = \xi(x,y,z), \ \eta = \eta(x,y,z), \ \zeta = \zeta(x,y,z)$$

Application of the chain rule of differentiation yields

$$\frac{\partial}{\partial x} = \xi_x \frac{\partial}{\partial \xi} + \eta_x \frac{\partial}{\partial \eta} + \zeta_x \frac{\partial}{\partial \zeta}$$

with similar expressions for the partials with respect to $y$ and $z$. The inverse transformation gives

$$\frac{\partial}{\partial \xi} = x_\xi \frac{\partial}{\partial x} + y_\xi \frac{\partial}{\partial y} + z_\xi \frac{\partial}{\partial z}$$

Again, expressions can be found for the $\eta$ and $\zeta$ partials in a like manner. Represented in matrix form:

$$\begin{bmatrix} \frac{\partial}{\partial x} \\ \frac{\partial}{\partial y} \\ \frac{\partial}{\partial z} \end{bmatrix} = \underbrace{\begin{bmatrix} \xi_x & \eta_x & \zeta_x \\ \xi_y & \eta_y & \zeta_y \\ \xi_z & \eta_z & \zeta_z \end{bmatrix}}_{T} \begin{bmatrix} \frac{\partial}{\partial \xi} \\ \frac{\partial}{\partial \eta} \\ \frac{\partial}{\partial \zeta} \end{bmatrix}$$

and for the inverse transformation,

$$\begin{bmatrix} \frac{\partial}{\partial \xi} \\ \frac{\partial}{\partial \eta} \\ \frac{\partial}{\partial \zeta} \end{bmatrix} = \underbrace{\begin{bmatrix} x_\xi & y_\xi & z_\xi \\ x_\eta & y_\eta & z_\eta \\ x_\zeta & y_\zeta & z_\zeta \end{bmatrix}}_{T^{-1}} \begin{bmatrix} \frac{\partial}{\partial x} \\ \frac{\partial}{\partial y} \\ \frac{\partial}{\partial z} \end{bmatrix}$$

Combining the use of $T = (T^{-1})^{-1}$ and finite volume metrics, such as those described by Vinokur [61], leads to a scheme which is freestream-preserving because of the telescoping property. Hence, if the surface normals to a constant $\xi, \eta$, or $\zeta$ plane are defined respectively as

$$\begin{aligned} \mathbf{s}_{i+\frac{1}{2}} &= s_{x,i+\frac{1}{2}}\mathbf{i} + s_{y,i+\frac{1}{2}}\mathbf{j} + s_{z,i+\frac{1}{2}}\mathbf{k} \\ &= \frac{1}{2}(\mathbf{r}_7 - \mathbf{r}_4) \times (\mathbf{r}_8 - \mathbf{r}_3) \end{aligned}$$

$$
\begin{aligned}
\mathbf{s}_{j+\frac{1}{2}} &= s_{x,j+\frac{1}{2}}\mathbf{i} + s_{y,j+\frac{1}{2}}\mathbf{j} + s_{z,j+\frac{1}{2}}\mathbf{k} \\
&= \frac{1}{2}(\mathbf{r}_7 - \mathbf{r}_2) \times (\mathbf{r}_3 - \mathbf{r}_6) \\
\mathbf{s}_{k+\frac{1}{2}} &= s_{x,k+\frac{1}{2}}\mathbf{i} + s_{y,k+\frac{1}{2}}\mathbf{j} + s_{z,k+\frac{1}{2}}\mathbf{k} \\
&= \frac{1}{2}(\mathbf{r}_6 - \mathbf{r}_8) \times (\mathbf{r}_5 - \mathbf{r}_7)
\end{aligned}
$$

where the index convention is shown in Fig. 3.

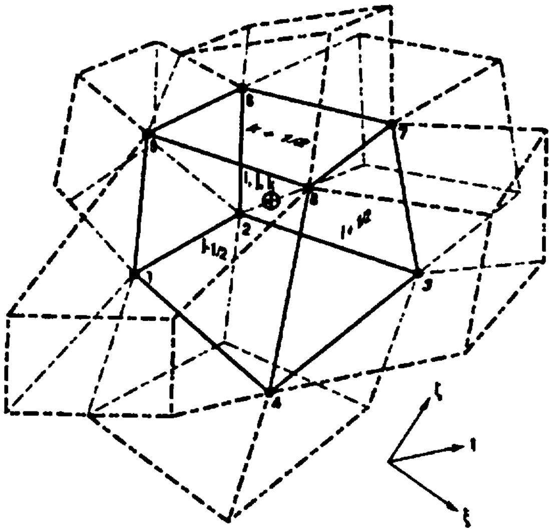

Figure 3: Hexahedral cell and stencil

The metrics can then be formed as

$$
\begin{aligned}
\xi_x &= J(y_\eta z_\zeta - y_\zeta z_\eta) &= \frac{1}{\mathcal{V}} s_{x,i+\frac{1}{2}} \\
\xi_y &= J(x_\zeta z_\eta - x_\eta z_\zeta) &= \frac{1}{\mathcal{V}} s_{y,i+\frac{1}{2}} \\
\xi_z &= J(x_\eta y_\zeta - x_\zeta y_\eta) &= \frac{1}{\mathcal{V}} s_{z,i+\frac{1}{2}} \\
\eta_x &= J(y_\zeta z_\xi - y_\xi z_\zeta) &= \frac{1}{\mathcal{V}} s_{x,j+\frac{1}{2}} \\
\eta_y &= J(x_\xi z_\zeta - x_\zeta z_\xi) &= \frac{1}{\mathcal{V}} s_{y,j+\frac{1}{2}} \\
\eta_z &= J(x_\zeta y_\xi - x_\xi y_\zeta) &= \frac{1}{\mathcal{V}} s_{z,j+\frac{1}{2}} \\
\zeta_x &= J(y_\xi z_\eta - y_\eta z_\xi) &= \frac{1}{\mathcal{V}} s_{x,k+\frac{1}{2}}
\end{aligned}
$$

$$\begin{aligned}
\zeta_y &= J(x_\eta z_\xi - x_\xi z_\eta) = \frac{1}{\mathcal{V}} s_{y,k+\frac{1}{2}} \\
\zeta_z &= J(x_\xi y_\eta - x_\eta y_\xi) = \frac{1}{\mathcal{V}} s_{z,k+\frac{1}{2}}
\end{aligned}$$

These metrics represent the projections of the cell face normal into $(x, y, z)$ space. The faces of the hexahedron exactly enclose the discrete control volume, i.e., no gaps are permitted at the edges.

Finally, the Jacobian of the coordinate transformation is equivalent to the inverse of the volume, as related by

$$\begin{aligned}
\frac{1}{J} &= \frac{\partial(x,y,z)}{\partial(\xi,\eta,\zeta)} \\
&= x_\xi(y_\eta z_\zeta - y_\zeta z_\eta) - x_\eta(y_\xi z_\zeta - y_\zeta z_\xi) + x_\zeta(y_\xi z_\eta - y_\eta z_\xi) \\
&= \mathcal{V} = \frac{1}{3}(\mathbf{s}_{i-\frac{1}{2}} + \mathbf{s}_{j-\frac{1}{2}} + \mathbf{s}_{k-\frac{1}{2}}) \cdot (\mathbf{r}_7 - \mathbf{r}_1)
\end{aligned}$$

Utilizing these metrics in the application of the chain rule to Eq. (1) and subsequent simplification yields

$$Q'_\tau + E'_\xi + F'_\eta + G'_\zeta = 0$$

where

$$\begin{aligned}
Q' &= Q\mathcal{V} \\
E'_{NS} &= (E_{NS}\xi_x + F_{NS}\xi_y + G_{NS}\xi_z)\mathcal{V} \\
&= [E_{NS}s_x + F_{NS}s_y + G_{NS}s_z]_i \\
F'_{NS} &= (E_{NS}\eta_x + F_{NS}\eta_y + G_{NS}\eta_z)\mathcal{V} \\
&= [E_{NS}s_x + F_{NS}s_y + G_{NS}s_z]_j \\
G'_{NS} &= (E_{NS}\zeta_x + F_{NS}\zeta_y + G_{NS}\zeta_z)\mathcal{V} \\
&= [E_{NS}s_x + F_{NS}s_y + G_{NS}s_z]_k
\end{aligned}$$

Separating the inviscid and viscous portions of the flux vectors, then in the $\xi$ direction

$E'_{NS} = E' + E'_v$, where

$$E' = \mathcal{V}\begin{bmatrix} \rho U \\ \rho u U + \xi_x p \\ \rho v U + \xi_y p \\ \rho w U + \xi_z p \\ (e+p)U \end{bmatrix}$$

Here the contravariant velocity component in $\xi$ is $U = u\xi_x + v\xi_y + w\xi_z$, without metric normalization. The viscous flux can be represented as

$$E'_v = \mathcal{V}\begin{bmatrix} 0 \\ \tau_{xx}\xi_x + \tau_{yx}\xi_y + \tau_{zx}\xi_z \\ \tau_{xy}\xi_x + \tau_{yy}\xi_y + \tau_{zy}\xi_z \\ \tau_{xz}\xi_x + \tau_{yz}\xi_y + \tau_{zz}\xi_z \\ (ue'_2 + ve'_3 + we'_4) + (q_x\xi_x + q_y\xi_y + q_z\xi_z) \end{bmatrix}$$

where the viscous stress terms are evaluated by again invoking the chain rule, and the flux in the $\eta$ and $\zeta$ directions are found similarly. The results presented herein are implemented using either the thin-layer or the full viscous term treatment.

The widespread use of the thin-layer approximation, first implemented by Steger [62], can be justified from either physical or algorithmic arguments. Physically, the neglect of all diffusion processes parallel to the body is similar to that used in boundary-layer theory, albeit not as restrictive. Hence, when the viscous effects are confined to thin regions along a constant $\xi, \eta,$ or $\zeta$ plane, this assumption is valid. Regarding the algorithmic argument, the banded matrix structure used in multidimensional algorithms which sequentially solve a set of unidirectional problems can include only these thin-layer terms implicitly. This thin-layer flux in the $\eta$ direction, assumed to be the body normal coordinate, is expressed as:

$$F'_{tl} = -\mathcal{V}\begin{bmatrix} 0 \\ m_1 u_\eta + m_4 v_\eta + m_5 w_\eta \\ m_4 u_\eta + m_2 v_\eta + m_6 w_\eta \\ m_5 u_\eta + m_6 v_\eta + m_3 w_\eta \\ m_1 \bar{u} u_\eta + m_2 \bar{v} v_\eta + m_3 \bar{w} w_\eta + m_4(\bar{u} v_\eta + \bar{v} u_\eta) + m_5(\bar{u} w_\eta + \bar{w} u_\eta) \\ + m_6(\bar{v} w_\eta + \bar{w} v_\eta) + \kappa\epsilon_\eta(\eta_x^2 + \eta_y^2 + \eta_z^2) \end{bmatrix}$$

where the $(\bar{\ })$ denotes an arithmetic mean value and

$$\begin{aligned} m_1 &= \mu\left(\frac{4}{3}\eta_x^2+\eta_y^2+\eta_z^2\right), \; m_4 = \frac{\mu}{3}\eta_x\eta_y \\ m_2 &= \mu\left(\eta_x^2+\frac{4}{3}\eta_y^2+\eta_z^2\right), \; m_5 = \frac{\mu}{3}\eta_x\eta_z \\ m_3 &= \mu\left(\eta_x^2+\eta_y^2+\frac{4}{3}\eta_z^2\right), \; m_6 = \frac{\mu}{3}\eta_y\eta_z \end{aligned}$$

These viscous flux terms may be found for the remaining spatial coordinates as well. The results presented here are implemented using either the thin-layer or the full viscous term treatment, as required by the the flow physics.

### Nondimensionalization

The governing equations may be nondimensionalized by the choice of a length scale, denoted by $\tilde{L}$, and reference values of $\rho$, $u$, and $p$ such as

$$\tilde{\rho}_{ref} = \tilde{\rho}_\infty, \quad \tilde{u}_{ref} = \sqrt{\tilde{p}_\infty/\tilde{\rho}_\infty}, \quad \tilde{p}_{ref} = \tilde{p}_\infty$$

The nondimensionalized variables follow:

$$\begin{aligned} &\rho = \tilde{\rho}/\tilde{\rho}_{ref}, \quad p = \tilde{p}/\tilde{p}_{ref}, \quad e = \tilde{e}/(\tilde{\rho}_{ref}\tilde{u}_{ref}^2) \\ &u = \tilde{u}/\tilde{u}_{ref}, \quad v = \tilde{v}/\tilde{u}_{ref}, \quad w = \tilde{w}/\tilde{u}_{ref} \\ &t = \tilde{t}\tilde{u}_{ref}/\tilde{L}, \quad T = p/\rho, \quad \mu = \tilde{\mu}/\tilde{\mu}_{ref} \end{aligned}$$

The Reynolds number resulting from this procedure is $Re = \tilde{\rho}_{ref}\tilde{L}\tilde{u}_{ref}/\tilde{\mu}_{ref}$, where the $(\tilde{\ })$ denotes a dimensional quantity, and $(\ )_\infty$ denotes the freestream conditions.

## 2.4 Upwind Schemes

The numerical scheme will be described using first-order terms, following which the higher-order extensions will be outlined. The scheme expressed for a cell which has a mean flux value on each of the six sides is

$$\frac{\partial}{\partial\tau}\int_{\mathcal{V}} Q d\mathcal{V} + \int_{j-\frac{1}{2}}^{j+\frac{1}{2}}\int_{k-\frac{1}{2}}^{k+\frac{1}{2}}(E'_{i+\frac{1}{2},j,k} - E'_{i-\frac{1}{2},j,k})d\zeta d\eta$$

$$\begin{aligned}
&+ \int_{k-\frac{1}{2}}^{k+\frac{1}{2}} \int_{i-\frac{1}{2}}^{i+\frac{1}{2}} (F'_{i,j+\frac{1}{2},k} - F'_{i,j-\frac{1}{2},k}) d\xi d\zeta \\
&+ \int_{i-\frac{1}{2}}^{i+\frac{1}{2}} \int_{j-\frac{1}{2}}^{j+\frac{1}{2}} (G'_{i,j,k+\frac{1}{2}} - G'_{i,j,k-\frac{1}{2}}) d\eta d\xi = 0
\end{aligned}$$

In fully discrete form, after dropping the primes for convenience, the governing equations can be written as

$$\begin{aligned}
Q^{n+1}_{i,j,k} - Q^{n}_{i,j,k} &+ \frac{\Delta\tau}{\mathcal{V}_{i,j,k}} \Big\{ (E^{n+1}_{i+\frac{1}{2},j,k} - E^{n+1}_{i-\frac{1}{2},j,k}) \\
&+ \qquad (F^{n+1}_{i,j+\frac{1}{2},k} - F^{n+1}_{i,j-\frac{1}{2},k}) \\
&+ \qquad (G^{n+1}_{i,j,k+\frac{1}{2}} - G^{n+1}_{i,j,k-\frac{1}{2}}) \Big\} = 0
\end{aligned}$$

where $n$ denotes the time level in this implicit representation, and $\Delta\xi$, $\Delta\eta$, and $\Delta\zeta$ are set to unity for convenience.

These flux terms may be evaluated using a technique which may be broadly classed as either central or upwind. The latter technique is chosen for this study for the desirable numerical properties, such as diagonal dominance of the flux Jacobian, and for the physical dependence on zones of influence which are inherent in upwind schemes.

Upwind schemes bias the derivative evaluations required to determine the flux across fluid cells according to the sign of the characteristic speeds. In this manner these methods bring the physics of the hyperbolic system, the unsteady Euler equations, into the numerical solution process. To facilitate the implementation of these upwind schemes, the eigensystem is determined. The similarity transformation which diagonalizes the unsteady, inviscid, gas-dynamic equations, shown by Warming, et al. [63], is outlined as follows

$$\frac{\partial E}{\partial Q} = T \Lambda T^{-1}$$

where the rows of $T^{-1}$ are the eigenvectors and

$$\Lambda = \Lambda^{+} + \Lambda^{-} = \ diag \left[ \hat{U}, \hat{U}, \hat{U}, \hat{U} + c, \hat{U} - c \right] ||\mathrm{s}||$$

using normalized contravariant velocity components. The eigenvalues can be split according to, among other splittings, their signs:

$$\lambda^{\pm} \ = \ \frac{\lambda \pm |\lambda|}{2}$$

where $\lambda$ is an element of $\Lambda$.

Two upwind schemes are implemented here to compare the results which may be obtained with either of the techniques. The initial portion of this discussion will be presented unidimensionally for simplicity; the multidimensional extension will be outlined towards the end of this section.

### 2.4.1 Flux Vector Splitting

The shock-capturing scheme developed by Steger and Warming [64] revisited the classical characteristic procedures. They found that the Euler equations possessed the property of homogeneity of degree one for the equation of state used here, meaning $E(\alpha Q) = \alpha E(Q)$. For a vector with this property $E = AQ$, where A is the flux Jacobian given by $\partial E/\partial Q$. Consequently, the flux vector can be split into two parts, each physically corresponding to the right and left moving waves. This technique resulted in the flux being represented as a combination of the subspaces associated with the positive and negative eigenvalues, expressed as

$$\begin{aligned} E &= T(\Lambda^+ + \Lambda^-)T^{-1}Q = (A^+ + A^-)Q \\ &= E^+ + E^- \end{aligned}$$

where $T$ and $T^{-1}$ are the right and left eigenvectors of the flux Jacobian matrix $A$, respectively. The flux across a cell face can be determined by

$$\begin{aligned} E_{i+\frac{1}{2}} &= E^+_{i+\frac{1}{2}} + E^-_{i+\frac{1}{2}} \\ &= A^+_{i+\frac{1}{2}}Q_i + A^-_{i+\frac{1}{2}}Q_{i+1} \end{aligned}$$

Because the Jacobian at $i + \frac{1}{2}$ is dependent on two states, this solution method now diverges from the original Steger-Warming flux vector splitting. The treatment of this Jacobian is shown in a following section. Linearization in time can be performed in one dimension as follows, extension to the multidimensions is straightforward and is omitted for brevity. At the $n + 1$ time level,

$$\begin{aligned} E^{n+1}_{i+\frac{1}{2}} &= (A^+)^{n+1}_{i+\frac{1}{2}}Q^{n+1}_i + (A^-)^{n+1}_{i+\frac{1}{2}}Q^{n+1}_{i+1} \\ &= (A^+)^n_{i+\frac{1}{2}}\delta Q^n_i + (A^-)^n_{i+\frac{1}{2}}\delta Q^n_{i+1} + E^n_{i+\frac{1}{2}} \end{aligned}$$

where the implicit change in the dependent variables is given by $\delta Q^n = Q^{n+1} - Q^n$. Note that the Jacobian matrices are frozen at time level $n$. The remaining flux, $E^{n+1}_{i-\frac{1}{2}}$, may be obtained similarly.

To assess the effect on stability of this type of linearization, a procedure developed by Barth [65] is applied to this method. Using the semidiscrete form $\partial Q_i / \partial t = -R_i$, then

$$R_i = \frac{1}{\Delta x}\left(E_{i+\frac{1}{2}} - E_{i-\frac{1}{2}}\right)$$

Using frozen Jacobian matrices, the method can be linearized as follows:

$$\left[\frac{I}{\Delta t} + \left(\frac{\partial R}{\partial Q}\right)^n\right]\delta Q = -R^n \tag{4}$$

where for the first-order subset the Jacobian is a block tridiagonal matrix. The blocks along the $i^{th}$ row are

$$\begin{aligned}
\frac{\partial R_i}{\partial Q_{i-1}} &= \frac{1}{\Delta x}\left(-A^{+}_{i-\frac{1}{2}}\right)\\
\frac{\partial R_i}{\partial Q_i} &= \frac{1}{\Delta x}\left(A^{+}_{i+\frac{1}{2}} - A^{-}_{i-\frac{1}{2}}\right)\\
\frac{\partial R_i}{\partial Q_{i+1}} &= \frac{1}{\Delta x}\left(A^{-}_{i+\frac{1}{2}}\right)
\end{aligned}$$

This scheme is inherently conservative in space because of the telescoping property of the finite-volume formulation; analysis of this scheme reveals that it is also conservative in time, possibly allowing the use of large Courant numbers [65]. A demonstration of this analysis proceeds by writing the scheme as

$$\left[\frac{I}{\Delta t} + A^n\right]\delta Q = -R^n = -A^n Q^n$$

hence

$$Q^{n+1} + \Delta t A^n Q^{n+1} = Q^n \tag{5}$$

In order for the scheme to be conservative in time over a periodic domain, the global average of a solution must remain constant for all time, i.e., $\sum_{i=1}^{I} Q_i^0 = \sum_{i=1}^{I} Q_i^n = \sum_{i=1}^{I} Q_i^{n+1}$. Hence, when Eq. (5) is summed across the domain, the result is that the columns of $A^n$ must sum to zero. For example, summation across a three-point domain yields

$$[Q_1+Q_2+Q_3]^{n+1}+\Delta t\,[I,\ I,\ I]\begin{bmatrix} B_1^n & C_1^n & . \\ A_2^n & B_2^n & C_2^n \\ . & A_3^n & B_3^n \end{bmatrix}^n \begin{bmatrix} Q_1 \\ Q_2 \\ Q_3 \end{bmatrix}^{n+1} = [Q_1+Q_2+Q_3]^n$$

where the elements of the middle column of $A^n$ are $C_1^n = A^-_{3/2}$, $B_2^n = A^+_{5/2} - A^-_{3/2}$, $A_3^n = -A^+_{5/2}$, which sum to zero.

### 2.4.2 Flux Difference Splitting

Flux difference splitting methods are based on the Riemann problem, solved exactly by Godunov in 1959 [66]. The Riemann problem is composed of $m+1$ piecewise constant states separated by $m$ wave families. The waves include shocks, contact surfaces, and rarefaction fans. For each of the Riemann problem cells, the transition of the dependent variables is a function of a parameter family. The solution can be found once these transition states are known. Approximate Riemann solvers simplify the numerics of the problem by eliminating the iterative process required to find the intermediate states.

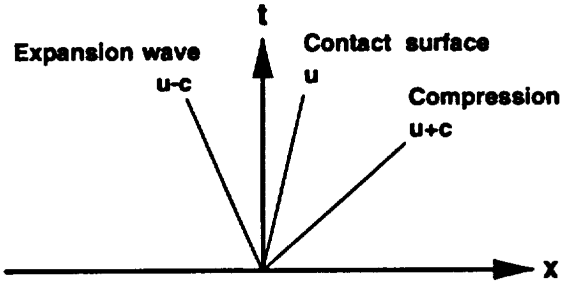

Figure 4: Riemann problem schematic

Figure 4 shows a schematic of the Riemann problem with the piecewise constant states separated by the appropriate wave families. The flux through the cell face is

$$\begin{aligned} E_{i+\frac{1}{2}} &= \frac{1}{2\Delta x}\left[E_i + E_{i+1} - (\Delta E^+_{i+\frac{1}{2}} - \Delta E^-_{i+\frac{1}{2}})\right] \\ &= \frac{1}{2\Delta x}(E_i + E_{i+1} - \Delta|E|_{i+\frac{1}{2}}) \end{aligned}$$

where $|E| = |A|Q = (A^+ - A^-)Q = [T(\Lambda^+ - \Lambda^-)T^{-1}]Q$. The flux differences associated with the + and − traveling waves are

$$\begin{aligned}\Delta E^+_{i+\frac{1}{2}} &= (T\Lambda^+T^{-1})_{i+\frac{1}{2}}(Q_{i+1} - Q_i)\\ \Delta E^-_{i+\frac{1}{2}} &= (T\Lambda^-T^{-1})_{i+\frac{1}{2}}(Q_{i+1} - Q_i)\end{aligned}$$

Again utilizing the semidiscrete form $\partial Q_i/\partial t = -R_i$, then

$$R_i = \frac{1}{2\Delta x}\left[(E_{i+1} - E_{i-1}) - (\Delta|E|_{i+\frac{1}{2}} + \Delta|E|_{i-\frac{1}{2}})\right]$$

This method can be linearized using a procedure similar to that described previously in Eq. (4). The blocks of the $i^{th}$ row are expressed as

$$\begin{aligned}\frac{\partial R_i}{\partial Q_{i-1}} &= \frac{1}{2\Delta x}\left(-A_{i-1} + \frac{\partial\Delta|E|_{i-\frac{1}{2}}}{\partial Q_{i-1}}\right)\\ \frac{\partial R_i}{\partial Q_i} &= \frac{1}{2\Delta x}\left(-\frac{\partial\Delta|E|_{i+\frac{1}{2}}}{\partial Q_i} + \frac{\partial\Delta|E|_{i-\frac{1}{2}}}{\partial Q_i}\right)\\ \frac{\partial R_i}{\partial Q_{i+1}} &= \frac{1}{2\Delta x}\left(A_{i+1} - \frac{\partial\Delta|E|_{i+\frac{1}{2}}}{\partial Q_{i+1}}\right)\end{aligned}$$

Substitution of the flux difference splitting expression yields

$$\begin{aligned}\frac{\partial\Delta|E|_{i+\frac{1}{2}}}{\partial Q_{i+1}} &= \frac{\partial}{\partial Q_{i+1}}\left[|A|_{i+\frac{1}{2}}(Q_{i+1} - Q_i)\right]\\ &= |A|_{i+\frac{1}{2}} + \frac{\partial\Delta|A|_{i+\frac{1}{2}}}{\partial Q_{i+1}}(Q_{i+1} - Q_i)\end{aligned}$$

These true Jacobians are expensive to compute, and the simplification to approximate Jacobians is made as

$$\frac{\partial\Delta|E|_{i+\frac{1}{2}}}{\partial Q_{i+1}} \approx |A|_{i+\frac{1}{2}}$$

Utilizing these approximate Jacobians, the linearization proceeds as

$$\begin{aligned}E^{n+1}_{i+\frac{1}{2}} &= \frac{1}{2\Delta x}(E^{n+1}_i + E^{n+1}_{i+1} - \Delta|E|^{n+1}_{i+\frac{1}{2}})\\ &= \frac{1}{2\Delta x}\left[(A^n_i + |A|^n_{i+\frac{1}{2}})\delta Q_i + (A^n_{i+1} - |A|^n_{i+\frac{1}{2}})\delta Q_{i+1}\right] + E^n_{i+\frac{1}{2}}\end{aligned}$$

where $E^{n+1} = E^n + A^n\delta Q$ and $Q^{n+1} = Q^n + (\partial Q/\partial t)^n\Delta t$. The fluxes through the remaining faces are determined similarly. This scheme can also be shown to obey the criterion for conservation in time.

### 2.4.3 Roe Averaging

In order to determine the Jacobian at the cell face $i + \frac{1}{2}$, some function, $A = A(Q_L, Q_R)$, must be assumed, where the subscripts indicate left and right states. The location of this flux evaluation is one of the differences between finite-difference and finite-volume schemes. The evaluation used here is attributable to Roe [67], which provides an approximate solution to the Riemann problem. This Jacobian is created through the use of a parameter vector composed of a geometric-like mean of the states. The more obvious arithmetic Jacobian forms, such as $A = \frac{1}{2}(A_L + A_R)$ or $A = A(\frac{1}{2}(Q_L + Q_R))$, are not conservative forms. Conservative Jacobian forms satisfy $A(Q_L, Q_R)(Q_L - Q_R) = E_L - E_R$. Stated explicitly, the Roe averaging operation is

$$
\begin{aligned}
\bar{\rho} &= \sqrt{\rho_L \rho_R} \\
\bar{u}_i &= \frac{u_{iL}\sqrt{\rho_L} + u_{iR}\sqrt{\rho_R}}{\sqrt{\rho_L} + \sqrt{\rho_R}} \\
&= \frac{\rho_L u_{iL} + \bar{\rho}(u_{iL} + u_{iR}) + \rho_R u_{iR}}{\rho_L + 2\bar{\rho} + \rho_R} \\
\bar{h}_T &= \frac{\rho_L (h_T)_L + \bar{\rho}((h_T)_L + (h_T)_R) + \rho_R (h_T)_R}{\rho_L + 2\bar{\rho} + \rho_R}
\end{aligned}
$$

where a $(\bar{\ })$ denotes a Roe averaged quantity, and the latter forms are presented as inexpensive alternative expressions. Substitution of $(i)$ for $L$ and $(i + 1)$ for $R$ allows the evaluation of the Jacobian at the intermediary cell face. For the flux vector splitting case described earlier, MacCormack [57] has found this average helps to alleviate excessive numerical dissipation in regions dominated by viscous effects. Roe averaged values are utilized throughout the development presented here.

### 2.4.4 Higher-Order Extensions

Spatially first-order methods frequently provide inadequate resolution of the flowfield. However, the methods discussed above can be extended to higher-order spatial accuracy by modification of the right hand side. In order to assist in the preservation of well-behaved solutions near the discontinuities admitted by the strong conservation law form of the Euler equations, a total variation diminishing technique is implemented. If the total variation of a solution is defined as $TV(u) = \sum_{i=-\infty}^{\infty} |u_{i+1} - u_i|$, then a solution which follows $TV(u^{n+1}) \leq TV(u^n)$ is TVD. The TVD constraint can be shown to result in diagonal dominance, allowing the use of relaxation schemes. In this manner the scheme may be extended to higher space accuracy throughout the smoothly varying regions of the field, reducing the accuracy in localities of high-gradient and extrema in order to obtain sharp and oscillation-free resolution. These methods are rigorously applicable only to scalar nonlinear equations or a system of linear equations in one spatial dimension. Application of these schemes to multi-dimensional systems of nonlinear equations are generally not TVD. Moreover, it is not clear that the higher-order accuracy of the unidimensional problem is retained in multidimensional cases. However, the results which can be obtained demonstrate the usefulness of the technique.

Of the several methods which fall into the TVD domain [9], the technique implemented here is one attributable to Chakravarthy and Osher [68], the development of which follows for completeness. In this formulation, the higher-order flux can be expressed as a sum of a first-order flux, denoted $E_{i+\frac{1}{2}}$, and a flux correction term. The flux correction terms are determined by first computing the flux differences across the $m$ wave families mentioned previously. Subsequent limiting of these flux differences and summation across the wave families results in the higher-order flux. This flux is expressed as

$$\begin{aligned}\hat{E}_{j+\frac{1}{2}} = E_{i+\frac{1}{2}} \; & - \; \frac{(1-\phi)}{4}\left[\sum_{i}^{m} \widetilde{dE}^{j-}_{i+\frac{3}{2}}\right] - \frac{(1+\phi)}{4}\left[\sum_{i}^{m} \widetilde{\widetilde{dE}}^{j-}_{i+\frac{1}{2}}\right] \\ & + \; \frac{(1+\phi)}{4}\left[\sum_{i}^{m} \widetilde{dE}^{j+}_{i+\frac{1}{2}}\right] + \frac{(1-\phi)}{4}\left[\sum_{i}^{m} \widetilde{\widetilde{dE}}^{j+}_{i-\frac{1}{2}}\right]\end{aligned}$$

where $(\tilde{\ })$ and $(\tilde{\tilde{\ }})$ indicate a quantity that has been limited, $j$ is the index denoting the wave family, and $i$ is the index assigned to a cell center. Using the notation of $l^j$ for the rows of the left eigenvector matrix, $T^{-1}$, and $r^j$ for the columns of the right eigenvector matrix, $T$, then the measure of the change in the dependent variables is

$$\alpha^j_{i+\frac{1}{2}} = l^j_{i+\frac{1}{2}} \cdot (Q_{i+1} - Q_i)$$

The measure of the change in the flux is defined as

$$\sigma^j = \lambda^j \alpha^j = (\lambda^{j+} + \lambda^{j-})\alpha^j$$

the eigenvalues being split as shown previously. The limited counterparts of these values are obtained as:

$$\begin{aligned}
\tilde{\sigma}^{-}_{i+\frac{3}{2}} &= \text{minmod}\left[\sigma^{-}_{i+\frac{3}{2}}, \beta\sigma^{-}_{i+\frac{1}{2}}\right] \\
\tilde{\tilde{\sigma}}^{-}_{i+\frac{1}{2}} &= \text{minmod}\left[\sigma^{-}_{i+\frac{1}{2}}, \beta\sigma^{-}_{i+\frac{3}{2}}\right] \\
\tilde{\sigma}^{+}_{i+\frac{1}{2}} &= \text{minmod}\left[\sigma^{+}_{i+\frac{1}{2}}, \beta\sigma^{+}_{i-\frac{1}{2}}\right] \\
\tilde{\tilde{\sigma}}^{+}_{i-\frac{1}{2}} &= \text{minmod}\left[\sigma^{+}_{i-\frac{1}{2}}, \beta\sigma^{+}_{i+\frac{1}{2}}\right]
\end{aligned}$$

This limiter returns the argument of smaller magnitude when the signs are equal, and returns zero when the arguments are of opposite sign. This procedure effectively adds dissipation locally in regions of high flux gradient and at inflection points. In this manner, monotonicity is preserved by preventing the creation of new extrema while preserving the global accuracy of the solution. While formal accuracy estimates are difficult to ascertain because of the nonlinear application of limiting to different wave families, numerical experiments have demonstrated that the global accuracy of the underlying scheme is preserved [69].

The compression parameter, $\beta$, is restricted according to $1 < \beta \leq \frac{3-\phi}{1-\phi}$ and the limiting operator is given as

$$\text{minmod}(x, y) = \text{sign}(x)\left(\max\left\{0, \min\left[|x|, y\,\text{sign}(x)\right]\right\}\right)$$

The compression parameter reduces the amount of dissipation added, the range being bounded by accuracy and TVD constraints. Finally, the limited flux difference values are expressed as

$$\begin{aligned}
\widetilde{dE}^{j-}_{i+\frac{3}{2}} &= \tilde{\sigma}^{j-}_{i+\frac{3}{2}} r_{i+\frac{3}{2}} \\
\widetilde{\widetilde{dE}}^{j-}_{i+\frac{1}{2}} &= \tilde{\tilde{\sigma}}^{j-}_{i+\frac{1}{2}} r_{i+\frac{1}{2}} \\
\widetilde{dE}^{j+}_{i+\frac{1}{2}} &= \tilde{\sigma}^{j+}_{i+\frac{1}{2}} r_{i+\frac{1}{2}} \\
\widetilde{\widetilde{dE}}^{j+}_{i-\frac{1}{2}} &= \tilde{\tilde{\sigma}}^{j+}_{i-\frac{1}{2}} r_{i-\frac{1}{2}}
\end{aligned}$$

This asymmetric limiter is designed to modify the fluxes only in the rapidly varying portions of the flow, where nonphysical oscillations are likely to occur. Since these high-gradient regions are confined to thin regions, the dominant solution domain is differenced in accordance with the underlying scheme. Variances in the value of the compression parameter allow the fluxes to be limited for different gradient levels. This implies that use of $\beta_{max}$ will cause the limiting action to be taken only in the high-gradient regions, and lower values of $\beta$ will result in limiting for commensurately lower flux gradients. The variety of schemes which can be obtained using this technique are shown in Table 1.

| $\phi$ | Unlimited Scheme | $\beta_{max}$ | $2^{nd}$ order TE |
|---|---|---|---|
| $-1$ | Fully upwind | 2 | $\frac{1}{3}(\Delta x)^2 f_{xxx}$ |
| $-\frac{1}{3}$ | Nameless | $\frac{5}{2}$ | $\frac{1}{6}(\Delta x)^2 f_{xxx}$ |
| 0 | Fromm's | 3 | $\frac{1}{12}(\Delta x)^2 f_{xxx}$ |
| $\frac{1}{3}$ | $3^{rd}$ Order | 4 | 0 |
| $\frac{1}{2}$ | Low TE $2^{nd}$ Order | 5 | $-\frac{1}{24}(\Delta x)^2 f_{xxx}$ |
| 1 | Central | $\infty$ | $-\frac{1}{6}(\Delta x)^2 f_{xxx}$ |

Table 1: Summary of schemes

Here $TE = (\frac{1}{3} - \phi)(\Delta x)^2 f_{xxx}/4$ defines the leading term of the truncation error for the unlimited form of the schemes. Local metrics have been used in the above method to maintain reasonable computational efficiency, a satisfactory approximation for grids which do not contain rapid variations.

### 2.4.5 Viscous Terms

The viscous terms are treated through central differencing about the cell faces. The explicit terms are conventionally differenced after chain-rule expansion, inclusive of the cross terms if these diffusion processes are significant for the problem at hand. The left hand side does not include these cross terms, and the resultant viscous Jacobian, employing $V = [\rho, u, v, w, \epsilon]^T$ as the primitive variable vector, is

$$M = \left.\frac{\partial V}{\partial \eta}\right|_{TL} = -\begin{bmatrix} 0 & 0 & 0 & 0 & 0 \\ 0 & m_{22} & \mu s_x s_y/3 & \mu s_x s_z/3 & 0 \\ 0 & m_{23} & m_{33} & \mu s_y s_z/3 & 0 \\ 0 & m_{24} & m_{34} & m_{44} & 0 \\ 0 & m_{52} & m_{53} & m_{54} & m_{55} \end{bmatrix}$$

$$m_{22} = \mu(\frac{4}{3}s_x^2 + s_y^2 + s_z^2) \ , \ m_{33} = \mu(s_x^2 + \frac{4}{3}s_y^2 + s_z^2)$$
$$m_{44} = \mu(s_x^2 + s_y^2 + \frac{4}{3}s_z^2) \ , \ m_{55} = \kappa(s_x^2 + s_y^2 + s_z^2)$$

$$\begin{aligned} m_{52} &= um_{22} + vm_{23} + wm_{24} \\ m_{53} &= um_{32} + vm_{33} + wm_{34} \\ m_{54} &= um_{42} + vm_{43} + wm_{44} \end{aligned}$$

The viscous flux through a cell wall at $j + \frac{1}{2}$ is of the form $M_{j+\frac{1}{2}}(N_{j+1}Q_{j+1} - N_jQ_j)$ where

$$N = \frac{\partial Q}{\partial V} = \frac{1}{\rho}\begin{bmatrix} \rho & 0 & 0 & 0 & 0 \\ -u & 1 & 0 & 0 & 0 \\ -v & 0 & 1 & 0 & 0 \\ -w & 0 & 0 & 1 & 0 \\ -\epsilon + \frac{1}{2}(u^2 + v^2 + w^2) & -u & -v & -w & 1 \end{bmatrix}$$

Now, using three-dimensional indices $(i, j, k)$, expansion of the block structure gives

$$\begin{aligned} - & \left\{\frac{\Delta t}{\mathcal{V}} A^+_{i-\frac{1}{2},j,k}\right\}\delta Q_{i-1,j,k} \\ - & \left\{\frac{\Delta t}{\mathcal{V}}\left[B^+_{i,j-\frac{1}{2},k} - \frac{1}{\mathcal{V}}M_{i,j-\frac{1}{2},k}N_{i,j-1,k}\right]\right\}\delta Q_{i,j-1,k} \\ - & \left\{\frac{\Delta t}{\mathcal{V}} C^+_{i,j,k-\frac{1}{2}}\right\}\delta Q_{i,j,k-1} \\ + & \left\{I + \frac{\Delta t}{\mathcal{V}}\left[A^+_{i+\frac{1}{2},j,k} - A^-_{i-\frac{1}{2},j,k}\right.\right. \end{aligned}$$

$$\begin{aligned}
&\qquad + B^{+}_{i,j+\frac{1}{2},k} - B^{-}_{i,j-\frac{1}{2},k} \\
&\qquad + C^{+}_{i,j,k+\frac{1}{2}} - C^{-}_{i,j,k-\frac{1}{2}} \\
&\qquad \left. \left. + \frac{1}{\mathcal{V}} (M_{i,j+\frac{1}{2},k} + M_{i,j-\frac{1}{2},k}) N_{i,j,k} \right] \right\} \delta Q_{i,j,k} \\
+ &\left\{ \frac{\Delta t}{\mathcal{V}} C^{-}_{i,j,k+\frac{1}{2}} \right\} \delta Q_{i,j,k+1} \\
+ &\left\{ \frac{\Delta t}{\mathcal{V}} \left[ B^{-}_{i,j+\frac{1}{2},k} - \frac{1}{\mathcal{V}} M_{i,j+\frac{1}{2},k} N_{i,j+1,k} \right] \right\} \delta Q_{i,j+1,k} \\
+ &\left\{ \frac{\Delta t}{\mathcal{V}} A^{-}_{i+\frac{1}{2},j,k} \right\} \delta Q_{i+1,j,k} = \Delta Q_{i,j,k}
\end{aligned}$$

where only the thin-layer terms in $\eta$ are shown here.

### 2.4.6 Factorization

The extension of the techniques given above is accomplished through dimensional splitting. The method used here is that of Yanenko [70], where the factors are chosen in the $\xi, \eta$, and $\zeta$ directions. Expressing the three-dimensional equations in compact notation as

$$(I + \frac{\Delta\tau}{\Delta\xi} A + \frac{\Delta\tau}{\Delta\eta} B + \frac{\Delta\tau}{\Delta\zeta} C) \delta Q = \Delta Q$$

then the factorization procedure yields

$$(I + \frac{\Delta\tau}{\Delta\xi} A)(I + \frac{\Delta\tau}{\Delta\eta} B)(I + \frac{\Delta\tau}{\Delta\zeta} C) \delta Q = \Delta Q$$

This system can be solved sequentially through the use of intermediary steps without loss of time accuracy. Although alternating direction implicit schemes of this type offer advantages of vectorization, the system is solved as a sequence of unidimensional problems, hence limiting the size of the time step due to stability restrictions [71]. The use of this technique here is justified by the requirement of adequate time history flow resolution, thus imposing an additional constraint on the maximum time step. Application of a line Gauss-Seidel method to the starting shock tunnel test case, discussed in Section 5.1.2, confirmed this hypothesis. This relaxation method offered a slightly increased stability range, but not enough to offset the additional expense caused by short vector lengths for the shock tunnel problem. Additionally, since for the factored scheme the flux exchange occurs at the same time level, the technique is conservative, even when convergence at the subiteration level is not attained for each time step.

The expense of both the upwind algorithms is relatively high: 86$\mu$s per cell per iteration using a single processor on the Ames Research Center CCF Cray Y-MP/832. These vectorized codes have computation rates of approximately 140 MFLOPS. In addition, the memory requirement is 40 words per cell. Decreased processor times may be achieved by many methods. For example, freezing the flux Jacobians for several subiterations will offer a processing time reduction of 15% per subiteration, albeit at the expense of memory. It is clear that the expense of these upwind methods is warranted only for problem classes in which the improved resolution is critical.

### 2.4.7 Newton Iterative Technique

Reduction of the linearization and factorization errors is achieved by a Newton iterative method of the type described by Rai and Chakravarthy [74] and Rogers and Kwak [75], albeit with the addition of allowance for a varying step size [14]. Assuming that the initial guess lies within the radius of convergence, the right hand side is converged to an arbitrary accuracy while holding time fixed. Since the right hand side includes the higher-order difference representations of the Navier-Stokes equations, linearization and factorization errors are eliminated at convergence. The method is discussed below where $m$ is the Newton iteration index and $n$ is the conventional index denoting time level. Discretizing $Q_t + E_x = 0$ gives

$$\begin{aligned}\frac{1}{\Delta\tau}(Q^{n+1,m+1} - Q^{n+1,m}) &= \frac{1}{\Delta\tau}\left[Q^{n+1,m+1} - Q^{n,m+1} - (Q^{n+1,m} - Q^{n})\right]\\ &\approx Q_t^{n+1,m+1} - \frac{1}{\Delta\tau}(Q^{n+1,m} - Q^{n})\end{aligned}$$

where the solution is converged at time level $n$, hence $Q^{n,m+1} = Q^n$. Defining $\delta Q' = Q^{n+1,m+1} - Q^{n+1,m}$, then

$$\begin{aligned}I\delta Q' &= \Delta\tau Q_t^{n+1,m+1} - (Q^{n+1,m} - Q^{n})\\ &= -\Delta\tau E_x^{n+1,m+1} - (Q^{n+1,m} - Q^{n})\end{aligned}$$

Linearization at iteration level $m+1$ gives

$$E_x^{n+1,m+1} = E_x^{n+1,m} + \left(\frac{\partial E_x}{\partial Q}\right)^{n+1,m} \delta Q'$$

where the flux Jacobian has been frozen at iteration $m$. Substitution yields

$$I\delta Q' = -\Delta\tau E_x^{n+1,m} - \Delta\tau \frac{\partial}{\partial x} A^{n+1,m}\delta Q' - (Q^{n+1,m} - Q^n)$$

Rearranging results in

$$\left[I + \frac{\Delta\tau}{\Delta x}A^{n+1,m}\right]\delta Q' = -(Q^{n+1,m} - Q^n + \Delta\tau E_x^{n+1,m})$$

which reverts to the standard noniterative form $\left[\frac{I}{\Delta\tau} + \frac{1}{\Delta x}A^n\right]\delta Q' = -E_x^n$, when no subiterations are taken, as can be seen by substitution of $n$ for $n+1, m$.

The temporally second-order accurate representation is found by extension of the above procedure. Using a three-point backward time stencil derived from a standard Taylor series approach,

$$Q_t = C_0 Q^{n+1} + C_1 Q^n + C_2 Q^{n-1}$$

where

$$\begin{aligned} C_0 &= \frac{1-\sigma}{(1-\sigma)\Delta\tau_2 + \Delta\tau_1}, \quad C_1 = \frac{\sigma}{(1-\sigma)\Delta\tau_2 + \Delta\tau_1} \\ C_2 &= \frac{-1}{(1-\sigma)\Delta\tau_2 + \Delta\tau_1} \end{aligned}$$

and $\sigma = (1 + \Delta\tau_1/\Delta\tau_2)^2$. The elapsed time between the $n-1$ and $n$ time levels is given by $\Delta\tau_1$ and between $n$ and $n+1$ is $\Delta\tau_2$. Rewriting at iteration level $m+1$,

$$C_0(Q^{n+1,m+1} - Q^{n+1,m}) = Q_t^{n+1,m+1} - (C_0 Q^{n+1,m} + C_1 Q^n + C_2 Q^{n-1})$$

Finally,

$$\left[I + \frac{1}{C_0 \Delta x}A^{n+1,m}\right]\delta Q' = -(Q^{n+1,m} + \frac{C_1}{C_0}Q^n + \frac{C_2}{C_0}Q^{n-1}) - \frac{1}{C_0}E_x^{n+1,m}$$

which reduces to $\left[\frac{3I}{2\Delta\tau} + \frac{1}{\Delta x}A^n\right]\delta Q' = \frac{1}{2\Delta t}(Q^n - Q^{n-1}) - E_x^n$ for the case of no iterations with fixed time step size. The formulation given above allows the use of a time step size which is a function of time, but is fixed at each step for the entire domain. The use of a variable time step size allows the solution to progress using a constant Courant number, possibly preventing inadvertent divergences. Higher-order accuracy in time may be obtained by extension of the above technique, albeit with additional memory requirements.

The assertion that this technique reduces the factorization and linearization errors is substantiated as follows. The right hand side of the method contains the discretized governing equations in their pure form, that is, without the numerical approximations utilized to attain rapid convergence. The left hand side allows the use of large time steps by relieving the Courant-Friedrichs-Lewy stability constraint. Deferring the question of uniqueness, if a set of dependent variables is found such that the right hand side is satisfied, then this field is a solution to the discretized equations regardless of the approximations made to arrive at that set.

## 2.5 Diagonal Scheme

Resolution of the transient wave-field of the blast-wave/target interaction problem class benefits from the use of upwind methods. In contrast, for the SOFIA effort a combination of the low transonic regime, the complex geometry, and the large problem size required an efficient integration scheme. The algorithms used for the SOFIA effort, coded by Buning and Chan [58], are implemented within the Chimera overset grid framework [72]. The solutions were obtained using a diagonal scheme [73], using spatially varying time steps for steady state computations, and fixed step size for unsteady flow simulations. The code utilizes the conventional dependent variable vector, $Q = [\rho, \rho u, \rho v, \rho w, e]^T$, and pseudo-finite-volume metrics. Euler implicit time marching and second-order central spatial differencing were used for the computations presented here. Computations were performed on the Numerical Aerodynamic Simulator (NAS) Cray Y-MP/832 using SSD, at an expense of $14\mu s$ per point per iteration.

## 2.6 Geometry Treatment

Geometric modelling and grid generation is a significant portion of the effort spent in obtaining the flowfield about any reasonably complex geometry. A structured approach is utilized for this study, with the body-conformal internal grids generated using the elliptic techniques of Thompson, et al. [76], Thomas and Middlecoff [77], and Steger and Sorenson [78]. The external flow domain was discretized via algebraic and hyperbolic means, the topology was chosen to allow the use of these grid generation methods. The grids used in this investigation were generated using codes written by Steinbrenner, Chawner, and Fouts [79], Chan and Steger [80], and Atwood and Vogel [81]. A discussion of the treatment of the surface, the grid topology, and the grid strategy is given below.

### Surface Modelling

The geometry used for the SOFIA configurations utilized clipped wings to emulate the geometry used in a specially designed experiment [16]. The use of clipped wings in the wind tunnel test allowed a cavity of more realistic size to be studied. The fuselage, wing, fairing, nacelles, and telescope geometry were obtained from CAD databases. Positioning errors in the database were corrected using blueprints.

The process of generating the more complicated grids, e.g., the quiet SOFIA configuration with telescope (configuration 100), warrants additional comment. Extensive wind tunnel testing [16] resulted in a hand-formed ramp and aperture, shown in Fig. 5a. This geometry was subsequently laser digitized [82], resulting in a data set of the form shown in Fig. 5b. These data, accurate to approximately 0.2 mm (0.6% of cavity length), were then converted into a form suitable for the surface grid using a standard CAD package [83].

Surface definition via bicubic surfaces in regions of high curvature can cause local oscillatory behavior [79, 81]. Along overlapping surfaces this property is manifested as $C^0$, or jump discontinuities at zone boundaries. The problem is ameliorated through bilinear projection from one zone boundary to another [84]. The distance of projection is typically five orders of magnitude less than a characteristic geometry length.

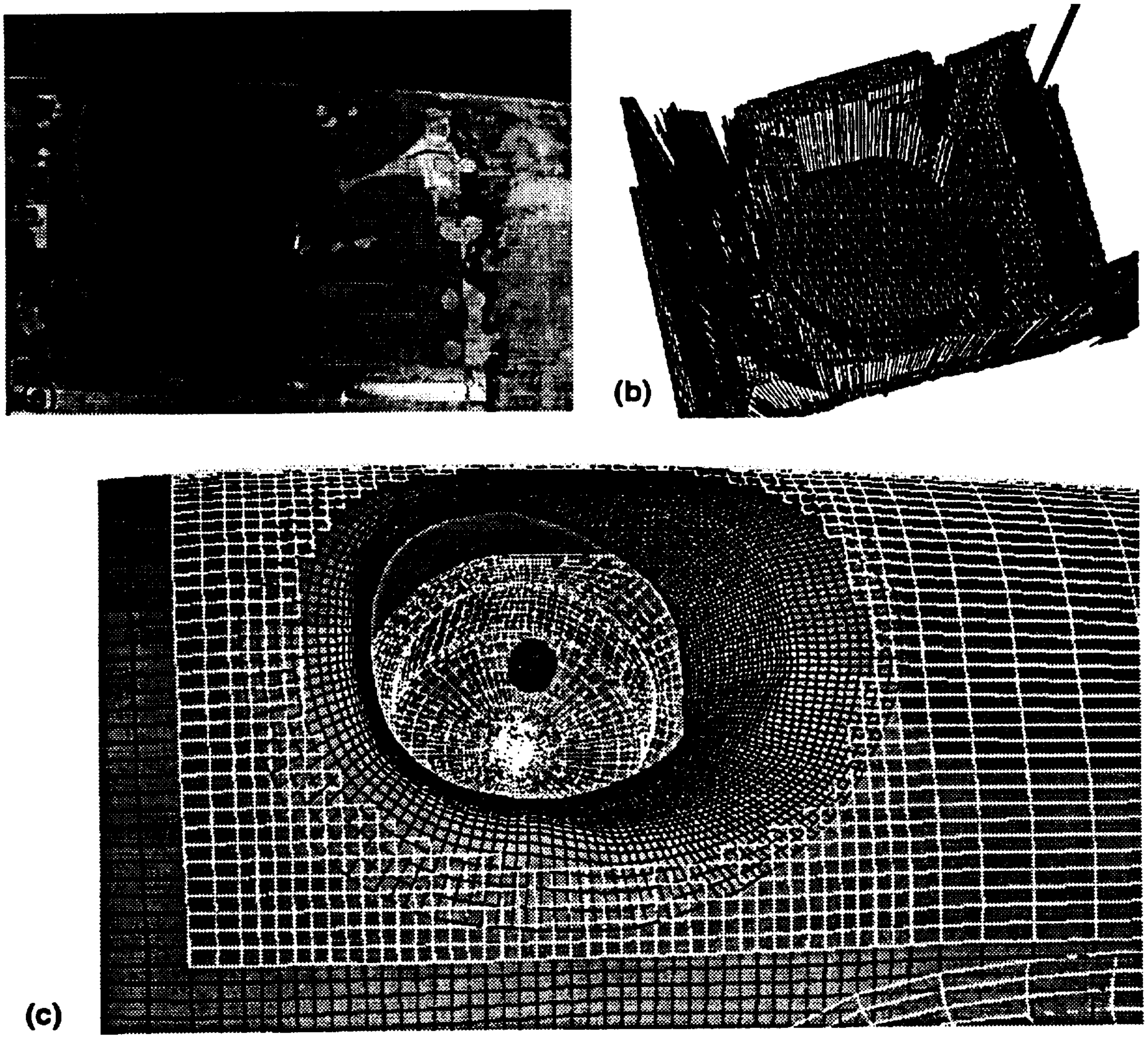

Figure 5: Geometry acquisition: (a) model, (b) laser digitized configuration, and (c) grids

### Topology

The overset grid topology scheme was chosen for its geometric flexibility and its ability to allow refinement of individual zones. The use of a different grid for each component of the geometry simplifies changes that will occur as the design matures. In fact, the geometries with cavities were built upon the clean configuration grids, providing a savings of many man-hours. The topology was chosen to allow rapid evaluation of new configurations and permit simple specification of turbulent wall and shear layer regions.

### Grids

The SOFIA configuration $y^+$ values for the first grid point away from the wall were generally about 4.0, the farfield boundary was placed at 20 fuselage diameters, and the outflow 10 diameters downstream. Damping of acoustic waves at the farfield boundary was achieved by the use of large cells which were unable to support the high frequency waves.

The clean SOFIA 747 configuration, without a cavity, was modelled using four grids for the half-body: one each for the fuselage, wing, wing tip, and nacelle. The grid point count was approximately $4 \times 10^5$. The fuselage grid was refined in anticipation of the cavity to provide similarly sized cells in interpolation regions.

The untreated aperture geometry, configuration 25 of the wind-tunnel test, was gridded by reflecting the four grid zones described above and adding two for the cavity. The term untreated refers to the lack of geometry modifications which can eliminate cavity resonance. The fuselage zonal boundaries were shifted meridionally to move interpolation away from the cavity region. The two additional grid zones consisted of an outer cavity grid surrounding the cavity region and an inner cavity grid which included the cavity walls and the shear layer region. The outer zone was utilized to isolate the cavity unsteadiness from the global solution. The total grid point count for this case was about $1.2 \times 10^6$ distributed in 10 zones.

The treated aperture geometry, configuration 100 of the wind-tunnel test, was modelled by the addition of seven grid zones to the clean case: one each for isolation, aperture wall, shear layer, cavity wall, telescope tub, secondary mirror, and an inner ramp grid. The total grid point count for this case was about $1.8 \times 10^6$ in 15 zones.

# Chapter 3

# Boundary Conditions

The flow solver block implicit boundary conditions are implemented in a manner consistent with the flux split linearization described earlier. The inviscid and viscous impermeable wall conditions are prescribed similarly to those given by MacCormack [85]. Although the following procedures are presented for a cell face which lies along a constant $\eta$ plane, the procedure may be generalized for application to any cell boundary. Finally, the characteristic inflow and outflow boundaries are discussed.

The inviscid, impermeable wall boundary condition is described for a pair of cells between which the surface lies, depicted in Fig. 6. In the following discussion, the cell

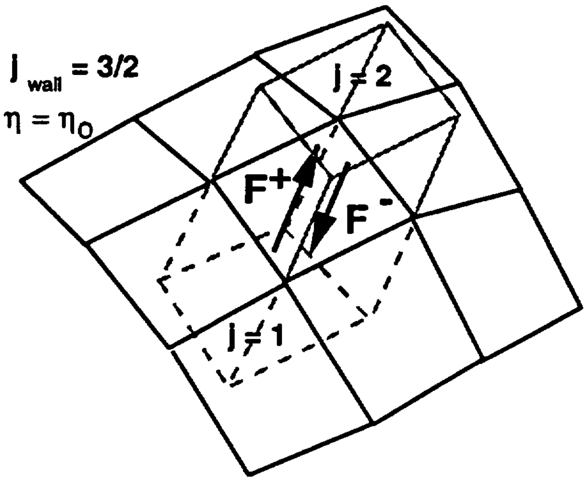

Figure 6: Flux computation at a cell face or wall

above the wall will be denoted by subscript 2, the cell below the wall by subscript 1. At the centroid of cell 2 the velocity is expressed as

$$\vec{V}_2 = u_2\mathbf{i} + v_2\mathbf{j} + w_2\mathbf{k}$$

and at the cell wall the surface normal is

$$\begin{aligned} \hat{s}_{wall} &= \frac{1}{\|\mathbf{s}\|}(s_x\mathbf{i} + s_y\mathbf{j} + s_z\mathbf{k})|_{wall} \\ &= (\hat{s}_x\mathbf{i} + \hat{s}_y\mathbf{j} + \hat{s}_z\mathbf{k})|_{wall} \end{aligned}$$

where $\|\mathbf{s}\|$ is the vector magnitude. Hence, the velocity component normal to the wall is

$$\begin{aligned} \vec{V}_{n2} &= \|\vec{V}_{n2}\|\hat{s}_{wall} \\ &= (u\hat{s}_x + v\hat{s}_y + w\hat{s}_z)(\hat{s}_x\mathbf{i} + \hat{s}_y\mathbf{j} + \hat{s}_z\mathbf{k})_{wall} \end{aligned}$$

Since, $\vec{V} = \vec{V}_t + \vec{V}_n$, then the tangential velocity component is

$$\begin{aligned} \vec{V}_{t2} &= \vec{V}_2 - \vec{V}_{n2} \\ &= \quad [u - \hat{s}_x(u\hat{s}_x + v\hat{s}_y + w\hat{s}_z)]\mathbf{i} \\ &\quad +[v - \hat{s}_y(u\hat{s}_x + v\hat{s}_y + w\hat{s}_z)]\mathbf{j} \\ &\quad +[w - \hat{s}_z(u\hat{s}_x + v\hat{s}_y + w\hat{s}_z)]\mathbf{k}|_2 \end{aligned}$$

The flow tangency condition is satisfied by $\vec{V}_{t1} = \vec{V}_{t2}$ and $\vec{V}_{n1} = -\vec{V}_{n2}$. Total energy and density are found from reflection as even functions through the relation $R\delta Q_1 = ER\delta Q_2$, where $E = diag[1, 1, -1, 1, 1]$ and the rotation matrix is found from an eigenvalue problem, the eigenvectors being the rows of

$$R = \begin{bmatrix} 1 & 0 & 0 & 0 & 0 \\ 0 & -(\hat{s}_y + \hat{s}_z) & \hat{s}_x & \hat{s}_x & 0 \\ 0 & \hat{s}_x & \hat{s}_y & \hat{s}_z & 0 \\ 0 & \hat{s}_z & \hat{s}_z & -(\hat{s}_x + \hat{s}_y) & 0 \\ 0 & 0 & 0 & 0 & 1 \end{bmatrix}_{j=\frac{3}{2}}$$

A Riemann problem can then be solved at the wall to determine the flux from $F_{j=\frac{3}{2}} = B^{-}Q_2 + B^{+}Q_1$. This amounts to the wall being represented as a contact discontinuity by constraining the contravariant velocity to vanish. Implicitly, this results in

$$\delta Q_1 = R^{-1}ER|_{wall}\delta Q_2 \tag{6}$$

where

$$R^{-1}ER = \begin{bmatrix} 1 & 0 & 0 & 0 & 0 \\ 0 & 1-2\hat{s}_x^2 & -2\hat{s}_x\hat{s}_y & -2\hat{s}_x\hat{s}_z & 0 \\ 0 & -2\hat{s}_y\hat{s}_x & 1-2\hat{s}_y^2 & -2\hat{s}_y\hat{s}_z & 0 \\ 0 & -2\hat{s}_z\hat{s}_x & -2\hat{s}_z\hat{s}_y & 1-2\hat{s}_z^2 & 0 \\ 0 & 0 & 0 & 0 & 1 \end{bmatrix}_{j=\frac{3}{2}}$$

The block tridiagonal system may be written as

$$\begin{bmatrix} B_1' & C_1' & \\ A_2' & B_2' & C_2' \\ & & \ddots \end{bmatrix} \begin{bmatrix} \delta Q_1 \\ \delta Q_2 \\ \vdots \end{bmatrix} = \begin{bmatrix} \Delta Q_1 \\ \Delta Q_2 \\ \vdots \end{bmatrix}$$

Now the change in flux across an arbitrary cell wall boundary is given by $\Delta E_{wall} = A^{+}\delta Q_1 + A^{-}\delta Q_2$, or the sum of the changes in the flux contribution from the positive and negative moving waves. Substitution of Eq. (6) yields

$$\Delta E_{wall} = (A^{+}R^{-1}ER + A^{-})\delta Q_2$$

and it can be seen that dependence upon $\delta Q_1$ has been eliminated. Hence, the block tridiagonal system may be represented with embedded boundary conditions as

$$\begin{bmatrix} B'' & C_2' & \\ A_3' & B_3' & C_3' \\ & & \ddots \end{bmatrix} \begin{bmatrix} \delta Q_2 \\ \delta Q_3 \\ \vdots \end{bmatrix} = \begin{bmatrix} \Delta Q_2 \\ \Delta Q_3 \\ \vdots \end{bmatrix}$$

where $B''$ is the appropriately modified Jacobian.

The viscous impermeable wall imposes additional constraints on the specification of the wall flux. Again utilizing a primitive variable vector $V = [\rho, u, v, w, \epsilon]^T$, then

$$\delta V_1 = diag[1, t_u, t_v, t_w, t]\delta V_2 = \frac{\partial V_1}{\partial V_2}\delta V_2$$

for a wall face at $\frac{3}{2}$. In this form the toggles $t_u, t_v, t_w$, and $t$ are set at 1 or $-1$ for a slip or a no-slip condition, or adiabatic or isothermal wall, respectively. This may be seen by simply rearranging expressions of the form $u_{wall} = \frac{1}{2}(u_1 + u_2)$ or $u_{wall} = u_1 = u_2$. Having already specified the impermeable wall conditions earlier, only the viscous terms at the wall are of present concern. Looking at the terms of the form

$$\Delta Q_2 = \frac{\Delta t}{\mathcal{V}^2}(-MN_1\delta Q_1 + MN_2\delta Q_2 + \cdots)$$

then substitution of the wall relations above leaves a term

$$\begin{aligned} \Delta Q_2 &= \frac{\Delta t}{\mathcal{V}^2}\left[-M\frac{\partial V_1}{\partial V_2}\frac{\partial V_2}{\partial Q_2}\delta Q_2 + M\frac{\partial V_2}{\partial Q_2}\delta Q_2 + \cdots\right] \\ &= \frac{\Delta t}{\mathcal{V}^2}\left[M\left(I - \frac{\partial V_1}{\partial V_2}\right)\frac{\partial V_2}{\partial Q_2}\delta Q_2 + \cdots\right] \end{aligned}$$

which is subsequently embedded into the block structure. The dependent variables within cell 1 are specified according to boundary-layer theory, holding the pressure gradient zero normal to the wall. The remaining variables follow from fluid and thermodynamic relations.

The inflow and outflow boundaries are specified according to characteristic theory for generality. Linearization of $T^{-1}Q_t + \Lambda T^{-1}Q_\xi = 0$ for the forward differenced inflow condition yields

$$[I - \frac{\Delta t}{\mathcal{V}}\tilde{\Lambda}]\tilde{T}^{-1}\delta Q_i = -\frac{\Delta t}{\mathcal{V}}\tilde{\Lambda}\tilde{T}^{-1}(Q_{i+1}^n - Q_i^n)$$

where the modified eigensystem matrices are computed as

$$\tilde{\Lambda} = \ diag\left[0, 0, 0, 0, (1 - t_{in})(\hat{U} - c)\right] \|\mathbf{s}\|$$

$$\tilde{T}^{-1} = \begin{bmatrix} \partial p_T/\partial Q \\ \partial T_T/\partial Q \\ \partial v/\partial Q \\ \partial w/\partial Q \\ (1 - t_{in})l_5 + t_{in}\partial u/\partial Q \end{bmatrix}$$

Here $t_{in}$ is zero or unity for subsonic or supersonic inflow. The specified variables are chosen such that a unique set of flow quantities are given at the entrance.

The outflow condition is specified in a like manner; however, there are now at least four characteristics linking the domain with the boundary. Backward differencing about $i+1$ and specification of static pressure at the exit results in the modified matrices

$$\tilde{\Lambda} = diag\left[\hat{U},\hat{U},\hat{U},\hat{U}+c,t_{out}(\hat{U}-c)\right]\|\mathrm{s}\|$$

$$\tilde{T}^{-1} = \begin{bmatrix} l_1 \\ l_2 \\ l_3 \\ l_4 \\ (1-t_{out})\partial p/\partial Q + t_{out} l_5 \end{bmatrix}$$

In the above development, the eigensystem is evaluated at the boundary face in question, maintaining consistency with the interior treatment.

The strongly unsteady blast-wave problems investigated here revealed that the use of block implicit boundary conditions resulted in significantly enhanced convergence. This beneficial effect is caused by the faster signal propagation arising from the incorporation of the boundary conditions within the linear system. However, for the cavity flows explicit boundary condition implementations were used for coding simplicity. Comparison of the computed results with experiment show satisfactory resolution of the moderate unsteadiness present in transonic cavity flows.

Several of the cavity cases used characteristic boundary conditions holding mass flow, total enthalpy, and flow angle constant. Subsonic inflow conditions, for example, are related to the interior of the flow by the $u-c$ characteristic:

$$\frac{\partial p}{\partial t} - \rho c\frac{\partial u}{\partial t} = -(u-c)\left(\frac{\partial p}{\partial x} - \rho c\frac{\partial u}{\partial x}\right)$$

which may be rewritten as

$$p_t - \rho c u_t + c(\rho u_t + u\rho_t) \quad = \quad -(u-c)[p_x - \rho c u_x] + c(\rho u)_t$$

where the mass flow is fixed for these computations, giving $(\rho u)_t = 0$. Discretization and rearrangement yields

$$d\rho \quad = \quad \frac{-(u-c)\frac{\Delta t}{\Delta x}}{\frac{\partial p}{\partial \rho} + cu}[p_2 - p_1 - \rho c(u_2 - u_1)]$$

$$\begin{aligned}
\rho_1^{n+1} &= \rho_1^n + d\rho \\
u_1^{n+1} &= \frac{\dot{m}}{\rho_1^{n+1}} \\
T_1^{n+1} &= T_T - \frac{\gamma - 1}{2}\left(\frac{u_1^2}{\gamma R}\right)
\end{aligned}$$

Implementation of the boundary conditions, unless otherwise noted, are as follows: viscous impermeable wall conditions are no-slip, zero normal pressure gradient, and adiabatic; information transfer across overset mesh boundaries is implemented using non-conservative trilinear interpolation of $Q$. Treatment of the farfield boundaries is case dependent and is noted in the results section.

# Chapter 4

# Geometrical Aero-Optics

The objective of the numerical simulation of the flow about the SOFIA airborne observatory is to design a safe configuration which will have the least detrimental effects upon the optics. Towards this goal, the following transonic cavity flow problems were divided into three sections. First, the unsteady interaction of the external flow with the cavity requires time-dependent solutions to the Reynolds-averaged Navier-Stokes equations. Second, the shear layer growth rate is strongly dependent on turbulence effects which must be modelled due to the grid coarseness. The final portion of the problem is the application of the optical model to the unsteady density field in the shear layer to determine seeing quality.

The variation of the speed of light through gases is primarily a function of the density field. This fact has been extensively used to benefit the study of fluid physics, as exemplified by use of schlieren, shadowgraph, and interferometry techniques. However, the objective of the present effort is to quantify the wavefront distortion of a beam of light propagating through the shear layer. This distortion is computed using the history of the density variations within the shear layer to predict fluctuations in the optical path length via geometric optics. This will in turn allow prediction of the telescope resolution limits due to seeing and thus contribute to the telescope design specifications.

The geometric optics model developed here assumes that the impact of the fluid density on the optical field may be computed by casting light rays through a field

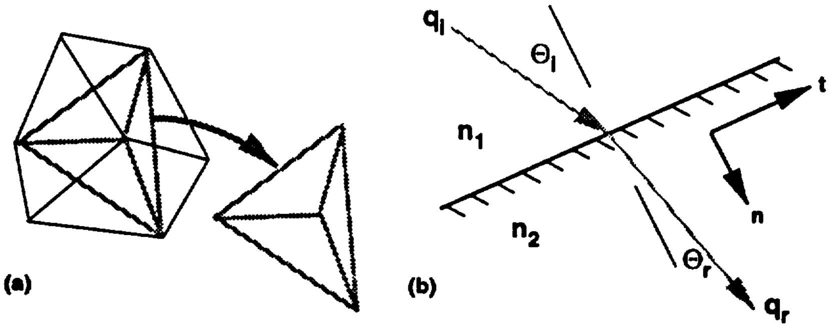

Figure 7: Geometric optics: (a) partitioning of hexahedrons into tetrahedrons, and (b) intersection and refraction procedure

discretized into tetrahedrons. Diffraction effects, which become important when the wavelength approaches the scale size, are neglected. The simplifications afforded by the use of planar facets and piecewise continuous media are utilized by tesselating, or partitioning, each hexahedron of the flowfield into five tetrahedra as shown in Fig. 7. It should be noted that other tesselations were found to be more robust for thin warped cells [86], however for the shear layer grids used here the five tetrahedra decomposition is well-behaved.

Application of the geometric optics code to two preliminary test cases was undertaken to determine sensitivity of the optics code to the above non-unique tesselation. The parallel emergence of the rays after propagation through a plate and a prism of index of refraction $n = 2.4$ suggests that the results are relatively insensitive to the method of tesselation.

The problem can now be divided into three steps: 1) propagation of the ray, 2) intersection of the ray with a facet, and 3) refraction. Solution for the point contained in both the facet, $\mathbf{p}$, and the ray, $\mathbf{q}_i$, expressed parametrically as

$$\mathbf{q}_i(t) = \mathbf{d} + \mathbf{e}t \ ; \ \mathbf{p}(u, w) = \mathbf{a} + \mathbf{b}u + \mathbf{c}w$$

results in the intersection in parametric coordinates, which is found from the dot product of the normal with the ray and the surface:

$$(\mathbf{b} \times \mathbf{c}) \cdot \mathbf{p} = (\mathbf{b} \times \mathbf{c}) \cdot \mathbf{q}_i$$

$$t = \frac{(\mathbf{b} \times \mathbf{c}) \cdot \mathbf{a} - (\mathbf{b} \times \mathbf{c}) \cdot \mathbf{d}}{(\mathbf{b} \times \mathbf{c}) \cdot \mathbf{e}}$$

$$u = \frac{(\mathbf{c} \times \mathbf{e}) \cdot \mathbf{d} - (\mathbf{c} \times \mathbf{e}) \cdot \mathbf{a}}{(\mathbf{c} \times \mathbf{e}) \cdot \mathbf{b}}$$

$$w = \frac{(\mathbf{b} \times \mathbf{e}) \cdot \mathbf{d} - (\mathbf{b} \times \mathbf{e}) \cdot \mathbf{a}}{(\mathbf{b} \times \mathbf{e}) \cdot \mathbf{c}}$$

where the vector coefficients are found from boundary conditions:

$$\begin{aligned} \mathbf{a} &= \mathbf{p}(0,0) \\ \mathbf{b} &= \mathbf{p}(1,0) - \mathbf{p}(0,0) \\ \mathbf{c} &= \mathbf{p}(0,1) - \mathbf{p}(0,0) \\ \mathbf{d} &= \mathbf{q}_i(0) \\ \mathbf{e} &= \mathbf{q}_i(1) - \mathbf{q}_i(0) \end{aligned}$$

Specification of the light ray origin and a direction initializes the problem. Following the search for the initial hexahedral cell in which the ray originates, the tetrahedron within this hexahedron must be computed. First, the shortest intersection distance of the ray with the 16 planes which compose the hexahedron is computed. Then the dot product of the ray with the fourth vertex of the closest plane determines the origin tetrahedron. Subsequent intersection and refraction processes are a marching procedure. The optical path length ($OPL$) is found from

$$OPL = \int n(s) ds \approx \sum_j n_j \Delta s_j$$

where $n(s)$ is the index of refraction as a function of position along the ray, $s$. The variation of the $OPL$ over the aperture gives a measure of the wavefront error caused by the shear layer.

The refraction process is determined according to Snell's law as shown in Fig. 7, where the planar interface, $\mathbf{p}(u, w)$, separating the media and the incident light ray, $\mathbf{q}_i(t)$ [87, 81] are depicted. Generalization to three-dimensions is accomplished by rotation to the osculating plane, which includes the surface normal and both the incident and refracted rays. In this osculating plane, a rotated local coordinate system is defined:

$$\mathbf{q}_i = |\mathbf{q}_{i_n}|\hat{\mathbf{n}} + |\mathbf{q}_{i_t}|\hat{\mathbf{t}}$$

where

$$|\mathbf{q}_{i_n}| = |\mathbf{q}_i|\cos\theta_i \quad \text{and} \quad |\mathbf{q}_{i_t}| = |\mathbf{q}_i|\sin\theta_i$$

$$\hat{\mathbf{t}} = \frac{\hat{\mathbf{q}}_i - \hat{\mathbf{n}}\cos\theta_i}{\sin\theta_i}$$

Application of Snell's law $n_1 \sin\theta_i = n_2 \sin\theta_r$ where $n = 1 + \beta\frac{\rho}{\rho_{STP}}$ results in an expression for the refracted ray:

$$\hat{\mathbf{q}}_r = \hat{\mathbf{n}}\cos\theta_r + \hat{\mathbf{t}}\sin\theta_r$$

The local index of refraction, $n_j$, is found by arithmetically averaging the densities at the four vertices of the tetrahedron, where only one vertex changes as the ray propagates to a neighbor tetrahedron. The Gladstone-Dale constant, $\beta$, is a function of the media and of the wavelength. Using air as the media and a wavelength of $\lambda = \lambda_D = 5893\text{Å}$, then $\beta = 2.92 \times 10^{-4}$. The Cauchy formula can also be used:

$$\beta = \left[2875.66 + 13.412/(\lambda^2 \times 10^{-8}) + 0.3777/(\lambda^4 \times 10^{-16})\right] \times 10^{-7}$$

The values of $\beta$ used in the present computations were chosen to match those used in the reduction of the experimental data. The wavelengths of interest for SOFIA range from the near infrared, $1\mu$m, to the microwave, 1 mm, where optical distortion can be seen to be more severe for shorter wavelengths.

Finally, to obtain a measure of the loss in irradiance due to the fluctuating density field, the $OPL$ for vacuum conditions is subtracted from the $OPL$ through the gas to yield the optical path difference ($OPD$). The value of $< OPD' >$ is computed using a sequence of $OPD$'s at a fixed station. Using the root-mean-square wavefront distortion $< OPD' >$, the phase distortion ($\Phi$) is found from $\Phi = \frac{2\pi\sigma}{\lambda}$. The Strehl ratio, given by

$$\frac{I}{I_0} = e^{-\Phi^2}$$

is a measure of the peak intensity to which a beam can be focused. The computational expense of the procedure outlined above is currently $250\mu s$/hexahedron/ray on a single processor of the Numerical Aerodynamic Simulator Cray 2.

In these studies, the effect of fluids upon the optical field is determined through prismatic modelling of the density field. Integration of the equations of motion through a trilinearly varying density field could also be implemented. The use of a six-tetrahedron decomposition would eliminate the present requirement of a checkerboard cell arrangement to prevent gaps between hexahedrons. The modelling of the wave-like nature of light could also be implemented via the parabolized Helmholtz equation if diffraction effects were deemed significant [88].

# Chapter 5

# Results and Discussion

## 5.1 Blast-Wave Results

The methods introduced in the previous sections are applied to test cases which demonstrate the capabilities of the algorithm. The viscous term treatment in a low Mach number regime is shown by the Couette flow problems, which are compared to similarity solutions and previously obtained numerical results. Demonstration of the inviscid term treatment is shown by capturing of transient discontinuities for a shock tunnel start-up problem. The three-dimensional results are compared with an experimental study of a hemicylinder mounted in a shock tube.

### 5.1.1 Couette Flow

The Couette flow problem is used to compare the present methods against the method of Beam and Warming [7] and the similarity solution as given by Schlichting [89]. The results for the two upwind methods fall virtually on top of each other, and $n$ indicates the time step. The solutions shown in Fig. 8 were obtained using quiescent initial conditions and viscous boundary conditions with no-slip adiabatic walls. Both of these cases were implemented in the thin-layer form at a Reynolds number of 6.4, based on the distance between the plates, equal to $10^{-5}$ feet. During the course of these solutions, slightly more than an order of magnitude drop in $|\delta\rho|_{max}$ per two subiterations was observed in the (3 × 10) cell domain. The Courant number used for the oscillating plate calculation was approximately 10, indicating the viability of these types of unsteady computations at Courant numbers greater than unity. The Courant number was computed using $CFL = \frac{\Delta t}{V} max[|(\widehat{U}, \widehat{V}, \widehat{W})| + c]||s||$ over each cell in the domain. Identical results were obtained using both the two- and three-dimensional implementations in all directional permutations. Results reveal slightly steeper gradients than that of the conventionally differenced scheme or the analytic solution, a possible consequence of the handling of the boundary conditions or the viscous term treatment. In addition, this case was found to be insensitive to the choice of the higher-order flux correction terms, possibly because of the dominance of diffusive effects.

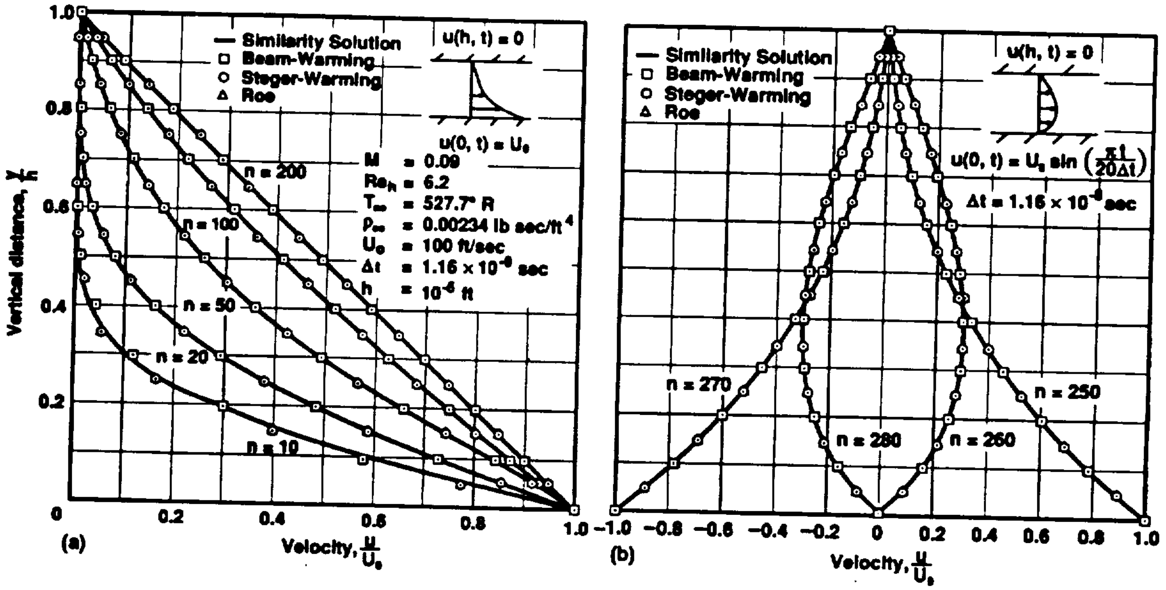

Figure 8: Couette flow case: (a) impulsively started and (b) oscillating plate

## 5.1.2 Shock Tunnel Start-up Problem

The third test case evaluated the inviscid term treatment through the simulation of the transient starting process of a planar shock tunnel. The (300 × 60) cell domain is shown in Fig. 9. The solution of the Euler equations is presented in Fig. 10 as a comparison of experimental and numerical shadowgraph images, the former due

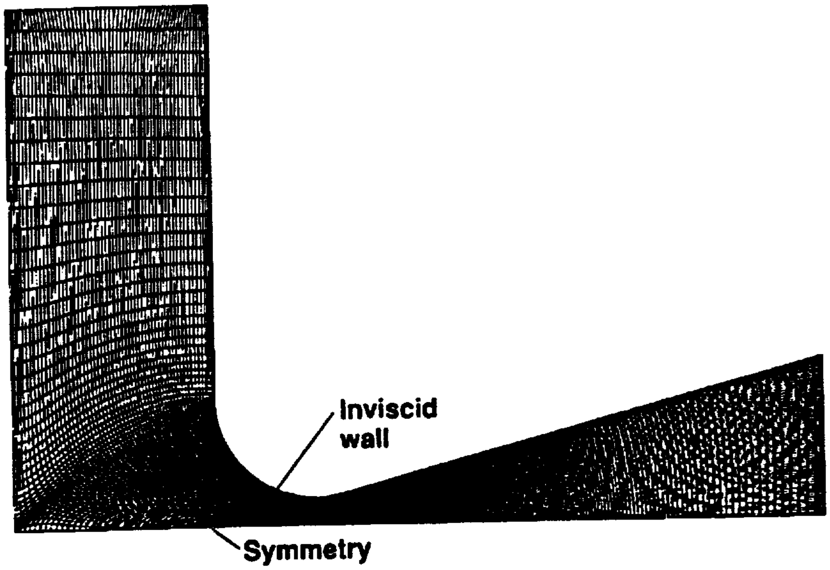

Figure 9: Shock tunnel case: 300 × 60 cell grid

to Amann [90]. The computed shadowgraph function is proportional to $\nabla^2 \rho$ and thus acts as an amplifier of the density gradient across contacts and shocks, for instance. This solution was obtained using Roe flux difference splitting with $\phi = 1/3$, the upwind biased flux evaluation. The Steger-Warming flux evaluation with Roe averaging was found to be moderately less stable, but no significant differences in the results were found for this case. The maximum compression parameter was used, and the entropy-fix parameter used in Harten's formulation [9] was set to 0.15. Disconcertingly nonphysical solutions were produced for smaller entropy-fix levels, possibly associated with an entropy-violating condition. The problem was initialized with a moving shock propagating to the right at a Mach number of 2.97, while the boundary conditions were specified as impermeable inviscid along the walls and fixed for the inlet and exit. For the maximum Courant number of four used here, four subiterations were chosen per time step based on a subjective judgment of discontinuity sharpness. The $|\delta\rho|_{max}$ was observed to drop approximately an order of magnitude over the course of these four subiterations.

Physically, this nozzle starting process generates a high enthalpy reservoir of more than 50 times the initial pressure, while the density increases by 11 times the initial

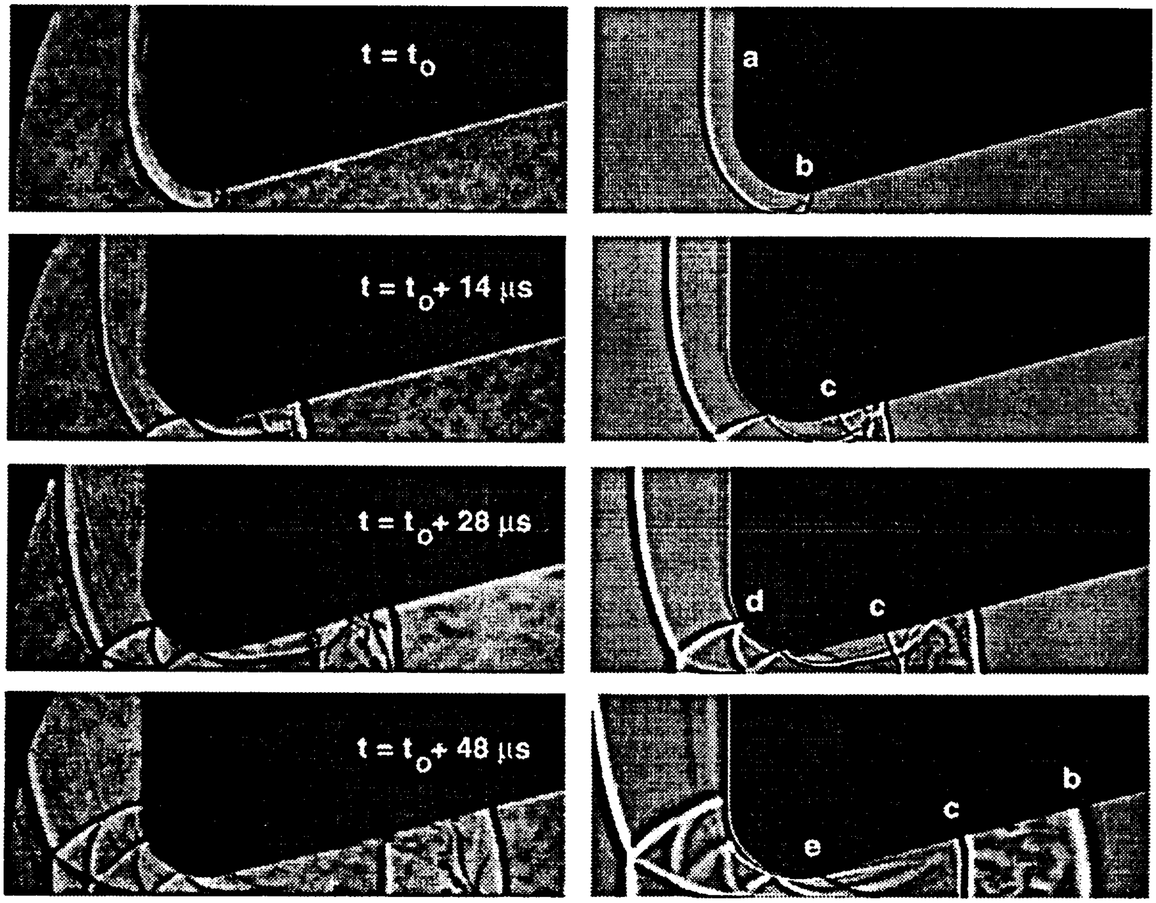

**Experiment, Amann (Ref. 90)** **Euler**

- **(a) Primary shock reflected into reservoir**
- **(b) Swallowed primary shock**
- **(c) Rearward facing shock being swept downstream**
- **(d) Reflected shock system**
- **(e) Mach line generated from $C^2$ discontinuity**

Figure 10: Shock tunnel case: shadowgraph comparison for a Mach 3 planar shock

state. This reservoir provides the energy necessary to generate high Mach flows downstream of the diverging nozzle region for short durations. The ensuing reflections of the shock with the nozzle wall reveals the complexities of the shock-shock and shock-contact interaction. In particular, it can be seen that the development of the rearward facing shock, which is directed upstream while being swept downstream, is resolved. At later times, the finer scale fluid motion between the primary and rearward facing shocks is, for the most part, lost because of grid coarseness and attendant numerical dissipation. However, increasingly fine structures are captured as the grid is refined.

### 5.1.3 Shock Tube Blockage Study

The viability of the technique in three-dimensions is shown by the final test case. These results are intended to replicate the conditions in an experimental study of a blast-wave encounter with a hemicylinder target in a shock tube by Kingery and Bulmash [91]. The experimental test configuration and pressure transducer locations are shown in Fig. 11. In order to estimate the costs and benefits of inviscid versus viscous simulations, the flow about this geometry was computed using both the Euler and Navier-Stokes equations. However, the expense of these three-dimensional simulations permitted the use of only one of the inviscid flux evaluation methods; the Roe flux difference splitting was chosen.

The simulation was initialized as a translating planar shock before diffraction over the cylinder began. Initial conditions were specified as:

$$\begin{array}{ll} M_s = 1.518, & Re/m = \frac{\rho_\infty c_\infty}{\mu_\infty} = 23.3 \times 10^6/m \\ T_\infty = 288.17\ K, & p_\infty = 101.3 \times 10^3\ N/m^2 \end{array}$$

Boundary conditions are specified for the viscous, single zone computation as shown in Fig. 12. In the shock-tube direction, the $\xi$-direction, extrapolation is used. This non-physical extrapolation is adequate for the duration of the early interaction. However, solutions at larger times are suspect, where times after the shocks have propagated through the boundaries are defined as large. Additionally, the use of an advancing front boundary is enabled because of a priori knowledge of the grid structure and the

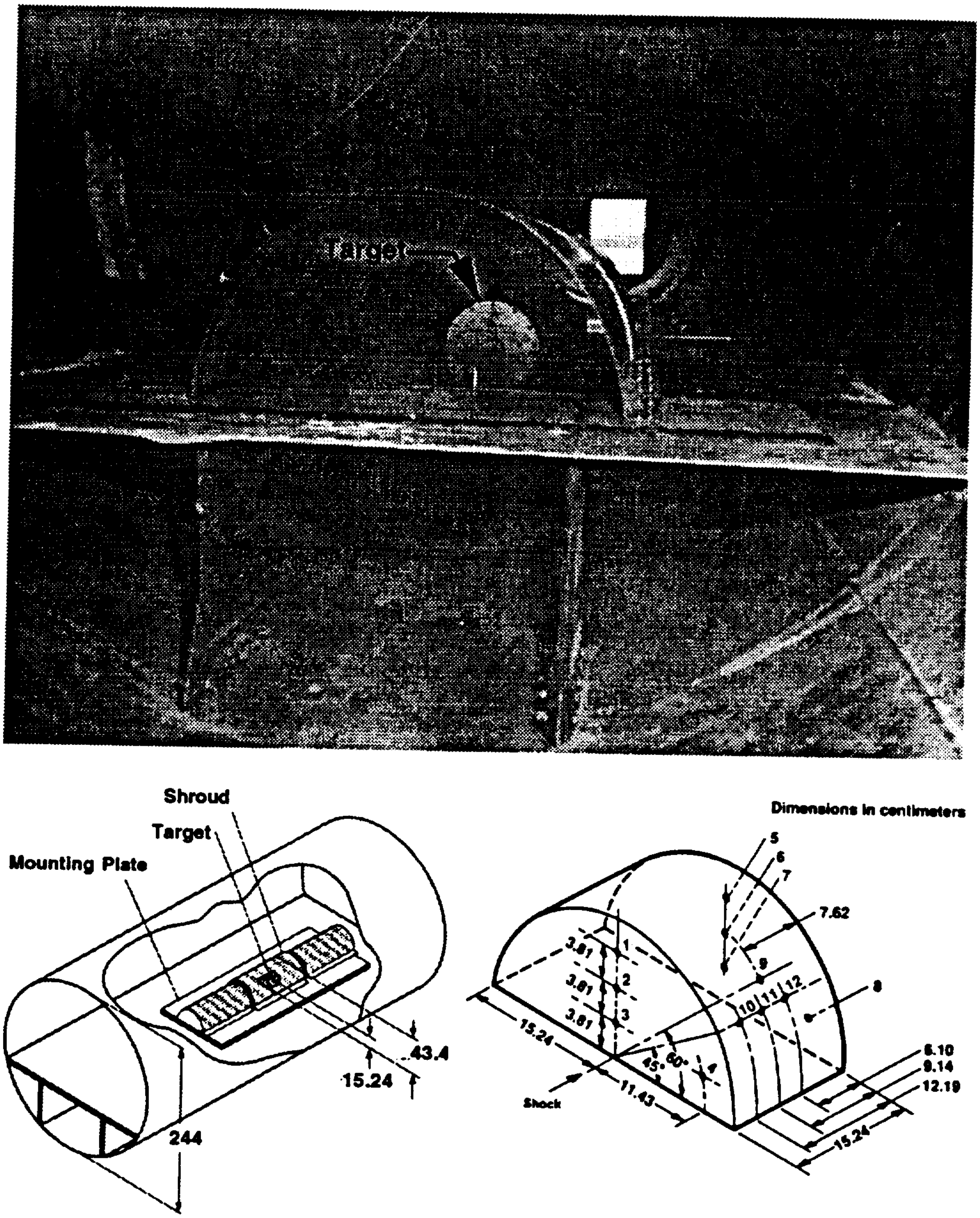

Figure 11: Hemicylinder case: experimental configuration and pressure transducer locations

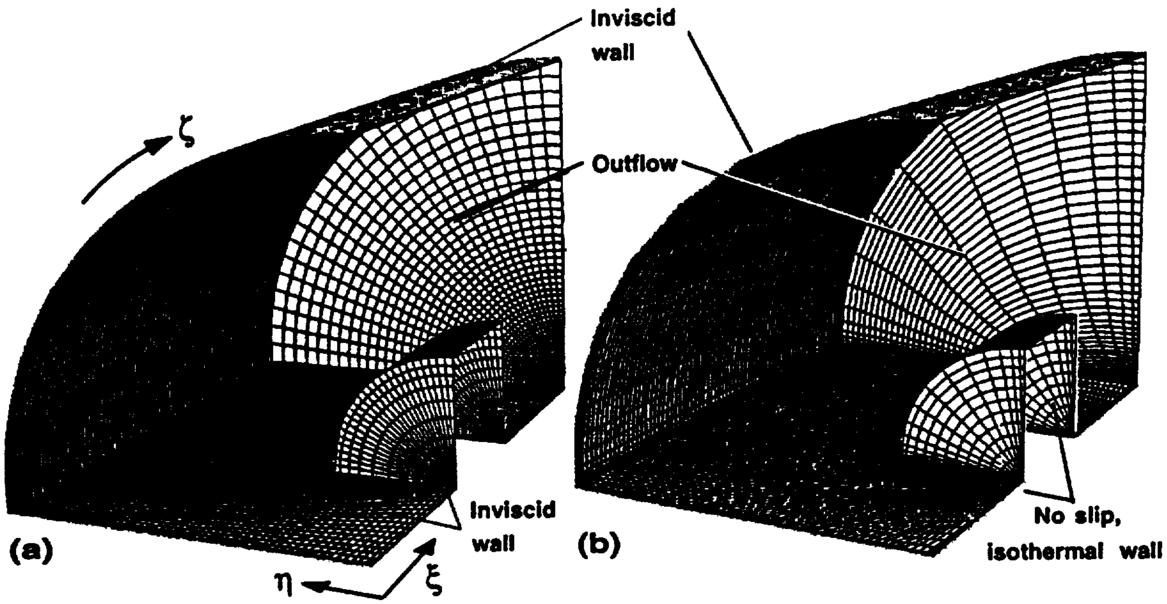

Figure 12: Hemicylinder case: central region of the 78 × 50 × 25 cell (a) inviscid and (b) viscous grids

primary shock speed. This simple time-dependent boundary reduces the computation time by using the fact that nothing occurs ahead of the blast-wave. In the $\eta$-direction, the lower boundary defines the surface geometry of the hemicylinder, and hence is specified as a no-slip isothermal wall. The top of the domain in the $\eta$-direction, corresponding to the inner radius of the shock tube, is specified as an inviscid wall, based on the assumption that the viscous effects on this surface have negligible influence on the results. Finally, the $\zeta$-direction boundaries are treated using the viscous condition along the floor of the tube. Symmetry conditions are used along the plane running along the longitudinal axis of the cylinder and normal to the floor. To simulate experimental conditions, the wall temperature was set equal to the temperature of the quiescent flow prior to primary shock arrival. The viscous grid has normal spacing of approximately $10^{-5}$ meters at the viscous walls. The Euler computation used the inviscid boundary conditions previously discussed where appropriate. For this Euler grid, since the areas of the faces corresponding to the geometric axis singularity are zero then $\vec{F} \cdot \mathbf{s}$ is also zero. Compensation for the round-off error inherent in the grid was implemented by eliminating those face areas which fell below a specified tolerance. The grids and boundary conditions for these cases are partly shown in Figs. 12 and 13.

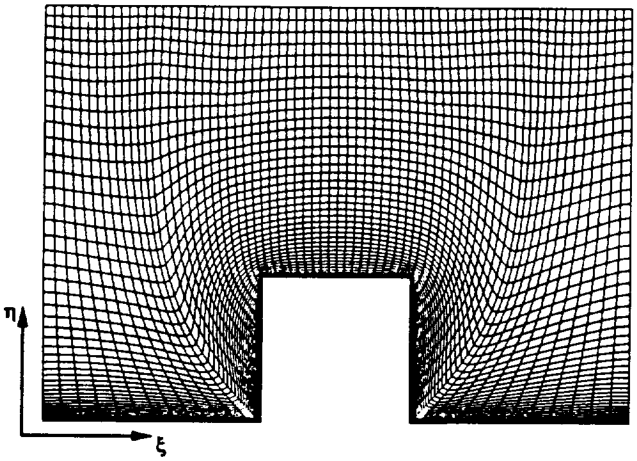

Figure 13: Hemicylinder case: symmetry plane of the central part of the viscous grid

The inviscid computation used $\phi = 1/3$, $\beta = 4$, Harten's entropy fix parameter of $10^{-4}$, Roe flux difference splitting, one subiteration per second-order accurate time step, and a Courant number of 15. The solution was obtained in 1500 time steps without any change of parameters.

The viscous computation used the same flux evaluation as above with the addition of the second-order accurate full viscous terms. Because of the viscous spacing, the Courant number utilized was $10^4$, allowing the solution to be obtained in 6800 time steps with no subiterations. In contrast to the inviscid simulation, the advancing front boundary condition was utilized in this case.

Results, given in Figs. 14 through 17, show that the primary shock is captured over two to three cells, the large physical thickness obtained is an artifact of the coarse grid used. Adaptive gridding methods would help maintain sharp shocks, but the anticipated expense of these methods precluded their use here. Figures 14 and 15 show comparisons of the numerical and experimental pressure histories. It is seen that the peak overpressure is underpredicted by 10%, possibly owing to the coarseness of the grid which in turn thickens the shock. These computed surface pressures were extracted from the domain through the use of a Newton search in three-space for the cell in which the given $(x, y, z)$ probe coordinate fell [92]. Subsequent trilinear interpolation over the cell, where the uniform parametric coordinates $(u, v, w)$ are determined from the positions of the vertices of the hexahedral cell, allows the pressure to be computed. Inherent in this first-order approximation lies the assumption that over a discrete cell the variation of pressure is linear in space.

Figures 16 and 17 show portions of the viscous simulation at selected times. Physically, the interaction process begins with the normal impact of the incident shock with the front face of the hemicylinder. At this time, peak overpressures of six times, and densities of four times that of the quiescent state are generated along this forward face. As the shock diffracts over the sharp corner of the target, a separation bubble forms, which eventually envelops a large portion of the circumferential face of the body. This vortical motion is depicted in Fig. 17 by instantaneous streamlines. A supersonic pocket is generated as the air negotiates the sharp corner as it rushes from the stagnation region left in the wake of the upstream propagating reflected shock. The next significant event occurs as the shock diffracts over the rearward face, shedding a strong vortex sheet while an expansion wave propagates away in a pattern which grows with time. The diffracted shock then impacts the floor of the shock tube, reflecting it upwards, while the shock which diffracted over the circumferential face reflects inwards from the outer walls of the tube. A simplified sketch of the interaction process is shown in Fig. 18. The subsequent diffractions and reflections result in the interaction of shocks, expansion fans, vortices, and developing boundary layers. From experimental evidence, this gross unsteadiness does not dissipate for more than 15 milliseconds after the interaction event begins. However, the primary shock passes from the test section 5 milliseconds after the initial target interaction; therefore, the computation is stopped at that time.

The effects of the viscous terms are seen by comparing the pressure histories in Figs. 14 and 15. While the pressures along the upstream face are largely unchanged, the circumferential and downstream faces are significantly affected by viscosity. The large separation along these faces causes low pressure regions due to this vortical motion. This phenomenon is more accurately captured in the viscous simulation, as

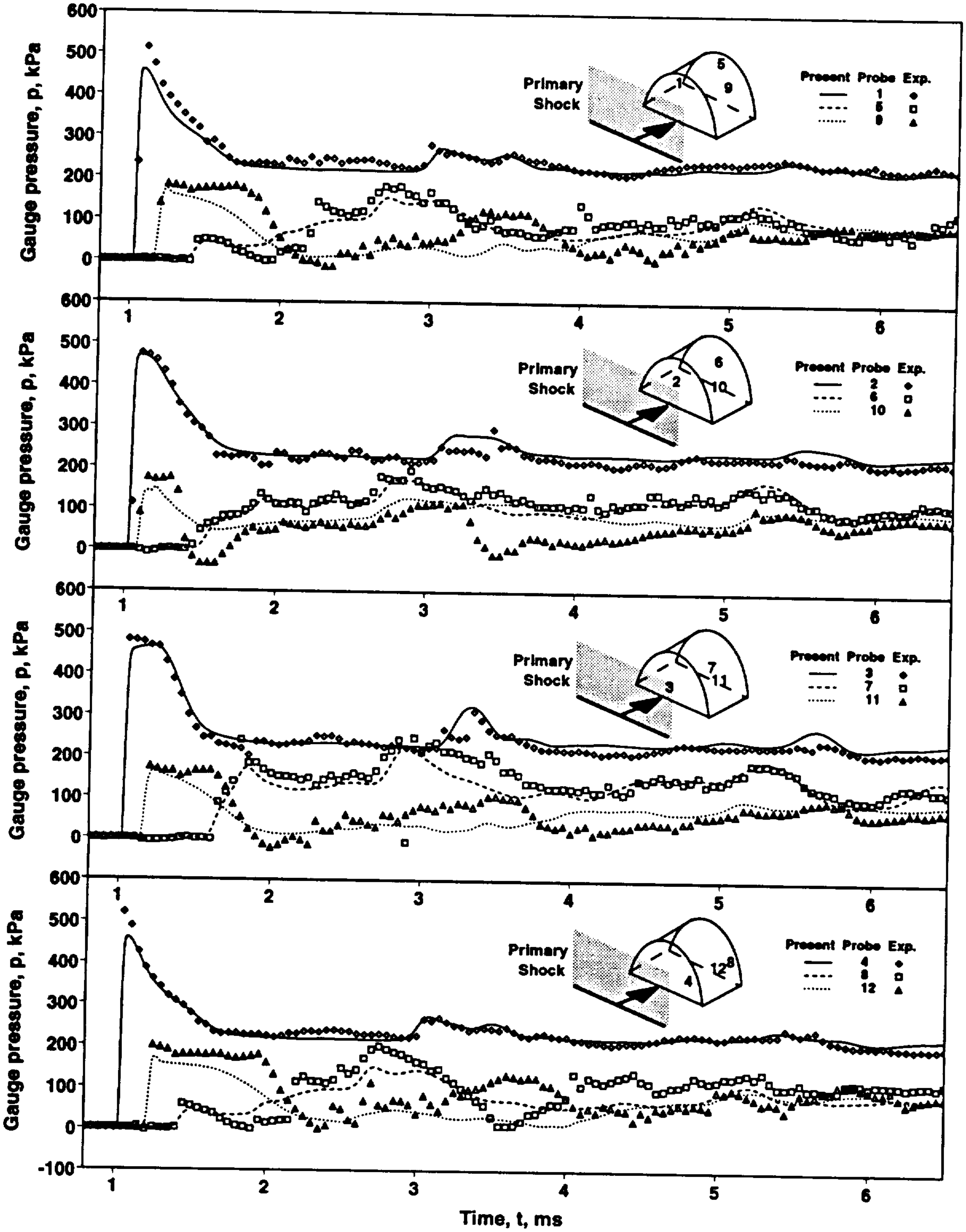

Figure 14: Hemicylinder case: experimental [91] and inviscid computation pressure histories

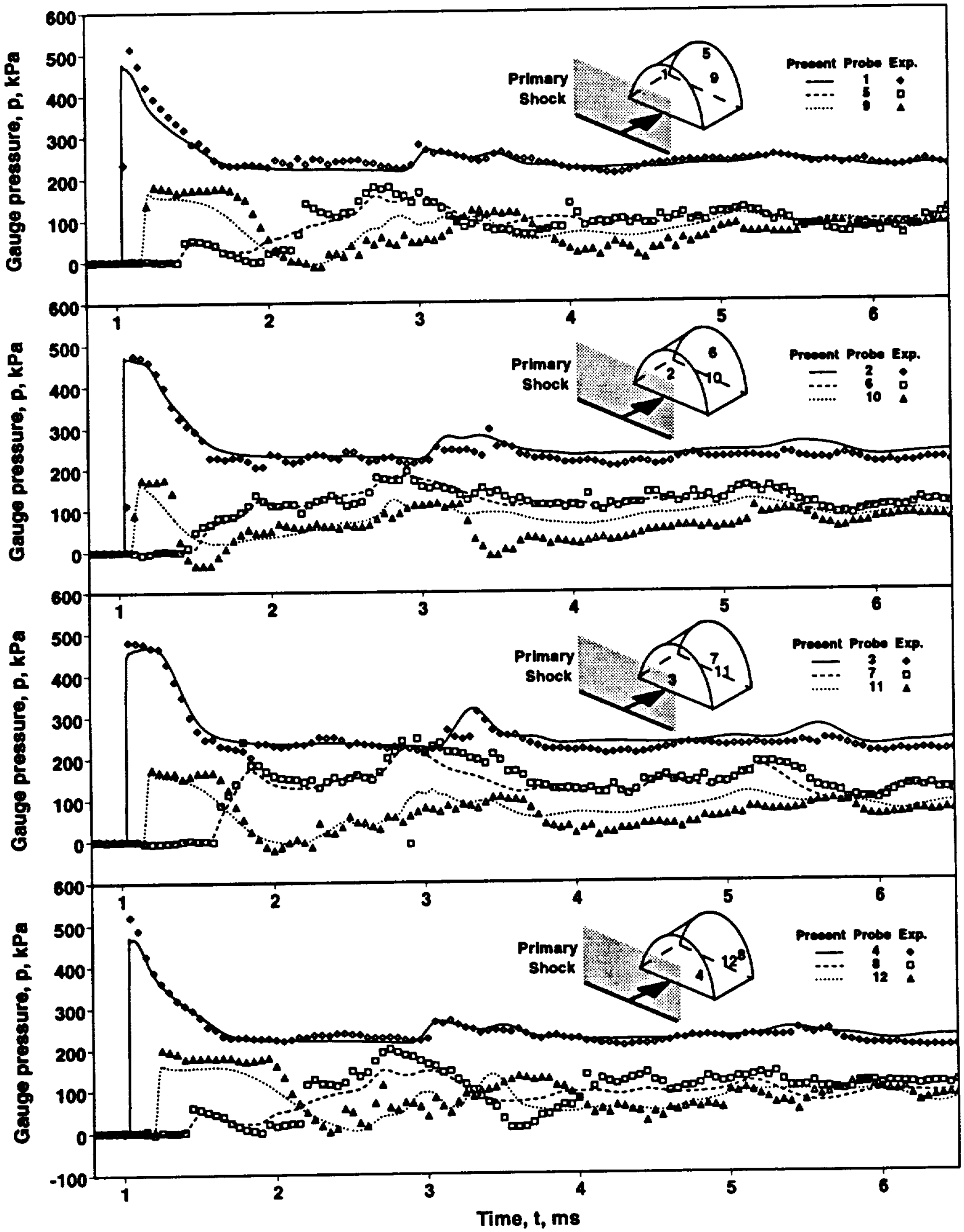

Figure 15: Hemicylinder case: experimental [91] and viscous computation pressure histories

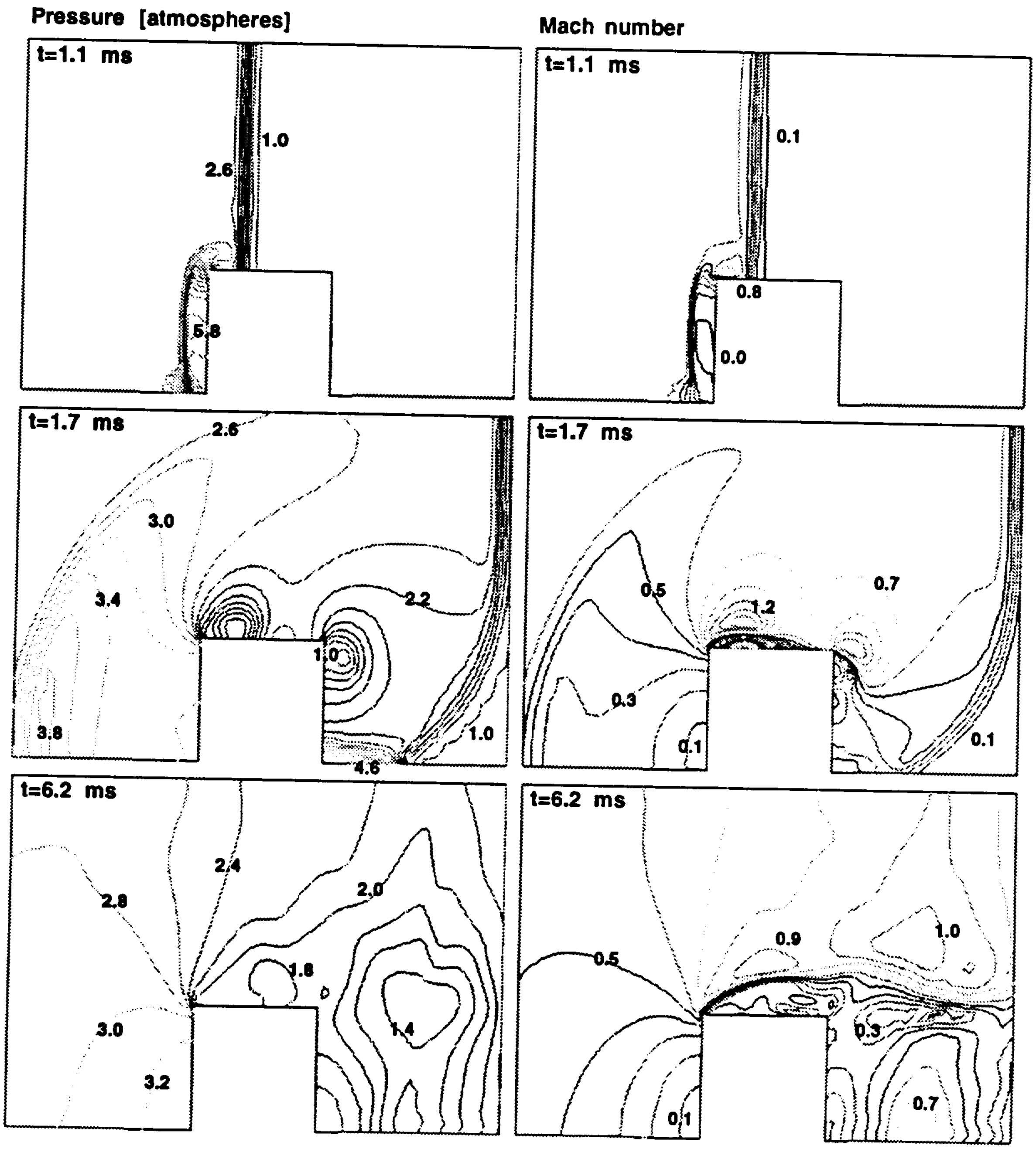
Pressure [atmospheres]

Mach number

Figure 16: Viscous hemicylinder case: symmetry plane pressure [atm.] and Mach contours at (a) t=1.1ms, (b) t=1.7ms, and (c) t=6.2ms

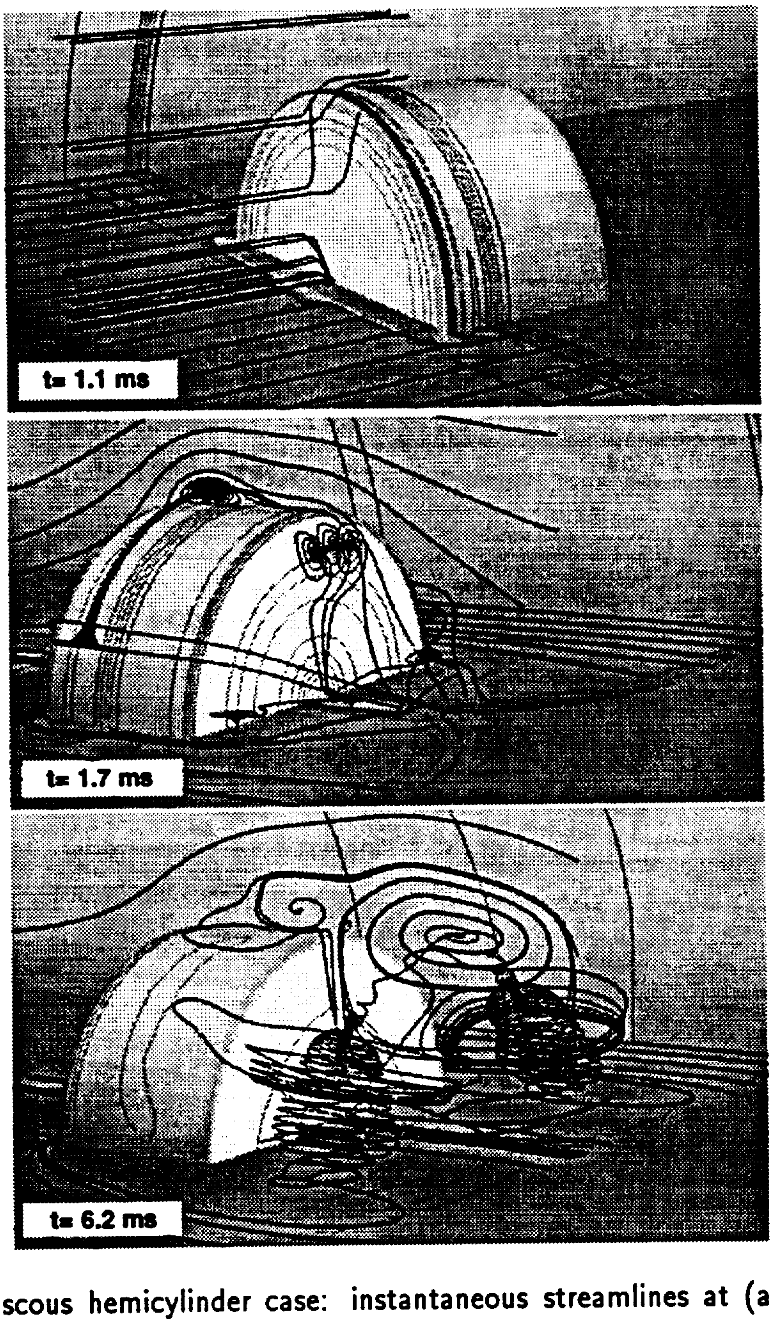

Figure 17: Viscous hemicylinder case: instantaneous streamlines at (a) t=1.1ms, (b) t=1.7ms, and (c) t=6.2ms

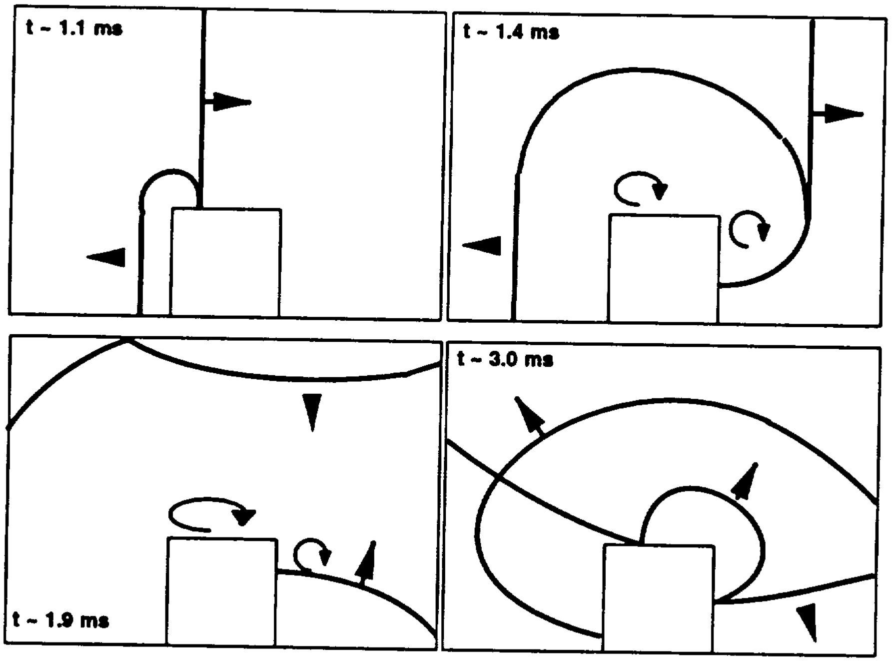

Figure 18: Hemicylinder case: schematic of shock interaction

may be seen by inspection of the pressure histories at probe 11. Differences between the experimental and the present results may be due to poor capturing of the vortex strength owing to grid coarseness. However, the higher-order behavior of the method used here attempts to reduce the need for finely spaced meshes. In addition, the occurrence of deformation of the shroud wall is thought to be a possible event during the experiment, and could adversely affect the comparison between experiment and computation [93].

A limited cost/benefit study of the Euler versus Navier-Stokes equations was also performed for the hemicylinder case. For approximately 5.5 ms of flow history on a (78 x 50 x 25) cell grid, the Euler computation consumed 7.6 processor hours, while the viscous simulation required 18.2 hours. From these results, the somewhat more accurate solution given by the Navier-Stokes simulation may be worthwhile. This is particularly true if the flowfield behavior after the direct interaction the primary shock with the target is important.

## 5.2 Cavity Flow Results

Validation of the diagonalized code was accomplished by evaluation of two- and three-dimensional cases related to the transonic aero-window problem. Numerical results for free shear layer and rectangular two-dimensional cavity flows were compared with analytic and experimental data to evaluate the capability of capturing the fundamental physics. Analysis of the SOFIA configuration simulations, including evaluation of optical distortion is also presented.

### 5.2.1 Free Shear Layer

A series of numerical experiments was performed using a two-dimensional shear layer as the test case. Sensitivities of mean and time-varying quantities to changes in time step size, fourth-order dissipation levels, and grid refinement were determined. Additionally, partial validation of the algebraic turbulent shear layer model was determined through comparison with similarity solutions and experimental data.

The computational domain for this case includes a two inch long splitter plate embedded in a channel, with initial conditions specified as a discontinuous step at the channel centerline. Shown to scale in Fig. 19, the channel extends 30 inches downstream of the splitter plate trailing edge, and five inches above and below the plate. Inviscid walls were specified for three inches upstream of the viscous splitter plate and for the channel walls. The inflow and outflow conditions were implemented using one-dimensional characteristic relations holding mass flow, total enthalpy, and flow angle fixed at the inlets, and fixing pressure at the exit plane. The boundary layers on the splitter plate and the shear layer were turbulent. Reynolds number based on the mean velocity of the streams and the length of the splitter plate was $6.7 \times 10^5$.

The results for three grid refinement levels are shown in Fig. 19 along with Görtler's similarity solution. The velocity profiles are taken 10 inches downstream of the trailing edge of the plate. The solution can be seen to become grid independent when the grid becomes finer than approximately 20 points across the layer. The Mach number ratio for this case was 0.2/0.8 and $\sigma = 20.7$. Eddy viscosity was observed to

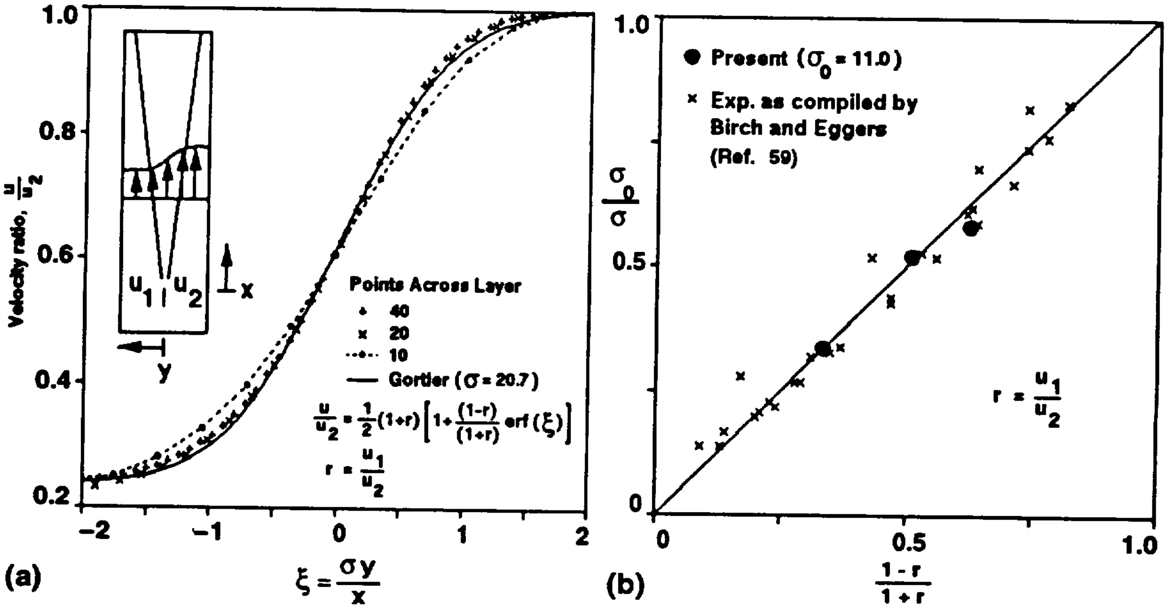

Figure 19: Shear layer case: (a) velocity profiles of differing grid resolution compared to similarity and (b) variation of spread rate with velocity parameter

grow linearly in accordance with the Clauser formulation.

Numerical experiments to determine the dependence of $< p' >$ on the level of fourth-order dissipation showed that a change in fourth-order smoothing from 0.01 to 0.05 caused a change of less than 1% in sound pressure level.

The velocity ratio across the SOFIA cavity shear layer will vary with streamwise location. Hence, comparison of the variation of spread rate with velocity ratio is shown in Fig. 19b. Three velocity ratios are shown for low Mach numbers with about 20 points maintained across the layer for all cases. Although the computed spreading rates are within the bounds of the experimental data [59], the data point at $r = \frac{1}{4}$ falls below the trend because of the limited entrainment afforded by the inviscid side wall treatment.

### 5.2.2 Two-Dimensional Rectangular Cavity

The objective of this two-dimensional cavity case was to demonstrate the prediction of self-induced cavity resonance. Validation data are provided by comparison against

Rossiter's experiment [15]. Sensitivity of the solution to topology, second-order dissipation, and turbulence model effects were determined.

The cavity geometry and grid topology are shown in Fig. 20, where the grid has been coarsened for clarity. The test conditions were set as:

$$M_\infty = 0.9, \qquad Re_L = 1.47 \times 10^6, \qquad L = 8\ in.$$
$$\rho_\infty = 0.40\ kg/m^3, \quad p_\infty = 2.9 \times 10^4\ N/m^2$$

The ratio of cavity length by depth $(L/D)$ was 2 for this model. The inflow boundary was placed 7.5 L upstream of the cavity leading edge, the outflow boundary 4.5 L downstream of the cavity trailing edge. The inflow and outflow conditions were specified as for the free shear layer cases, and an inviscid wall was placed 5 L above the cavity.

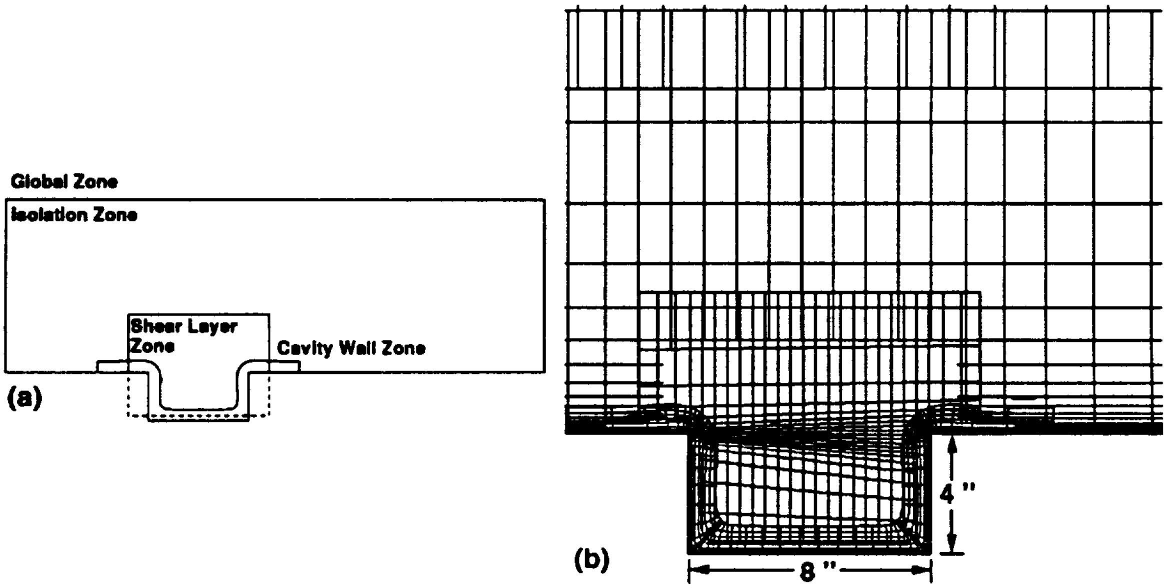

Figure 20: 2-d cavity: topology and grids

Figure 21 depicts instantaneous Mach number and pressure contours obtained during the computation in which the time step size was $\Delta t = 1.97\mu s$. Inspection of the contours across zonal boundaries indicates that the interpolation process is well-behaved for this unsteady flow. The Mach number contours show an instant of the time-oscillatory shear layer behavior which is prevalent for these rectangular geometries. The pressure contours verify the feedback mechanism postulated by

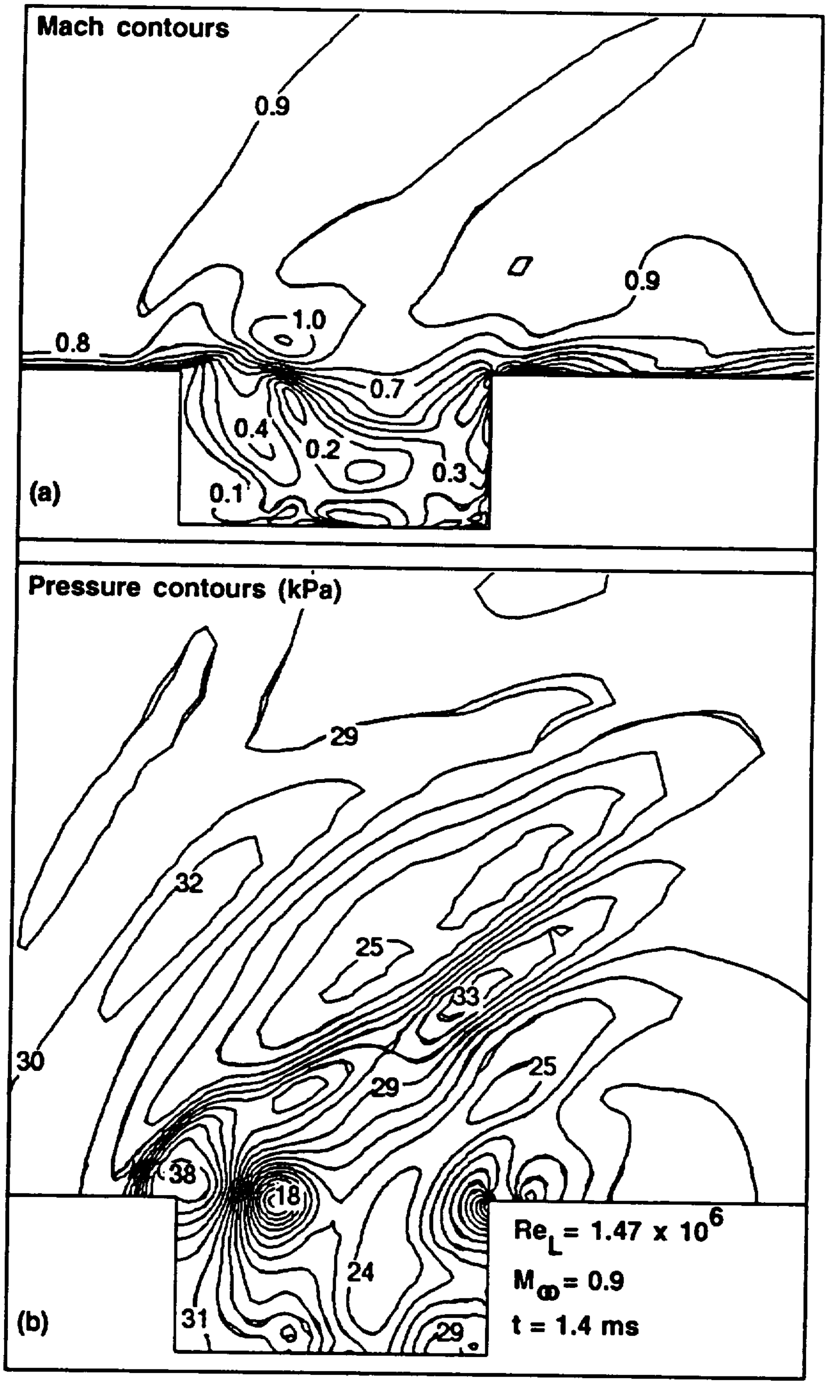

Figure 21: 2-d cavity: instantaneous Mach number and pressure [kPa] contours

Rossiter [15], and shown graphically in Fig. 22. Briefly, the cycle begins with the propagation of a wave from the aft wall of the cavity to the forward face. Wave reflection from the forward wall causes the shear layer to bow outwards, shedding vorticity. The deflected shear layer convects downstream and induces another cycle.

The origin of this physical model can be linked to the edge-tone phenomena, where a thin planar jet interacts with a wedge. The frequencies at which this feedback is reinforced is determined by ambient temperature and Mach number and was first quantified by Rossiter. Derivation of this model begins with the assumption that the frequency of the vortex shedding is equal to the cavity acoustic field, $f = \frac{Ku_\infty}{\lambda_v} = \frac{C_T}{\lambda_a}$. The vortical and acoustic field relationships are linked by

$$m_v \lambda_v = L + \gamma_v \lambda_v + K u_\infty t'$$

$$L = m_a \lambda_a + c_T t'$$

from which

$$f = \frac{u_\infty}{L} \frac{(m - \gamma)}{\left(\frac{1}{K} + \frac{u_\infty}{c_T}\right)} \tag{7}$$

where the phase lag factor, $\gamma = \gamma_v = 0.25$, and the normalized convection velocity of the perturbations, $K = 0.66$, are empirically determined constants dependent on the geometry and ambient conditions. The integer stage number is given by $m = m_a + m_v$. Use of the a Mach number scaled by the cavity speed of sound, determined by the recovery temperature, offers improved correlation with experiment. The model described here is idealized: the shear layer perturbations may be manifested as a sinuous motion as opposed to discrete roller vortices depicted in Fig. 22.

The pressure histories along the cavity walls are depicted in Fig. 23 along with the comparison of Rossiter's data to present results in power spectral density ($PSD$) form. The comparison against experiment shows agreement in frequency at the peak magnitudes. Magnitudes are higher for the present case by about 2 dB, however for this experiment and other numerical work this has been observed as an effect of cavity width. In these studies [15, 36], the sound level was found to be inversely related to $L/W$; the cavity for Rossiter's experimental work was of $L/W = 2$. Also shown in Fig. 23 are the first four stages, $m_i$, predicted by Eq. 7 using both his

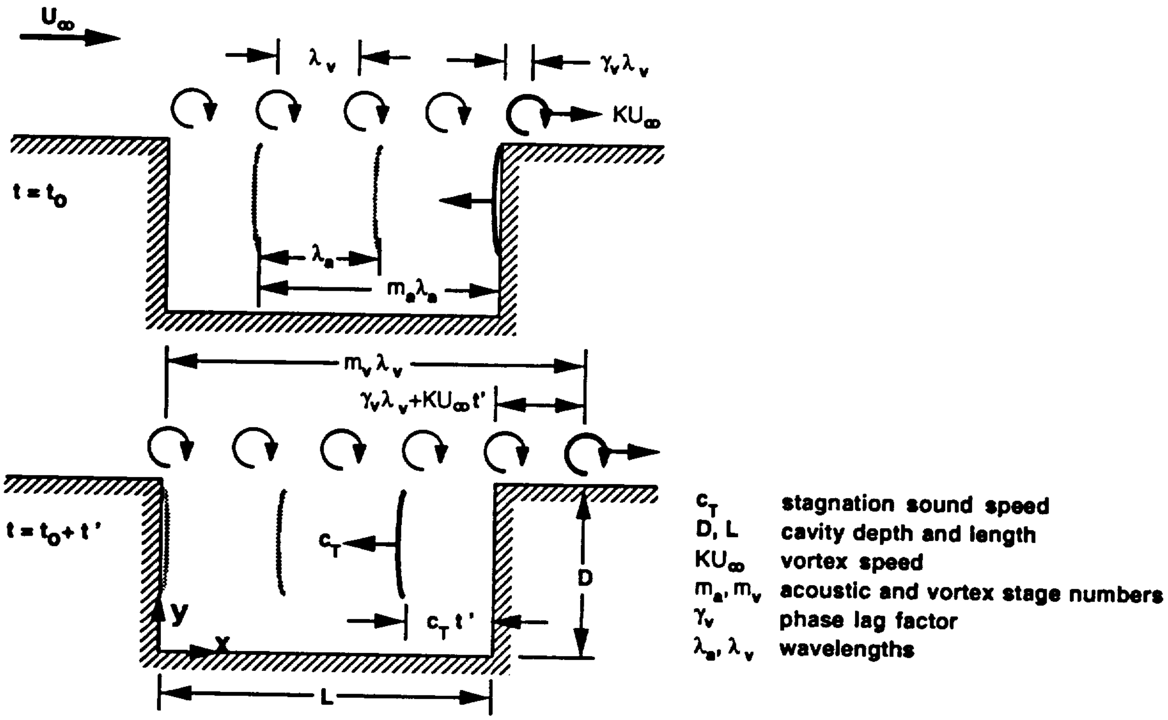

Figure 22: Rossiter's feedback model

vortex convection ratio of $K = 0.66$ and a $K = 0.56$ inferred from the treated cavity computation discussed below. The *PSD* for this case was computed using 8192 time samples, no zero-padding, and a square window.

Variation of the second-order dissipation, $\epsilon_2$, from 0.5 to 0.3 caused no discernable change in the pressure histories. Additionally, in order to test a hypothesis of a limited domain of unsteadiness, an isolation zone was implemented as shown in Fig. 20. The flow outside the zones of interest was frozen, resulting in a decrease of the cavity sound pressure levels by 2%. A final comparison between experimental data and numerical results is provided in Fig. 24, where the variation of the mean and oscillatory pressures along the cavity walls is shown. The $< C_p' >$ is computed following Rossiter's reduction of experimental pressure histories

$$\left[\Delta < C_p' >^2\right]_P = \epsilon \left\{ \left( \frac{p_\epsilon}{q_\infty \sqrt{\epsilon}} \right)_P^2 - \left( \frac{p_\epsilon}{q_\infty \sqrt{\epsilon}} \right)_R^2 \right\}, \quad \epsilon = 0.155$$

where $P$ and $R$ indicate peak and background pressure levels. The computational

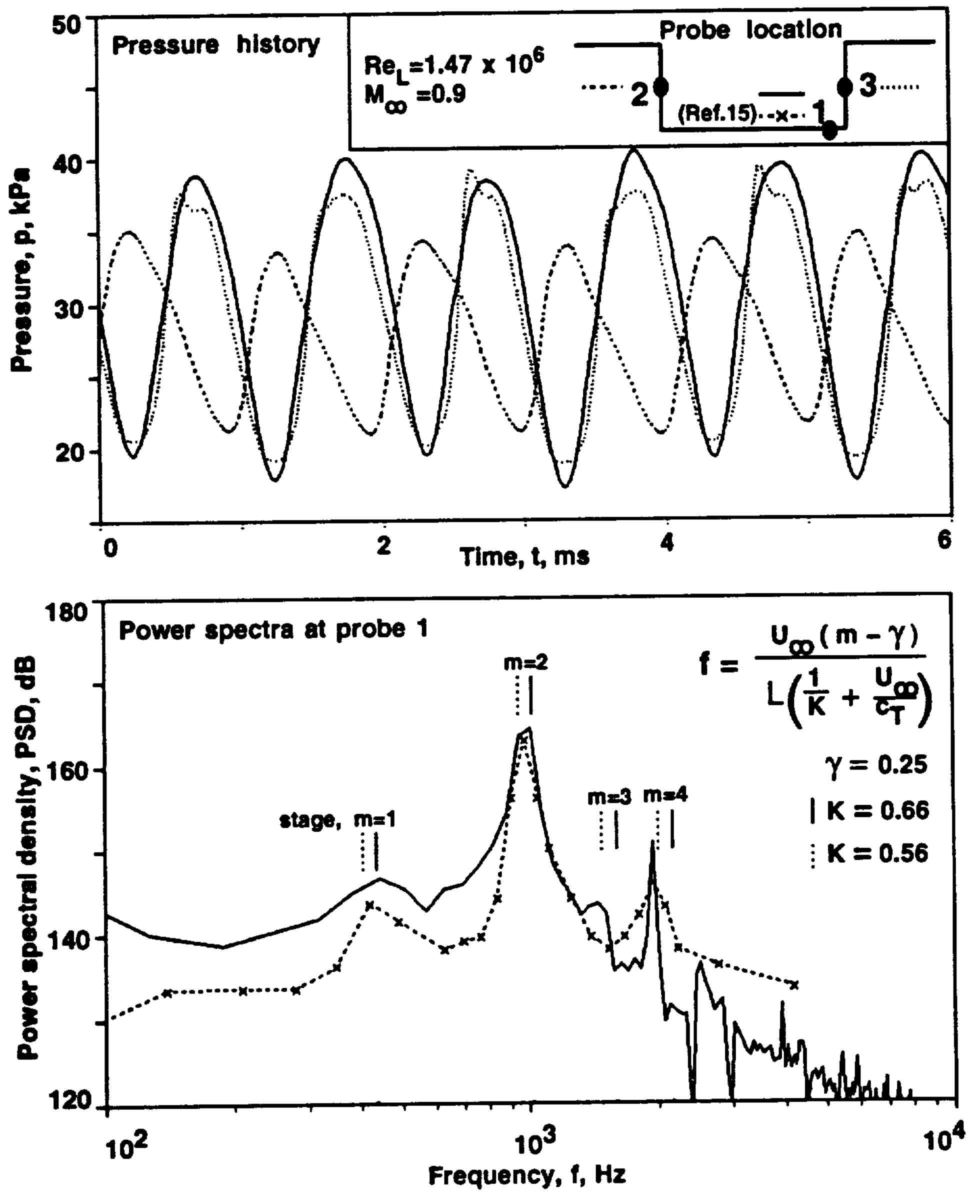

Figure 23: 2-d cavity: pressure history and power spectra comparison

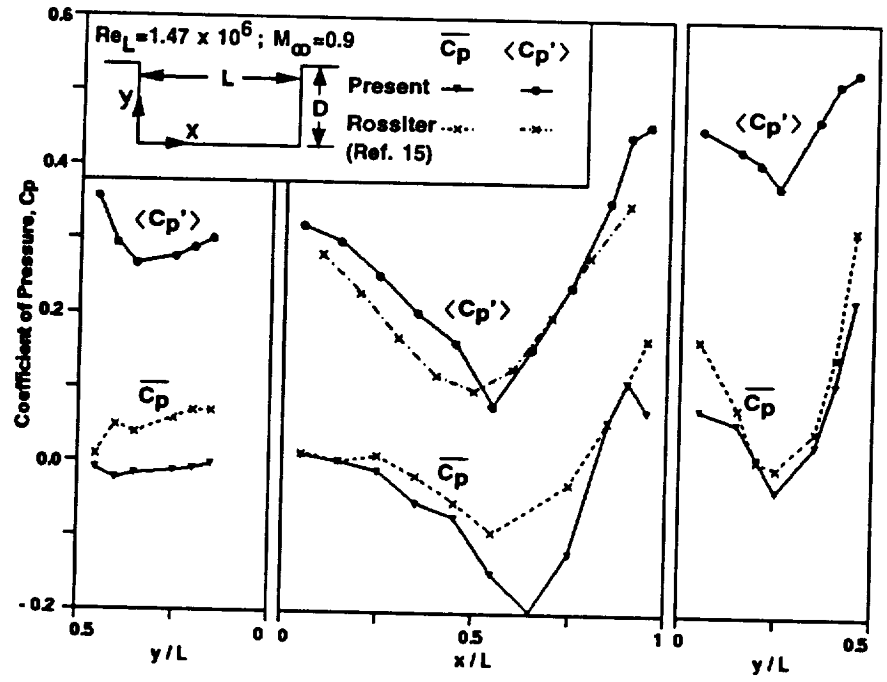

Figure 24: 2-d cavity: variation of mean and oscillatory pressures

results were reduced from assuming $p_\epsilon|_R = \bar{p}$ and $p_\epsilon|_P = p$. Use of Reynolds averaging, specifically $\overline{fg} = \bar{f}\bar{g}$, gives a result consistent with the experimental reduction

$$
\begin{aligned}
< C_p' > &= \sqrt{\frac{1}{N}\sum_i^N \left(\frac{p_i'}{q_\infty}\right)^2} = \sqrt{\frac{1}{N}\sum_i^N \left(\frac{p_i - \bar{p}}{q_\infty}\right)^2} \\
&= \sqrt{\frac{1}{N}\sum_i^N \left(\frac{p_i^2 - \bar{p}^2}{q_\infty^2}\right)}
\end{aligned}
$$

Given the difference in spatial dimensions and turbulence modelling uncertainties, the trends shown in Fig. 24 appear reasonable for a flow of this complexity.

Finally, to give a qualitative comparison of numerical and experimental [17] results, schlieren images are shown in Fig. 25. Despite Reynolds and Mach number mismatches and grid coarseness away from the cavity, the observed and computed acoustic radiation patterns are similar.

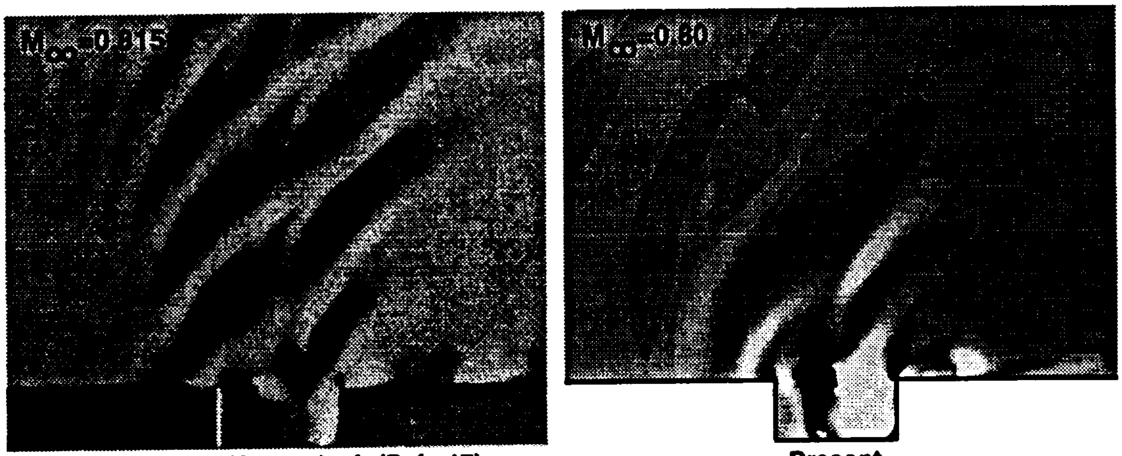

**Experiment, Karamcheti (Ref. 17)** **Present**

Figure 25: Comparison of experimental and numerical schlieren images with knife edge vertical

### 5.2.3 Two-Dimensional Treated Cavity

The effect of cavity geometry, particularly modification of the shear layer attachment region, is known to possess potential quieting capabilities [42]. The Army Airborne Optical Adjunct (AOA), shown in Fig. 26, flight tested several passive and active quieting methods [94]. The purpose of the present numerical simulations is to determine if optical quieting methods, particularly aft ramp treatment and lip-blowing, could be accurately simulated. Tangential lip-blowing at the upstream edge of the aperture may provide quieting by replenishing the mass entrained by the shear layer from the cavity. The quieting provided by aft ramp treatment at the shear layer impingement region is discussed below.

The grid cell size was specified at 0.83″ in the streamwise direction, chosen so that frequencies up to approximately 400 Hz would be resolved without significant numerical dissipation effects. A time step of $44\mu s$ was fixed so that $CFL \approx 1$ in the streamwise direction within the shear layer. The numerical test conditions were matched to flight data:

$$M_\infty = 0.77, \qquad Re_L = 5.00 \times 10^6, \qquad L = 47\ in.$$
$$\rho_\infty = 0.262\ kg/m^3, \quad p_\infty = 1.63 \times 10^4\ N/m^2$$

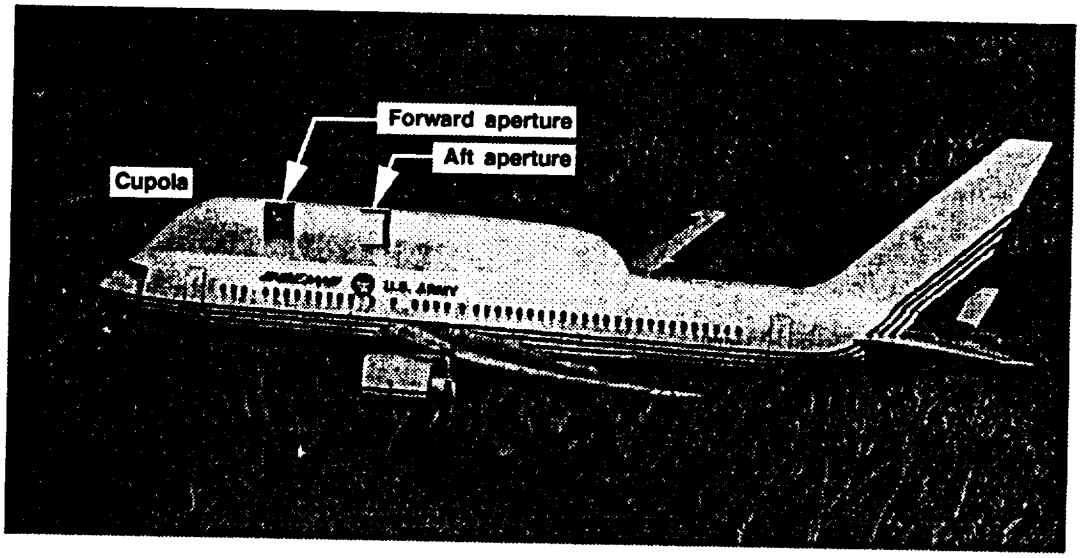

Figure 26: U.S. Army Airborne Optical Adjunct [94]

The initial conditions used the assumption of isentropic recovery to obtain the cavity temperature while maintaining constant pressure across the aperture. Boundary conditions were of the one-dimensional characteristic form: constant mass flow, total temperature, and flow angle inflow; constant pressure outflow; and an inviscid wall 6.4L from the cavity. A characteristic inflow condition was also used for the lip-blowing boundary, the flow rate computed using flight data and assuming isentropic compression of the ram air utilized in the aircraft. The 100% lip-blowing rate case corresponded to a $\dot{m} = 0.42(\rho u)_\infty$. For the discussion below, computed high and low lip-blowing rates refer to 100% and 1% of this mass flow rate. The coarsened near-field grids are shown in Fig. 27.

Comparison of flight data with this planar numerical study is justified by the flight test effort toward establishing two-dimensional flow across the apertures of the AOA. Use of flow cones and a shear layer rake verified, for the most part, the success of this effort. Although the cupola which allows for the cavities is of hemicylindrical form, the center of rotation is through the center of the cavity volume. Rather than simulate an axisymmetric cavity with an erroneous radius of curvature, the cavity was modelled with no spanwise variation in the flow. However, there is a dimensional effect in that the mass removed from the cavity by the shear layer entrainment process can only

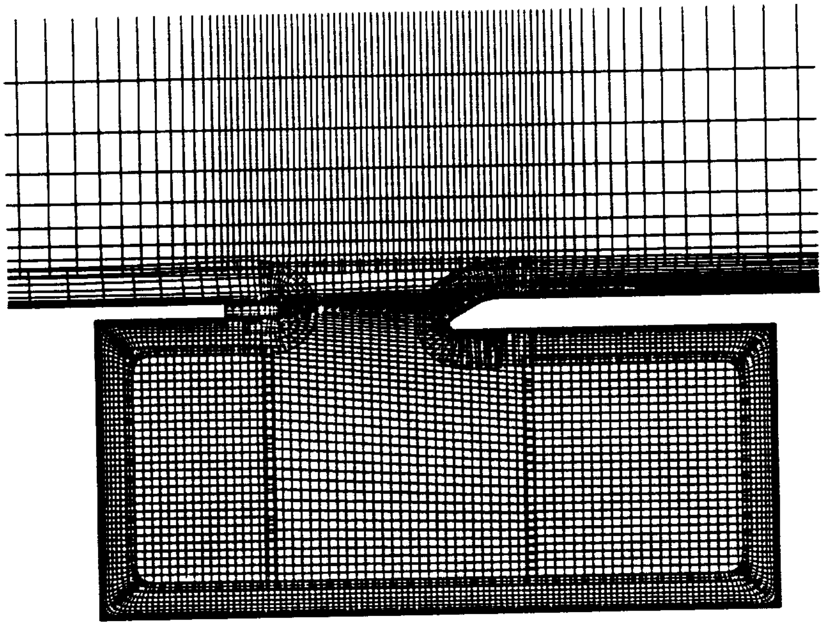

Figure 27: 2-d treated cavity: near field grids

be replenished at the impingement region. This is in contrast to the mass addition mechanism present in three-dimensions, which also includes mass replenishment via spanwise structures such as streamwise vortices.

The mechanism by which an aft ramp reduces the cavity feedback was explained by Heller and Bliss [24]. Assuming two-dimensional incompressible flow, the region immediately surrounding the stagnation point can be treated using a streamfunction approach:

$$\begin{aligned}\Psi &= axy + \frac{1}{2}by^2\\ u &= \frac{\partial \Psi}{\partial y} = ax + by\\ v &= -\frac{\partial \Psi}{\partial x} = -ay\end{aligned}$$

and the resultant field is shown in Fig. 28.

Physically, this result can be explained from a force balance normal to a streamline approaching the stagnation point. About the stagnation point, the velocity gradient across the impinging shear layer creates a pressure gradient. However, there is a

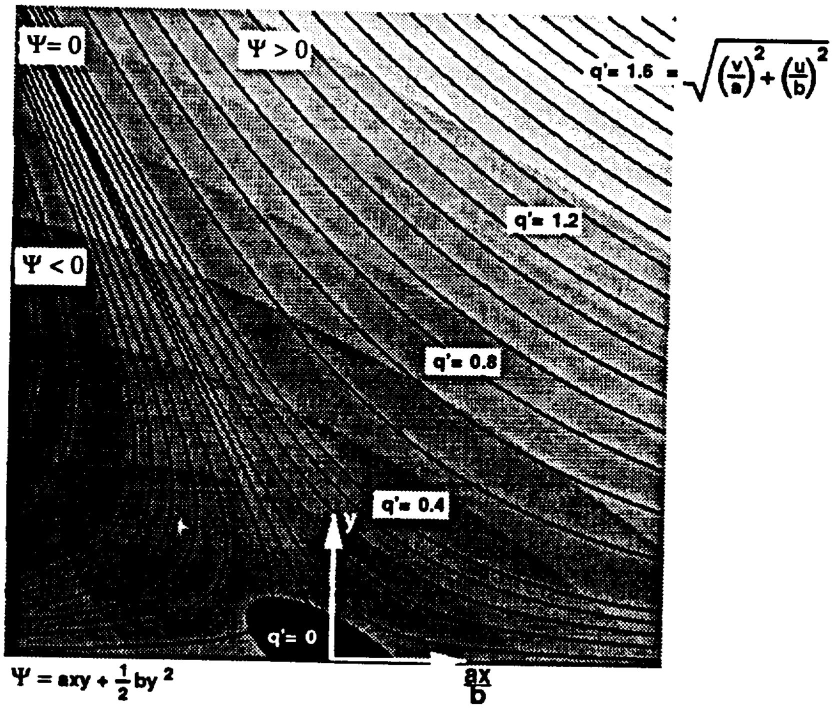

Figure 28: Streamfunction near a stagnation region

counteracting pressure gradient, $\rho q^2/r$, due to the differing radii of curvature above and below the dividing streamline.

For a rectangular cavity, the extreme of normal impingement of the shear layer onto the aft bulkhead causes further deflection into the cavity. Mass ingestion into the cavity causes increased pressure, deflecting the shear layer outwards. With the shear region now outwardly deflected, mass expulsion from the cavity reduces the cavity pressure, inducing another cycle. Therefore, between the extremes of a normal or tangential impingement of the shear layer, a balance of forces may be found. Use of a ramp instead of a convex surface at the reattachment region prevents shear layer perturbations from inducing instabilities of the type seen in rectangular cutouts. The length of the ramp must be large enough to accommodate the magnitude of the transverse shear layer excursions expected during operation.

It is hypothesized that the use of a modestly concave surface at the impingement point may provide increased quieting. Improved stability may be provided by the following reasoning. As the shear layer is perturbed downwards, the streamlines below the impingement point will have a smaller radius of curvature while the streamlines above the shear layer will be less curved. The resultant pressure gradient will drive the shear layer upwards. Conversely, as the shear layer deflects upwards the steeper tangent angle creates a smaller radius of curvature above, forcing the shear layer downwards towards the nominal stagnation point location.

Computed and flight mean Mach number profiles are compared in Fig. 29 for two lip-blowing rates. The quantity $\phi$ indicates the angle from the cupola crest at which the data was measured. Figure 29 also shows Mach number contours for the two lip-blowing rates above each set of profiles. The Mach number contours are instantaneous while the profiles were averaged over 2000 time steps. The difference between experiment and computational results on the lower edge of the shear layer ($r < -2''$) may be due to blockage in the cavity of the aircraft. This blockage was not computationally represented due to the lack of a complete geometry description. The difference at the upper aft portion of the shear layer ($r > 2''$) appears to be due to blockage in the computational model. Overall, the maximum vorticity as a function of x-station is in agreement for both cases.

Comparisons of power spectra at the aft ramp are shown in Figs. 30 and 31. The computed spectra can be seen to be quantitatively and even qualitatively different from flight data. The computed result lies more than 15 dB below the data, and a peak in the low lip-blowing rate spectra is clearly computed, but is not seen in the flight data. The power spectra were computed using 4096 points and a square window. Figure 32 shows mean and fluctuating quantities along the cavity walls, with the available data allowing comparison only along the aft ramp. The computed trend in $< C_p' >$ is in agreement with measured data, but a large discrepancy in magnitude is evident. The large spanwise variation in measured $< C_p' >$ indicates the existence of three-dimensional effects or experimental errors.

It has been noted from experimental evidence [95] that the frequency of large structures in shear layers is independent of axial station and occurs at Strouhal number of $St = \frac{f\theta}{u_1+u_2} = 0.024 \pm 0.003$, where $\theta$ is the local shear layer momentum thickness and $f$ denotes frequency. This phenomena is corroborated by the reduction of other researchers' data [48, 49, 51, 96, 97], whose results range from about $St = 0.02$ to

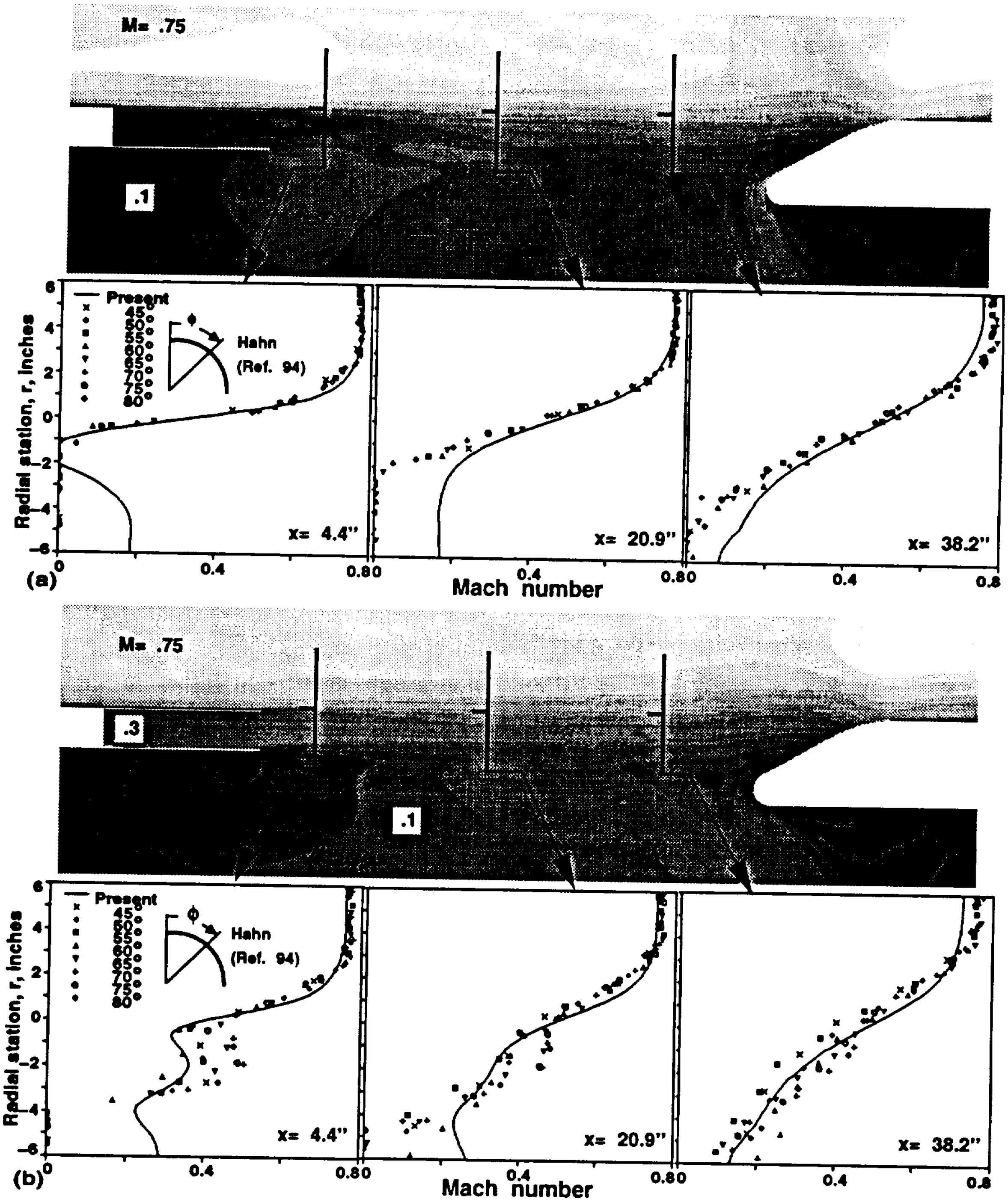

Figure 29: 2-d treated cavity: instantaneous Mach number contours and mean profiles at (a) low and (b) high lip-blowing rate

0.03 for incompressible shear layers.

Görtler's solution can be used to obtain $\theta = 0.036\frac{1-r}{1+r}x$ for $\sigma_0 = 11.0$, which compares favourably to the empirically determined correlation [98] of $\theta = 0.034\frac{1-r}{1+r}x$. Using this relationship along with a compressibility correction [99], the computed peak in the AOA solution at 340 Hz corresponds to a Strouhal number of 0.032. For comparison, the peak at approximately 1800 Hz in the quieted SOFIA case corresponds to a $St = 0.030$, as will be shown in section 5.2.7. It is interesting to note that by using Rossiter's formula, Eq. 7, the frequencies obtained for $m = 4$ and 5 are 285 and 360 Hz, respectively. From Fig. 34 it can be observed that $m_v = 4$, implying that $m_a = 1$.

Based upon these observations, it is hypothesized that large scale shear layer structures are beginning to be resolved. However, the lack of empirical support from the flight data pressure power spectra is at odds with this supposition. The comparison is further clouded by the reasonable comparison in $< \rho' >$ for the low lip-blowing rate shown in Fig. 33. The discrepancy may be caused by three-dimensional effects, angle of attack sensitivity, or geometry simplifications.

In this author's opinion, three-dimensional effects are the most plausible explanation for the discrepancy. Rockwell [100] noted that for sufficiently large Reynolds numbers three-dimensionality reduces coherence in the shear layer. This implies that assumption of two-dimensionality for small flow oscillations may be suspect. The evolution of streamwise-oriented vorticity interacting with the primary vortices would act to spread peaks in the reattachment ramp pressure spectra.

As a final note, Fig. 30 also depicts data, the ordinate scaled by $\frac{q_\infty|_{flight}}{q_\infty|_{tunnel}}$ and the abcissa by $\frac{(c_\infty/L)_{flight}}{(c_\infty/L)_{tunnel}}$, obtained from an AOA wind tunnel test [101]. The data can be seen to agree more closely with the computed results than with flight data, and a small peak exists where expected according to the above analysis.

### 5.2.4 2-D Treated Cavity: Aero-Optical Effects

Computation of aero-optical parameters requires the use of the unsteady density field. Figure 33 shows the computed and experimental profiles of the root mean square of the density fluctuations. Levels of $< \rho' >$ were computed over a time segment of

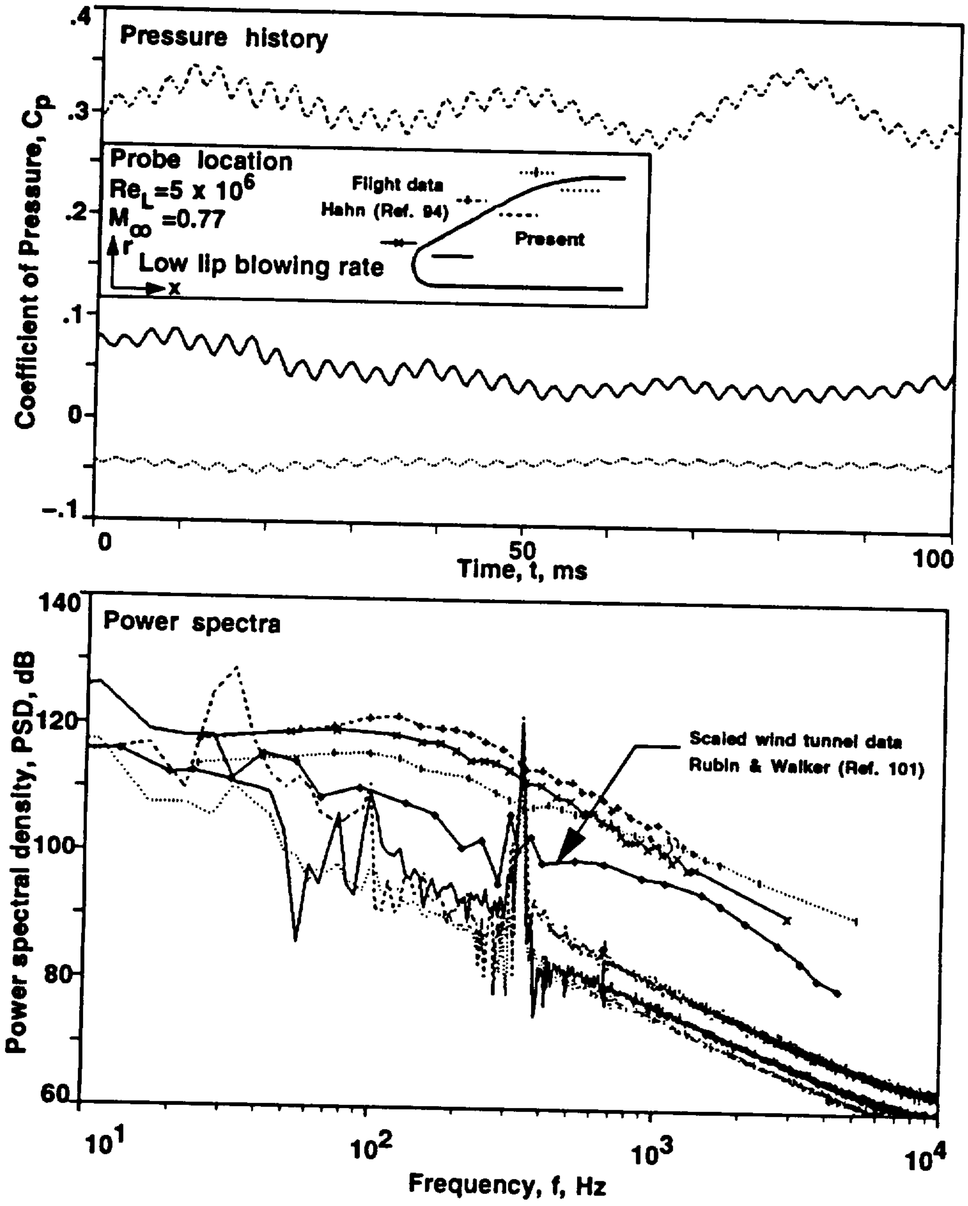

Figure 30: 2-d treated cavity: power spectra, low lip-blowing rate

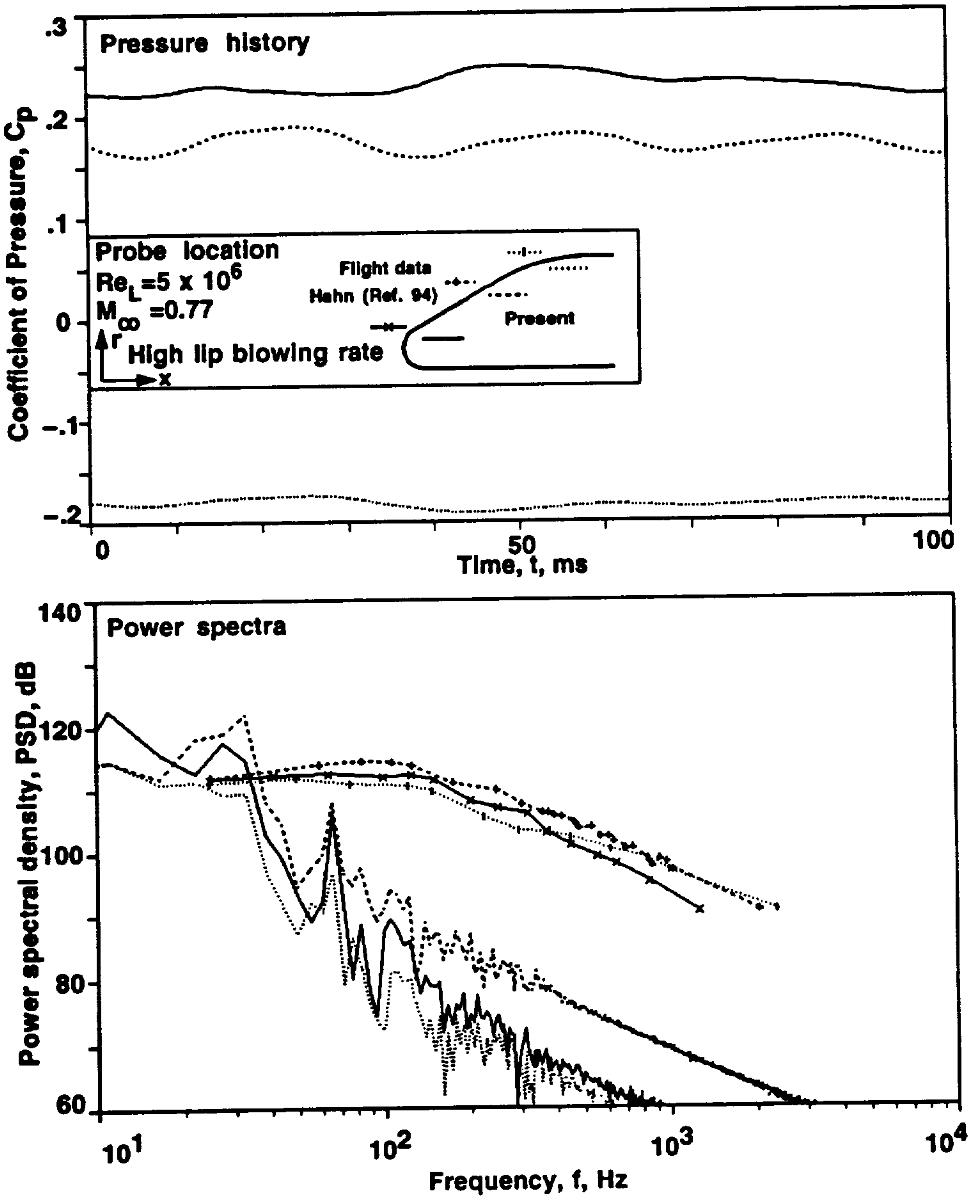

Figure 31: 2-d treated cavity: power spectra, high lip-blowing rate

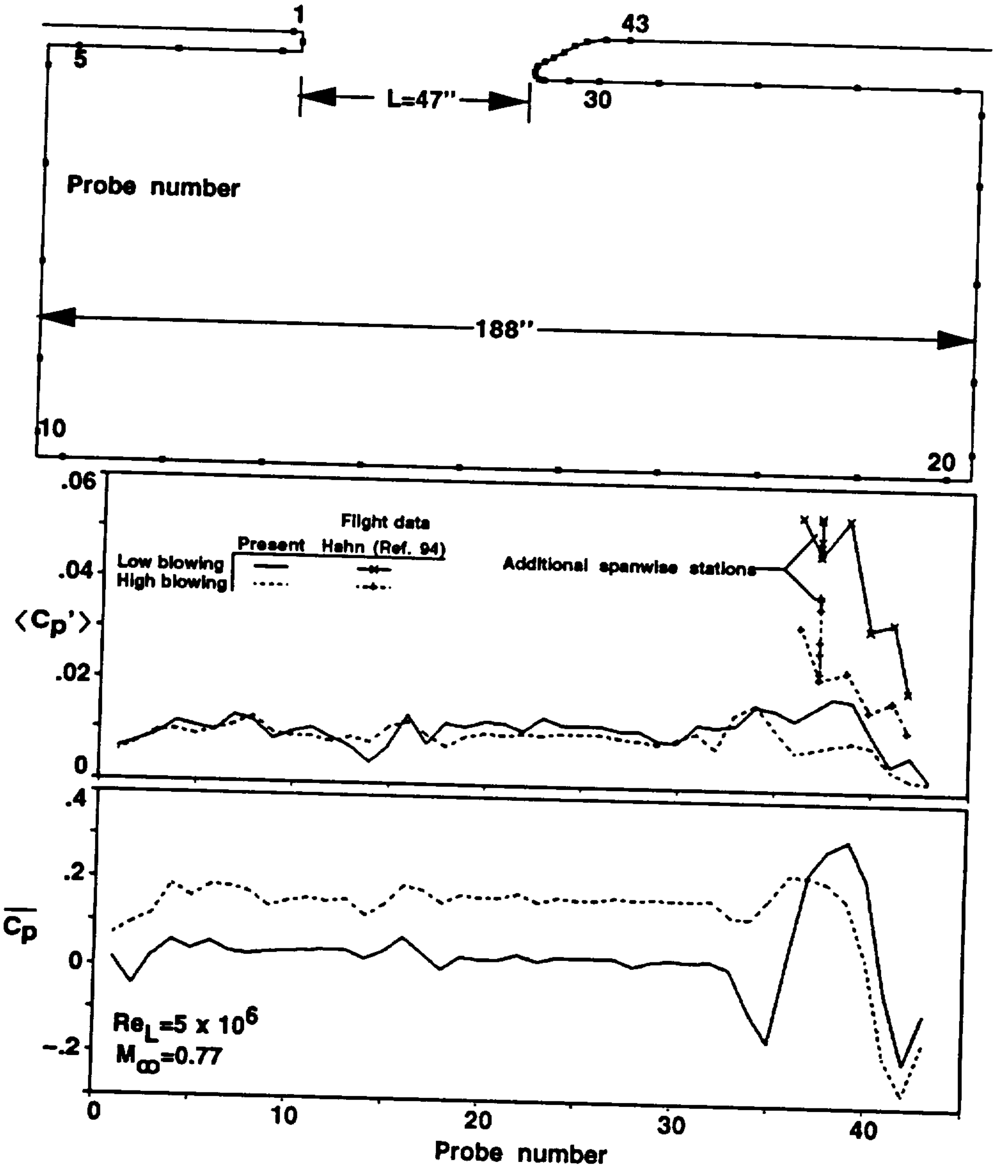

Figure 32: 2-d treated cavity: mean and oscillatory coefficients of pressure

about 90 *ms* in increments of 0.44 *ms*. Using the elapsed time for a particle to convect across the aperture at the mean shear layer speed as a characteristic time, $T_c = \frac{L}{Ku_\infty}$, then the optical computation was taken for about nine $T_c$. In Fig. 33, $\gamma$ is the rake angle from horizontal, with the axis of rotation offset from the cupola centerline. Determination of the systematic error band on the experimental result is discussed below. The low lip-blowing rate result underpredicts the magnitude of the peak in $\frac{<\rho'>}{\rho_\infty}$, however the peak location is in fair agreement. The computed results for the high lip-blowing rate compare poorly to experiment, possibly due to inadequate grid resolution or the increased flow complexity of the merging shear layers. This type of active control is presently not a design option for SOFIA, therefore further effort toward improvement of the high lip-blowing case was not warranted.

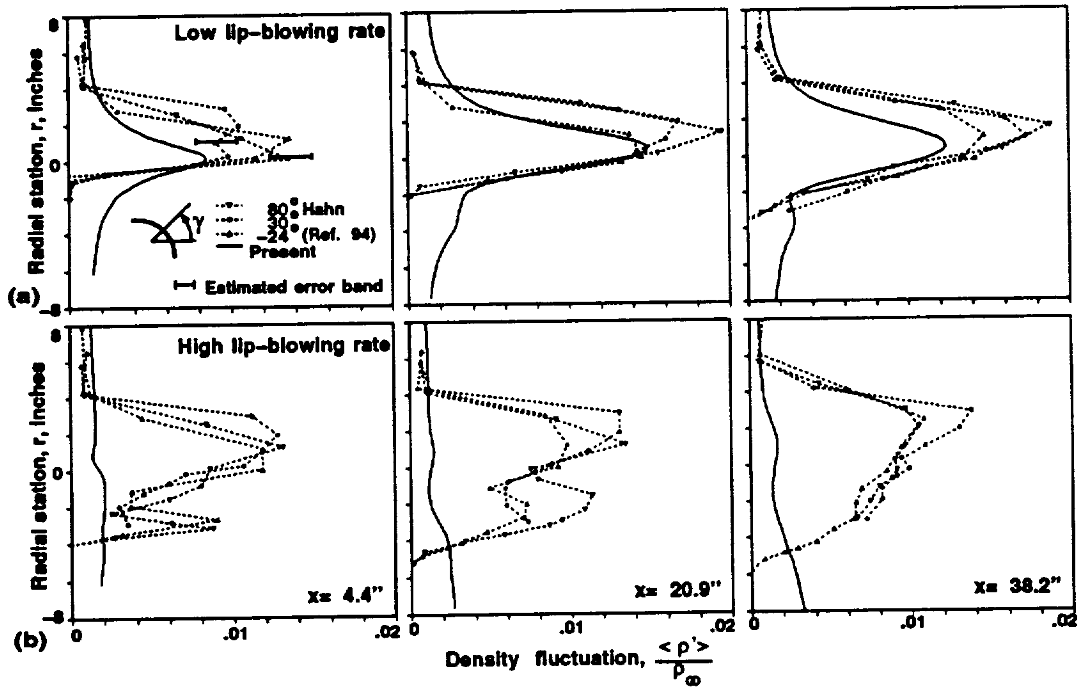

Figure 33: 2-d treated cavity: $\frac{<\rho'>}{\rho_\infty}$ profiles with (a) low and (b) high lip-blowing

Further investigation of the low-blowing rate case revealed the presence of large convecting structures associated with the shear layer. Figure 34 shows a contour plot of $\frac{\rho'}{\rho_\infty}$, depicting the growth and propagation of these sinuous motions in the shear layer. Also depicted in Fig. 34 is a schematic of the optical model, with the initial

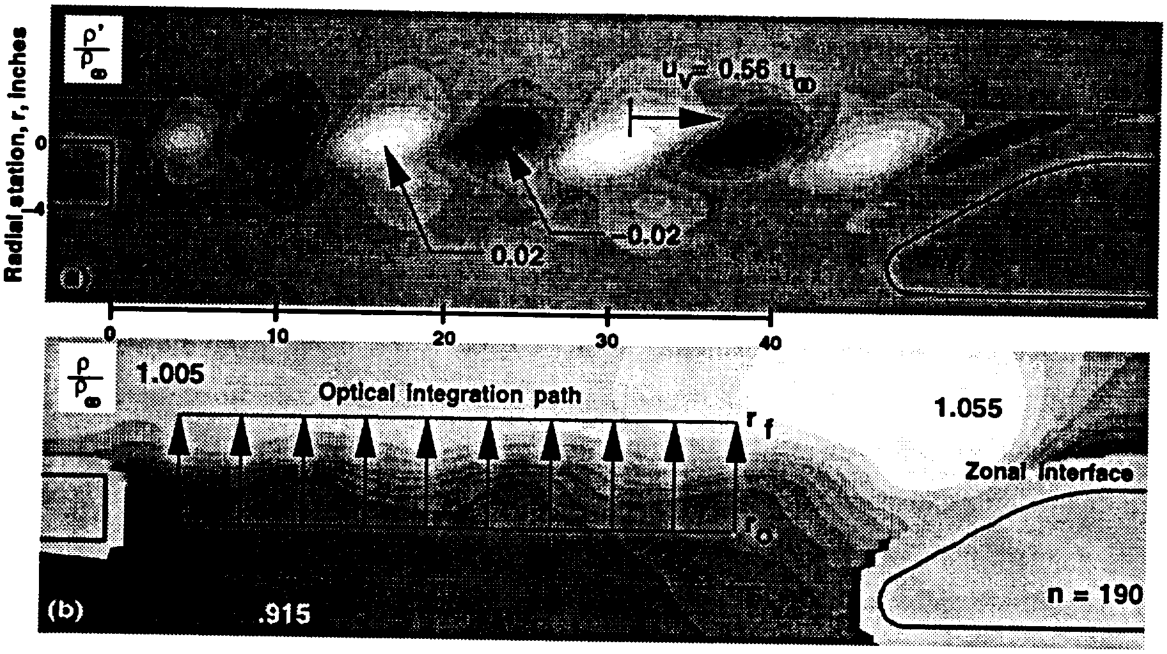

Figure 34: 2-d treated cavity, low lip-blowing rate: instantaneous contours of (a) $\frac{\rho'}{\rho_\infty}$ and (b) $\frac{\rho}{\rho_\infty}$ with schematic of optical model

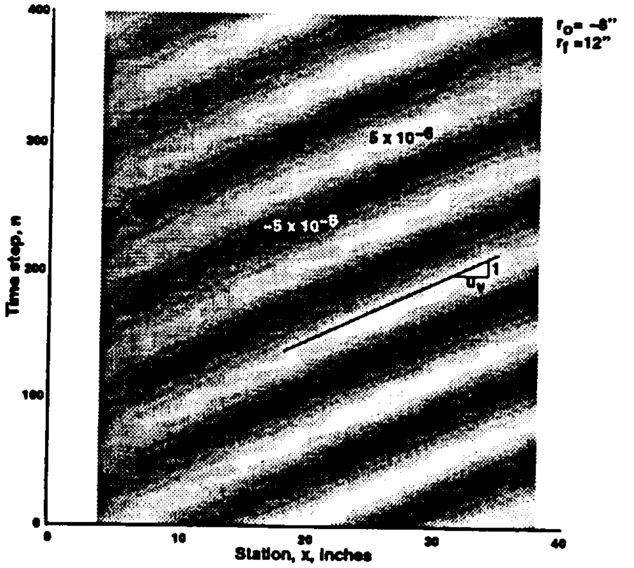

Figure 35: 2-d treated cavity: contours of $OPD'(x,t)$[ $in.$] along aperture, low lip-blowing rate

and final stations of the optical path integration are given by $r_0$ and $r_f$. The large structures, associated with a $0.03u_\infty$ vertical velocity component, are the primary contributors of the computed density fluctuations of the shear layer. The speed of the waves, as determined from Fig. 35, is $0.56u_\infty$, below the value of $0.66u_\infty$ inferred by Rossiter for rectangular cutouts, yet above the $0.51u_\infty$ determined analytically by Roscoe and Hankey [102].

Chew and Christiansen [50] and Tsai and Christiansen [51], utilizing results from computation and experiment, deduced that a free shear layer model of a sinusoidal phase delay growing in $x$ would produce results similar to those observed. Figure 35 displays behavior of a similar nature for the aero-window problem modelled here.

Comparisons of integrated aero-optical quantities, shown in Fig. 36, reveal slight overprediction for the low lip-blowing case and, given the $< \rho' >$ profiles, expected underprediction for the high lip-blowing rate case. Also shown in Fig. 36 are the root mean square of the optical path difference fluctuations for two additional integration paths. The result for the integration path which extends from $r_0 = -8''$ to $r_f = 12''$ displays an increment in $< OPD' >$ of about $(7 \times 10^{-7})''$ from the $7''$ path length case which originates at $r_0 = -3''$. The path initialized above the shear layer, from $r_0 = 4''$ to $r_f = 12''$, shows a small $< OPD' >$. Finally, the time averaged optical path difference, $\overline{OPD}$, can be seen to contribute curvature to the wavefronts as the light propagates through the shear layer. The optical clarity of the shear layer was determined using a $\beta = 2.584 \times 10^{-4}$, matching the value which was used to reduce the experimental data.

The analytic result for the $< OPD' >$, which goes like $x$, is found from [103]

$$\left(\frac{2\pi < OPD' >}{\lambda}\right)^2 = (\overline{\phi})^2 = 2k^2\frac{b^3}{a}L^3_{50n,m}\int_0^{L_{50n,m}}\left(\frac{\partial n}{\partial y}\right)^2 dy$$

Derivation of the model, which utilizes time-mean quantities to determine $< OPD' >$, is given by Bogdanoff [103]. This analytic result assumes an index-matched shear layer with a sinusoidal $n$ profile, $n(y) = \frac{n_1 - n_{max}}{2}\sin\left(\frac{2\pi y}{2L_{50n,m}}\right)$. The constants, $\frac{b^3}{a} = 0.0091$ and $L_{50n,m} \approx 1.31\delta_\omega = 1.31(0.18x[m])$, are empirical relations. The virtual origin of the shear layer is placed at $x = 0''$ for this analysis.

C-2

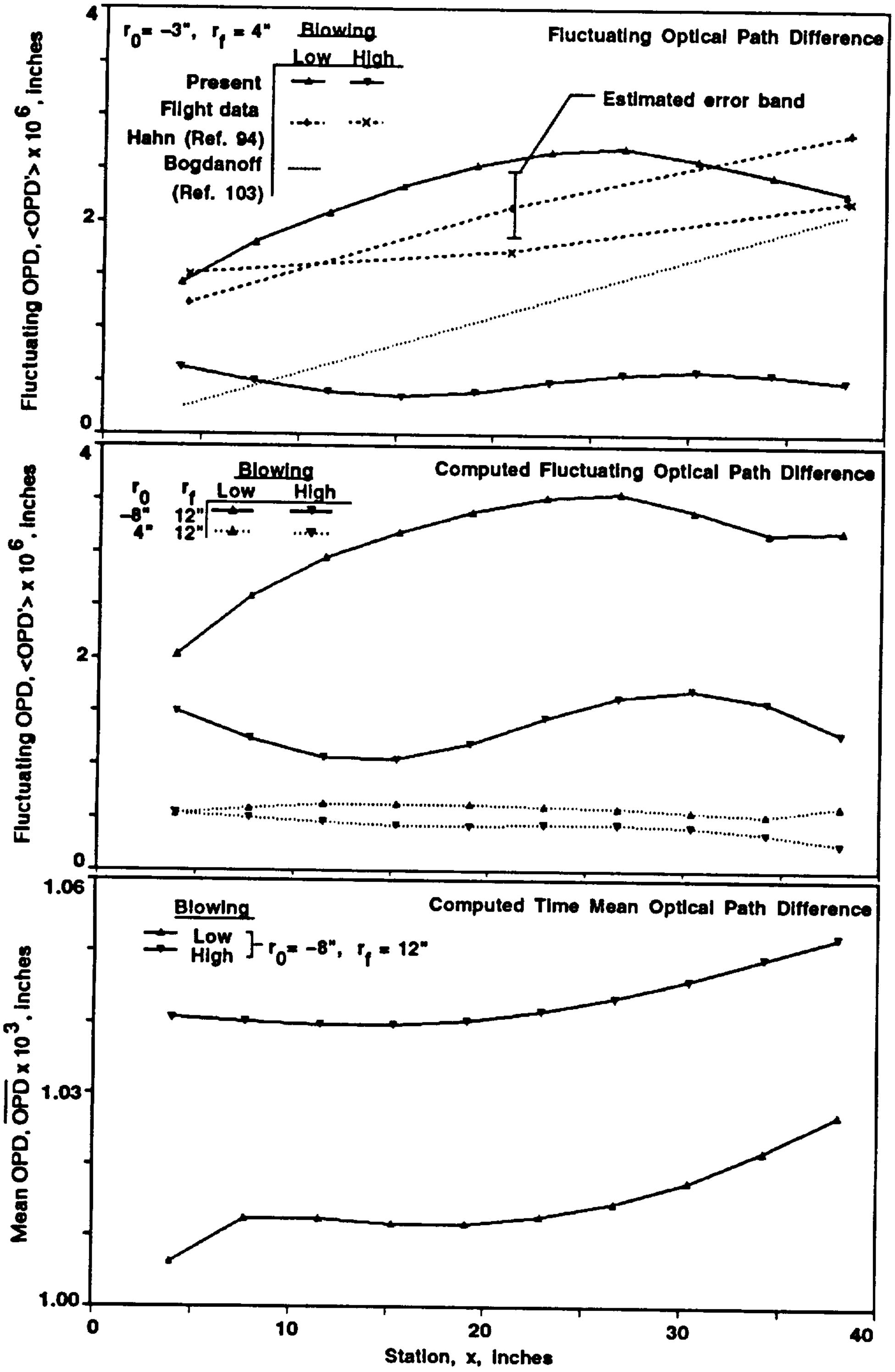

Figure 36: 2-d treated cavity: streamwise variation of optical path difference quantities

### Reduction of Experimental Data

The reduction of the data obtained from experiment [104] is noted here to delineate the approximations used and estimate systematic error bounds in the optical path distortion levels. Values of $\rho'$ are computed from assumptions of quasi-steady flow:

$$h_T = c_p T\left(1 + \frac{\gamma - 1}{2}M^2\right)$$

differentiation with respect to $t$

$$RT_T' = \frac{\rho p' - p\rho'}{\rho^2} + uu'\frac{\gamma - 1}{\gamma}$$

using $(\rho u)' = \rho u' + \rho' u$ then

$$\frac{T_T'}{T} = \frac{p'}{p} + (\gamma - 1)M^2\frac{(\rho u)'}{\rho u} - \left[(\gamma - 1)M^2 + 1\right]\frac{\rho'}{\rho}$$

The experimental observations against which the computed results are compared assume simultaneously small fluctuations in pressure and total temperature [105, 106], resulting in

$$\frac{\rho'}{\overline{\rho}} = \left(\frac{1}{(\gamma - 1)\overline{M}^2} + 1\right)^{-1}\frac{(\rho u)'}{\overline{\rho u}} \qquad (8)$$

Mean Mach number and density profiles are determined from isentropic relations, while $\frac{(\rho u)'}{\overline{\rho u}}$ is proportional to the voltage fluctuation, $\frac{E'}{E}$, obtained from hot film probes. The optical path disturbance is then found from [43]

$$(OPD')^2 = 2\left(\frac{\beta}{\rho_{STP}}\right)^2 \int_0^L < \rho' >^2 l_r dr \qquad (9)$$

where $\frac{l_r}{L}$ is the turbulent eddy size relative to the shear layer width, determined from cross correlation data to be typically about 15%.

The few available independent measurements [106, 107] indicate that pressure fluctuations of about 2% of freestream static pressure occur in the shear layer spanning the aperture of a quieted cavity geometry. In fact, Hahn [94] reported pressure fluctuations of 8% from shear layer rake measurements, however these include the dynamic pressure component normal to the orifice as well. Pressure fluctuation levels can also be inferred from sound pressure levels in the cavity, observed to be at least

130 dB for the AOA case. Shear layer total temperature fluctuations of about 1% have also been reported for this Mach regime [107]. The present low lip-blowing computation found a $< p' > \approx 1\%$ and a $< T_T' > \approx 0.8\%$ in the shear layer. The assumption of $< T_T' >$, $< p' > \approx 0$ in a shear layer is therefore questionable, and is used to estimate systematic experimental error bounds.

The determination of the error in $< \rho' >$ due to background noise levels begins by assuming the passage of a compression wave parallel to the static pressure port in the wake rake. Normal reflection of the wave would impart a larger deviation from $< \rho' >$ as computed by Eq. 8. Utilizing Görtler's free shear layer solution to provide $\overline{u(r)}$, assuming a cavity temperature recovery factor of unity, and holding mean static pressure constant through the layer, then $\overline{\rho(r)}$ is defined. The sensitivities of $\frac{\rho'}{\rho}$ to $\frac{p'}{p}$ and $\frac{T_T'}{T_T}$ are $\pm\frac{1}{(\gamma-1)M^2+1}$ and $\mp\frac{(1+(\gamma-1)M^2/2)}{(\gamma-1)M^2+1}$, respectively. Using a compression or rarefaction wave of strength $< p' >$ through the shear layer, then local values of $\rho'$ due to wave passage are defined. This value of $\rho'$ provides the error bound about the value obtained from Eq. 8, which assumes negligible $< p' >$ and $< T_T' >$. Taking shear layer pressure fluctuation levels corresponding to 135 dB and a velocity ratio $r = 0.1$, then the systematic error in the density fluctuations is 0.13% at the shear layer center. Figure 33 shows the resultant systematic error bars in $< \rho' >$.

From Eq. 9 the value of $< \rho' >$ is linearly proportional to $< OPD' >$. The error in $< OPD' >$ can be found by using a conservative within-system error of 0.05% in $\frac{<\rho'>}{\rho_\infty}$ gleaned from Fig. 33, plus the systematic error from the above analysis. The resultant error bar is plotted in Fig. 36.

### 5.2.5 Clean Configuration

The SOFIA configurations were initialized using the steady solution about a clean, or without cavity, geometry. In order to provide a measure of validation, the geometry and flow conditions were chosen to replicate the wind tunnel tests:

$$M_\infty = 0.85, \qquad Re_L = 4.2 \times 10^6, \qquad L = 12.6\ in.$$
$$\rho_\infty = 0.84\ kg/m^3, \quad p_\infty = 7.7 \times 10^4\ N/m^2, \quad \alpha = 2.5^\circ$$

However, subsequent correction of the wind tunnel data has resulted in the $Re_L = 4.0 \times 10^6$, about 5% lower than above. The temperature difference from this correction causes the sound speed in these computations to be approximately 6% higher than experiment. Numerical results obtained for this 7% scale model are discussed below.

The wind tunnel model without cavity was simulated in order to assess angle of attack errors owing to wind tunnel wall effects. Figure 37 compares the present pressure coefficient profiles along the crest, side, and bottom of the model with flight data [108] and wind tunnel results [16]. Experimental results are shown for both untripped and tripped cases; the latter case was used for all subsequent wind tunnel testing. The computations specified turbulent walls at all no-slip boundaries. Although this comparison indicates that the influence of the tunnel wall was small near the cavity, pressures along the bottom of the model are shifted, possibly due to the effect of the lower wall. A four-order drop in magnitude of $\delta\rho|_{max}$ was attained for this steady case in 2000 steps, using approximately four Cray Y-MP CPU hours.

### 5.2.6 Configuration 25

The geometry shown in Fig. 38 was the initial cavity configuration tested in the wind tunnel. This simulation was implemented in order to demonstrate the capture of self-excited cavity resonance in three dimensions. The flow conditions were the same as used above, the flowfield was initialized from the steady clean case. The stability-limited time step used was $\Delta t = 3.53\mu s$. This interval size corresponds to a $CFL \approx 1$ in the streamwise direction within the shear layer, and a $CFL|_{max} \approx 500$.

Instantaneous Mach number contours in Fig. 39 show the flapping of the shear layer and interpolation treatment. Sample pressure histories on the cavity walls and a comparison of the $PSD$ resulting from the wind tunnel and numerical efforts are shown in Fig. 40. The $PSD$ was obtained using 2048 points, a Hanning window, and no zero-padding. The predicted frequencies of the dominant tones appear reasonable, and the computed dominant tone is within 3 dB of experiment. The magnitudes of the computed higher modes are much lower than observed experimentally.

Estimation of the grid resolution required to maintain a propagating wave of a specific magnitude can be deduced from the rectangular two-dimensional cavity and

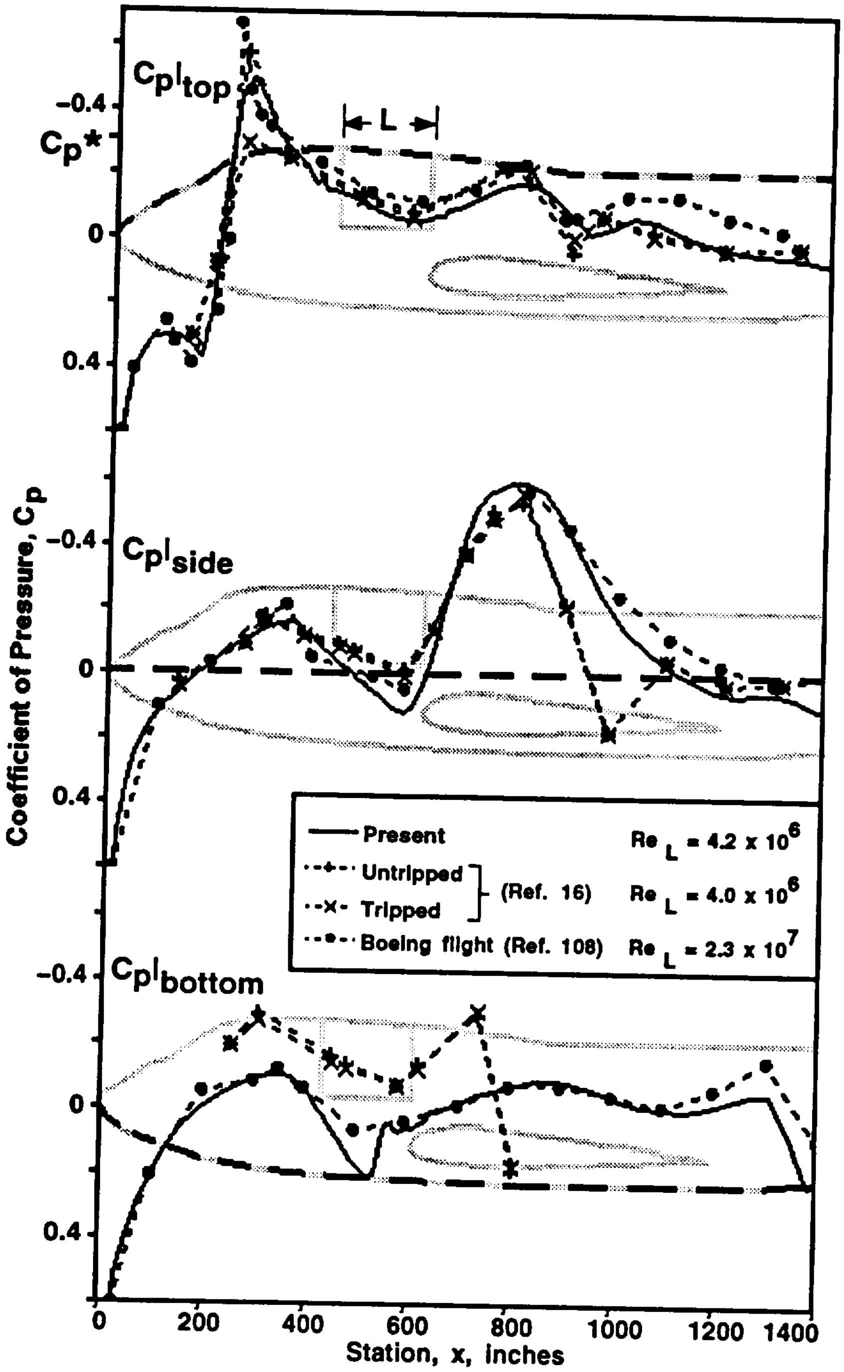

Figure 37: Clean configuration: pressure coefficient comparison

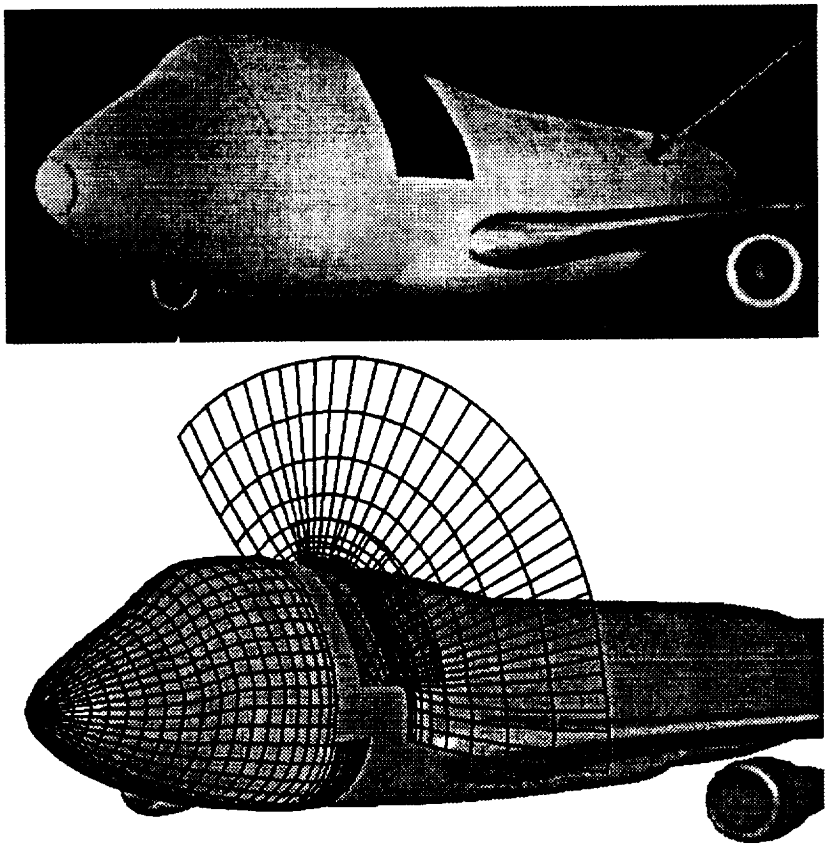

Figure 38: Configuration 25: wind tunnel and numerical models

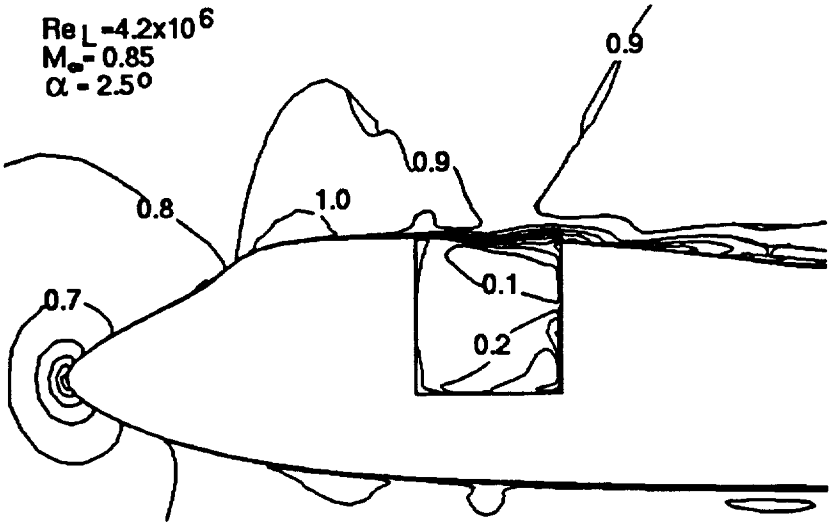

Figure 39: Configuration 25: Mach number contours at y=0

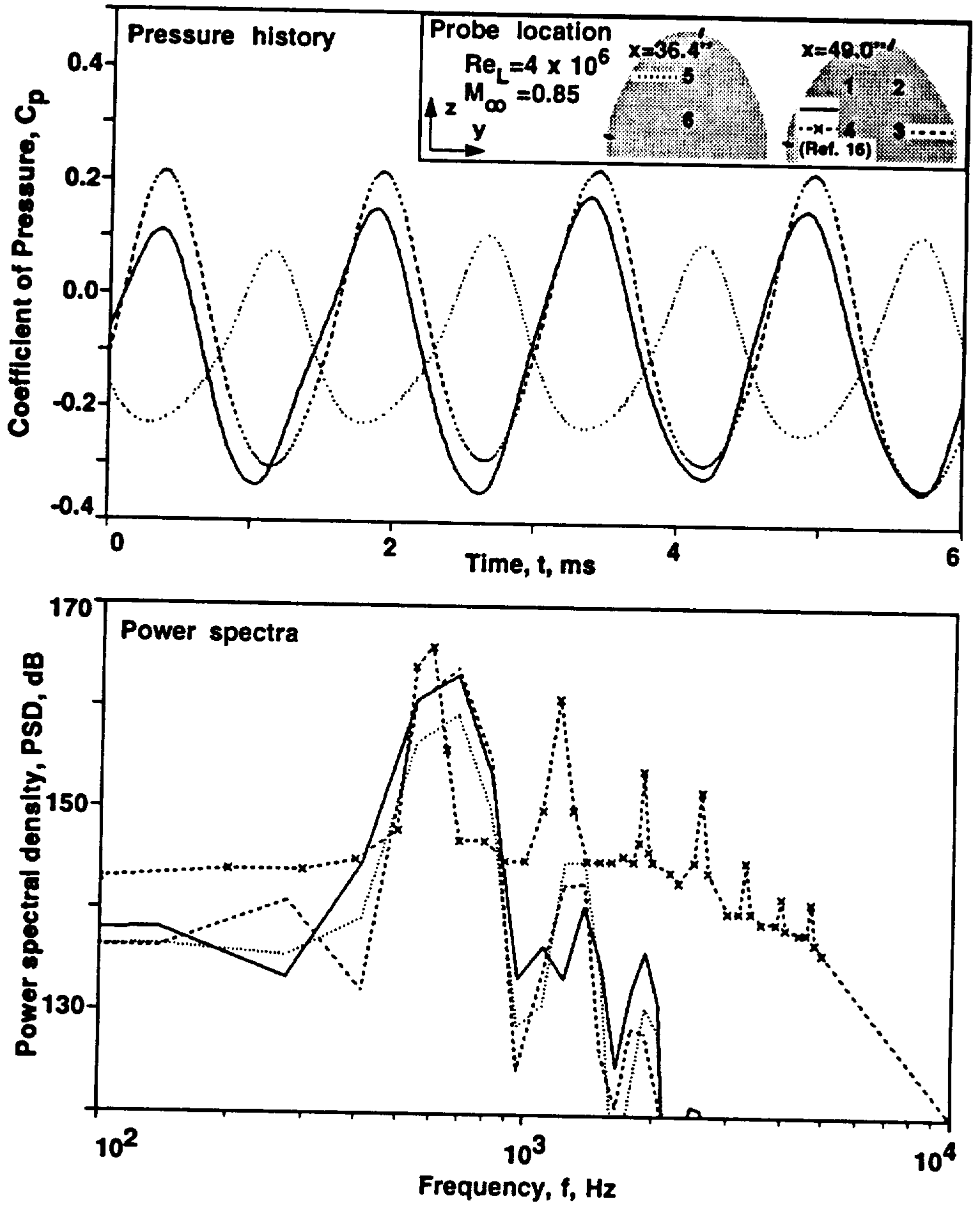

Figure 40: Configuration 25: pressure histories and power spectra

configuration 25 results. First, wavelength can be estimated by assuming the wave to be harmonic at a given frequency and travelling at the local speed of sound. Next, it is noted that frequencies around 2 kHz were resolved well in the two-dimensional case, in which the grid resolution was such that about 40 points supported the wave. From the configuration 25 results, it is seen that only the 700 Hz peak is well resolved, which again gives approximately 40 points across the wave for this coarser grid. Although numerical damping of the higher frequencies can be expected, most of the energy is contained in the lowest frequency mode, as can be seen in the sound pressure level,

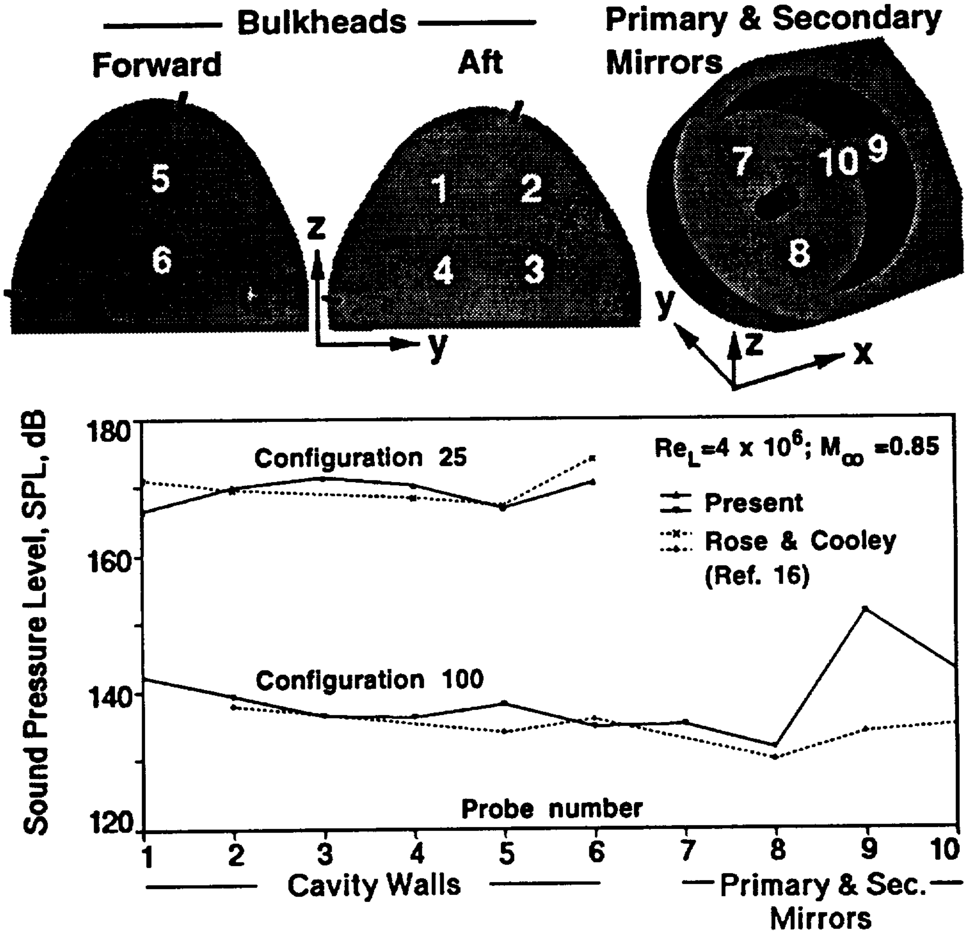

Figure 41: Comparison of sound pressure levels

or $SPL$, comparison of Fig. 41 where

$$SPL\ [dB] = 20 \log_{10} \frac{< p' >\ [N/m^2]}{2 \times 10^{-5}}$$

Experimentally observed and computed levels of $< p' >$ in the time domain were used in Fig. 41. The $SPL$ for the resonating and quieted geometries obtained numerically are in reasonable agreement with experiment.

### 5.2.7 Configuration 100

In 1990, an investigation of SOFIA cavity quieting treatments was performed in the NASA Ames $14' \times 14'$ wind tunnel [16]. Of the many geometries tested, configuration 100 resulted in the lowest sound production levels. This simulation was implemented in order to determine if the same level of quieting could be predicted numerically as was observed experimentally. As commented on earlier, previous investigations [41] of cavity noise suppression have shown aft ramp treatments to be effective by allowing a stable shear layer reattachment site. For the SOFIA experiment, this type of geometry treatment was found to be quieter than the untreated configuration 25 case by over 30 dB. Figure 41 summarizes that the proper trends were computed. The flow conditions were again initialized from the clean case, and integrated using a stability-limited time step size of $\Delta t = 7.06 \mu s$. The frequency domain analysis was obtained using 4096 points, a Hanning window, and no zero-padding.

For reference purposes, Fig. 42 shows the position and orientation of the telescope assembly in the aircraft and the associated coarsened grids. Figure 43 shows the topology used in the cavity region, where the grids have again been coarsened for clarity. The choice of topology, driven by grid quality and turbulence modelling considerations, is similar to those used in the two-dimensional studies.

Quantitative comparisons were made for this passively quieted cavity geometry in terms of shear layer profiles and pressure spectra in the cavity. Since errors in shear layer mass entrainment rate would adversely affect the cavity velocity field and hence the mean telescope loads, an important validation parameter is the shear layer spread rate. Figure 44 depicts mean experimental and computational shear layer Mach number profiles. The vertical scale of the profiles is twice that shown in the contour

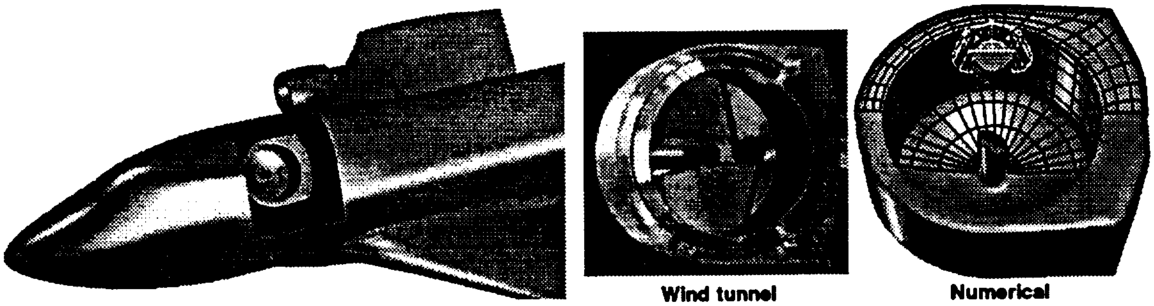

Wind tunnel

Numerical

Figure 42: Telescope location and grids

plot for clarity. Note that the experimental profiles were obtained using a rake, which is sensitive only to $u$, the x-component of velocity. The discrepancy between $|u|/c$ and $|\mathbf{V}|/c$ was found to be approximately 0.05 at the lower tail of the profile. Figure 44 indicates reasonable agreement for growth rates, though the profile shapes become somewhat different as the shear layer approaches the ramp. This discrepancy may be in part due to probe position uncertainty and geometry modifications to allow for the probe mechanism. These modifications included removal of the telescope assembly and cutting a streamwise slot in the ramp. The difference in spread rates may also be due to specification of an overly-large value of $\sigma_0$. Time averaging of velocities was performed over 1000 time steps and the profiles were insensitive to the duration of the time-segment used.

Some measure of qualitative agreement may be gleaned from the instantaneous streamlines depicted in Fig. 45, which show a strong cross flow component at the aft ramp for this aperture elevation angle. Although oil flow visualization was not performed on the configuration 100 experimental runs, a similar aft molding shown in Fig. 46 also displays strong cross flow behavior.

Assessment of the oscillating telescope assembly loads requires the accurate resolution of the unsteady pressure field in the cavity. Comparison of the computed and observed spectra at specific locations provides a measure of confidence for the computed telescope loads. Toward the estimation of loads, Fig. 47 shows the pressure history and resultant $PSD$ on the cavity walls. Although the peak levels are in

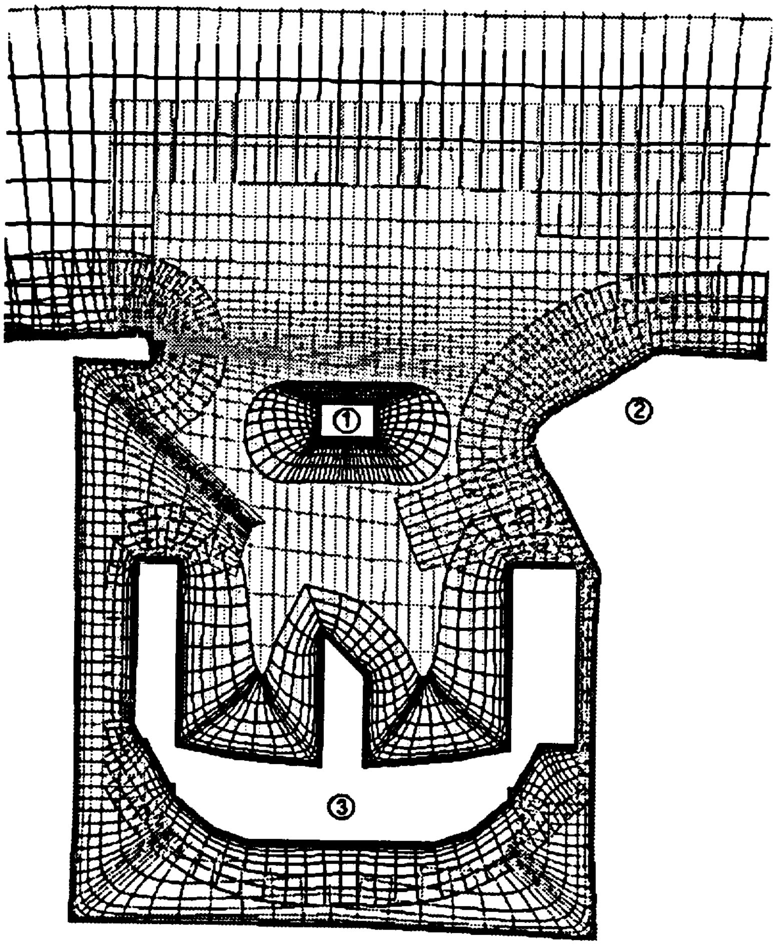

**①** **Secondary Mirror**
**②** **Aft Ramp**
**③** **Primary and Tertiary Mirror Assembly**

Figure 43: Configuration 100: cavity region topology

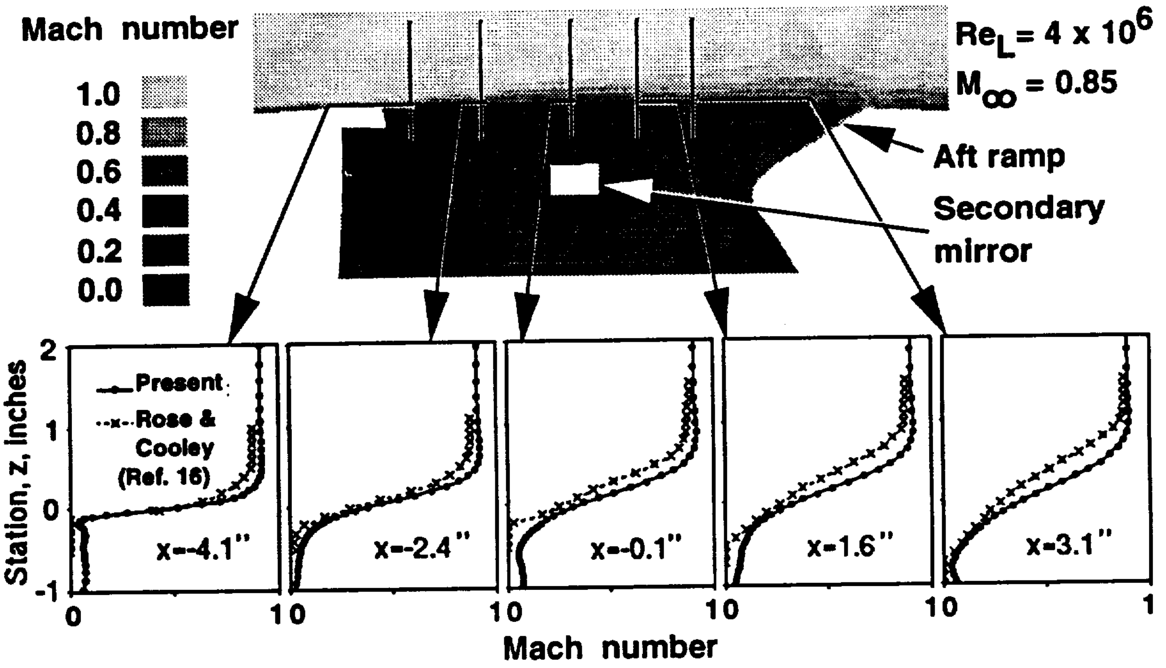

Figure 44: Configuration 100: instantaneous Mach number contours and mean profiles

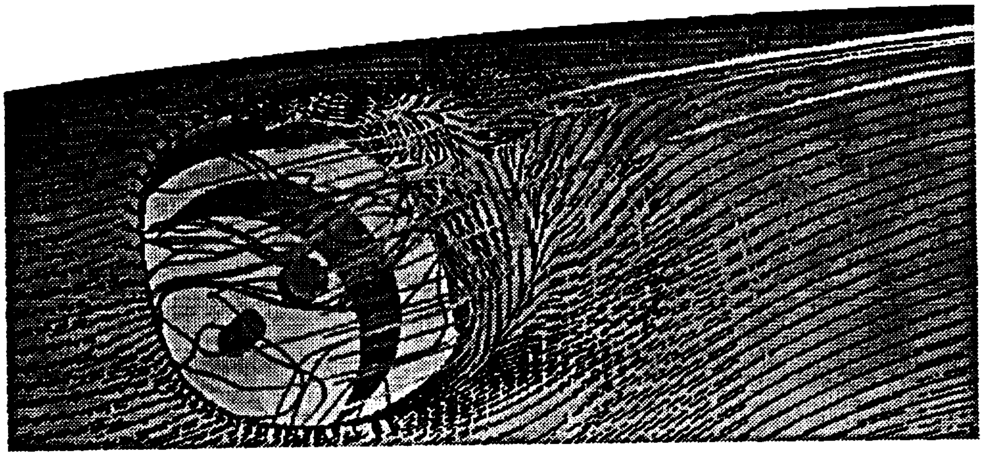

Figure 45: Configuration 100: streamlines along the treated aperture

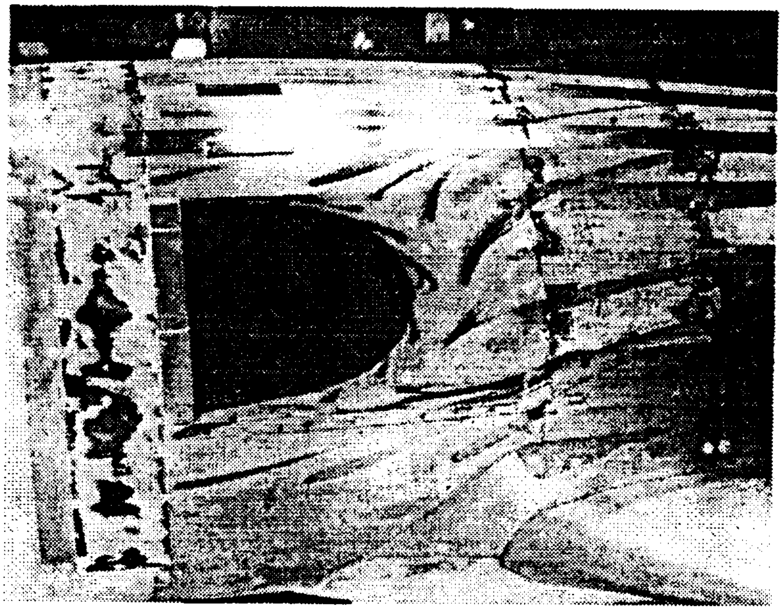

Figure 46: Experimentally [16] observed surface flow pattern

agreement, the computed spectra can again be seen to drop more rapidly with frequency than the experimental results. The pressures on the primary mirror, shown in Fig. 48, show lower high frequency content with the magnitude of the peak at 1800 Hz not well resolved. Figure 49 shows a low frequency component at the downstream secondary mirror location which was not found experimentally. The discrepancy is manifested as the difference between the computed and measured $SPL$ seen in Fig. 41 at probe 9.

### Scaling to Flight

The above computations were performed at wind tunnel geometric scale in order to allow close comparison with the SOFIA experiments. An early misunderstanding resulted in a mismatch of the ambient conditions between the wind tunnel tests and the computations. Scaling of optical effects as well as the acoustic frequencies and magnitudes from tunnel and computation to flight are obviously of design interest, and hence are noted here for completeness and clarity.

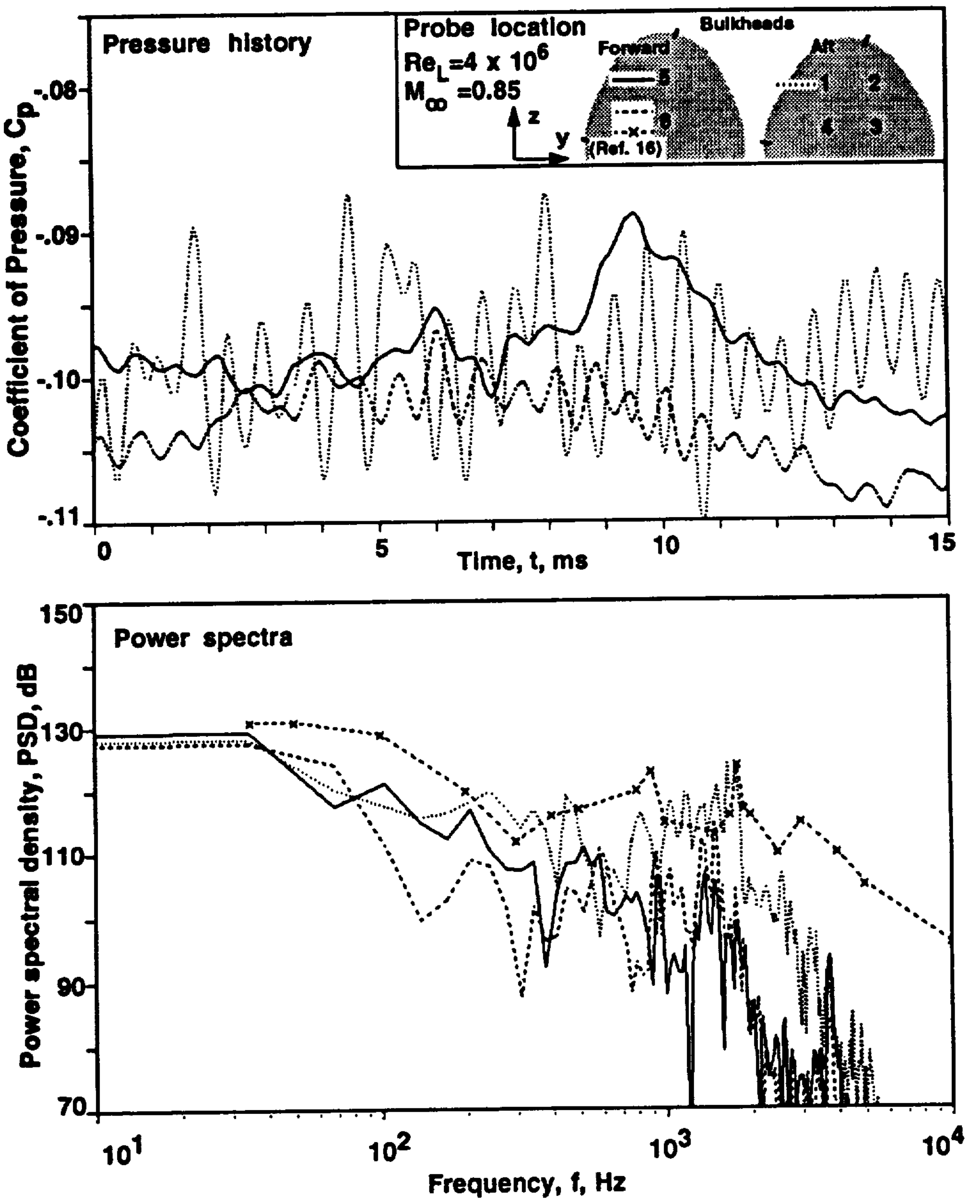

Figure 47: Configuration 100: pressure history and power spectra on cavity wall

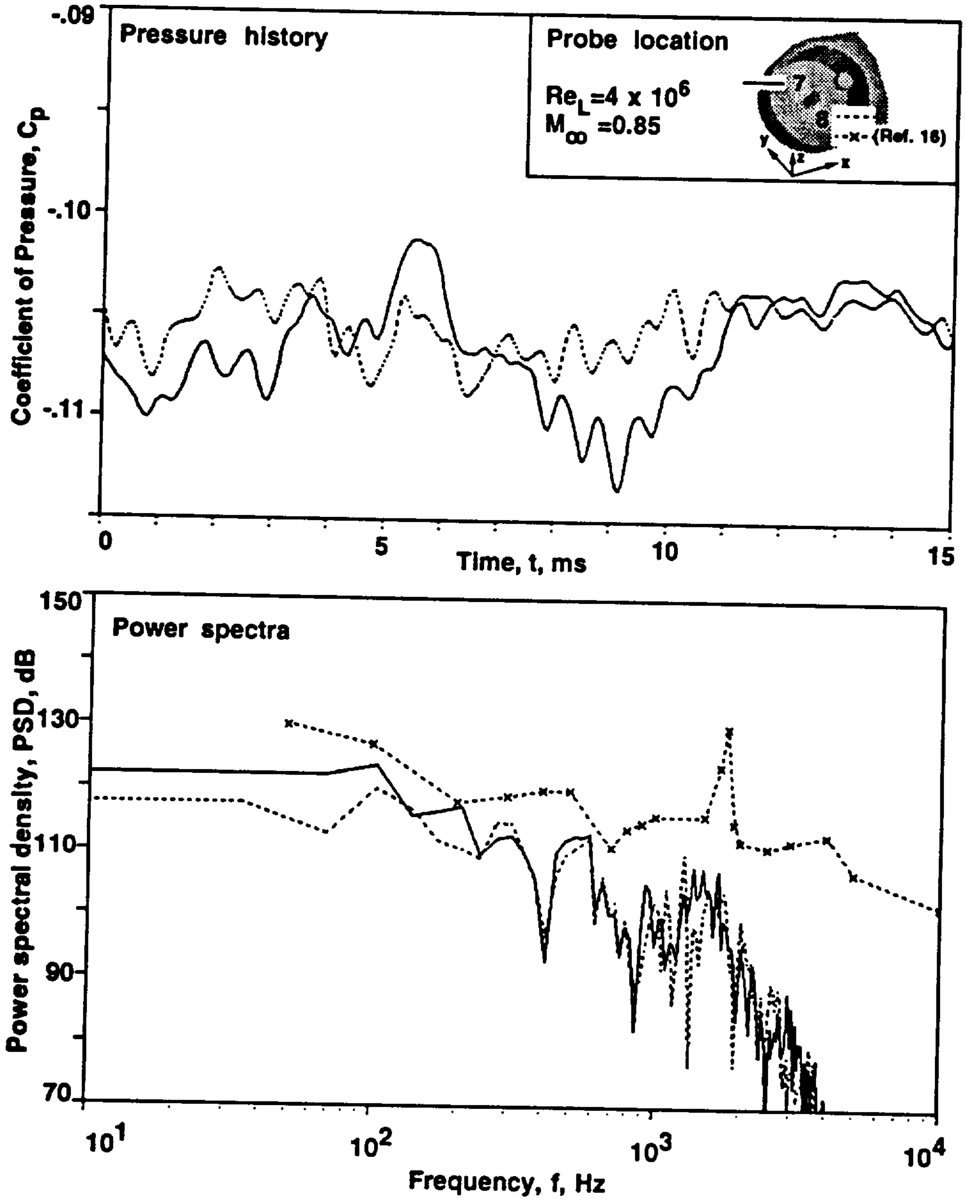

Figure 48: Configuration 100: pressure history and power spectra on primary mirror

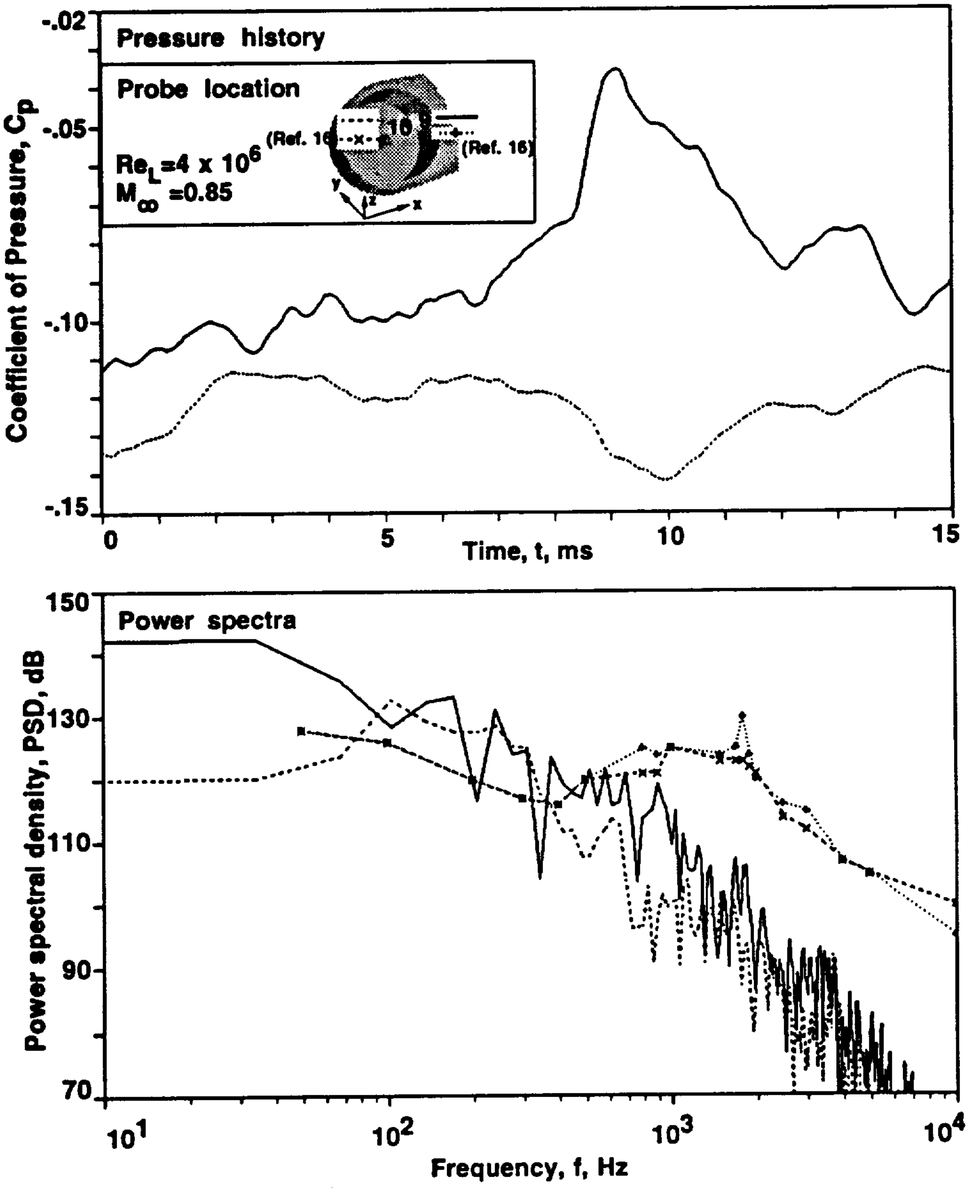

Figure 49: Configuration 100: pressure history and power spectra on secondary mirror

Briefly, the frequency is a function of the cavity length and the recovery temperature, which affects the acoustic speed in the cavity. The magnitude of the acoustic oscillations scale with dynamic pressure, while the optical distortion is proportional to density and geometric scale. Model and flight conditions are summarized in Table 2. Scaling from wind tunnel to flight results in a decrease in frequency by a multiplication factor of 16.4, a reduction of the magnitude of pressure oscillations by a factor of 11 dB, and an increase in optical distortion by 5.4 times. In contrast, scaling from computation to flight results in a frequency reduction of 17.4 times, a decrease in fluctuating pressure magnitude of 13 dB, and an increase in optical distortion of 4.9 times. Generally, the levels of uncertainty in measured quantities is greater than the difference between computed and wind tunnel results.

| | | Magnitude | | |
|---|---|---|---|---|
| Quantity | Units | Wind tunnel | Computation | Flight |
| $M_\infty$ | – | 0.85 | 0.85 | 0.85 |
| $Re_L$ | – | $4 \times 10^6$ | $4.2 \times 10^6$ | $2.3 \times 10^7$ |
| $T_\infty$ | °$K$ | 286 | 322 | 217 |
| $\rho_\infty$ | $\frac{kg}{m^3}$ | 0.77 | 0.84 | 0.289 |
| $L$ | $m$ | 0.32 | 0.32 | 4.6 |

Table 2: Wind tunnel, computed, and flight conditions

### 5.2.8 Configuration 100: Aero-Optical Effects

The optics code was applied to the computed density field obtained for configuration 100 from $t = 0$ to $7.8\ ms$ in the manner depicted in Fig. 50. Ten rays were propagated through 110 instantaneous density fields in time intervals of $\Delta t = 70.6 \mu s$. Using the elapsed time for a shear layer structure to convect across the aperture as a characteristic time, $T_c = \frac{L}{K u_\infty}$, then the optical measurement was taken for about five $T_c$. The results presented here are for a computational plane at approximately the cross flow center of the aperture, partly shown in Fig. 50, which will provide only a

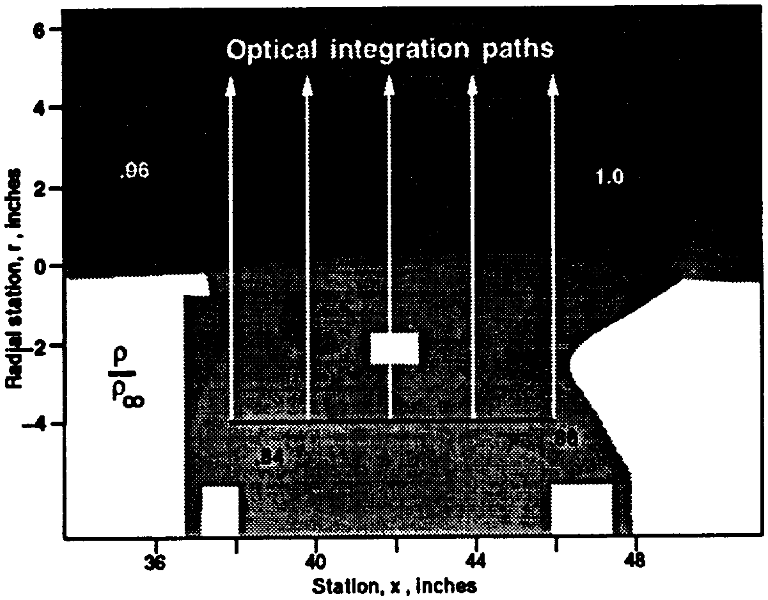

Figure 50: Configuration 100: instantaneous density field and optical refraction model

streamwise variation in optical properties. The numerical results are presented compared to previous analysis [103] and experiment [16] in which shear layer aerodynamic measurements were used to infer distortion.

The levels of fluctuating density were severely underpredicted as compared to experiment, as can be seen in Fig. 51. Although peaks in the density fluctuations were computed, the highly-ordered shear layer structures similar to those found in the AOA study were not observed. Differences may be attributable to grid coarseness or within-system errors in measurements, most likely the former.

The optical wavefront distortion through the configuration 100 aero-window is summarized in Fig. 52. The uppermost plot of Fig. 52 shows that the distortion model applied through the shear layer alone underpredicts the data determined analytically and experimentally. However, the computed trend is generally consistent with the data. At the streamwise center of the aperture, the $< OPD' >$ at two additional spanwise locations are shown. These points provide an estimate of the crossflow variation in distortion levels.

The center plot of Fig. 52 depicts computed $< OPD' >$ for ray propagation originating below the secondary mirror, $r_0 = -3.7''$, and above the shear layer, $r_0 =$

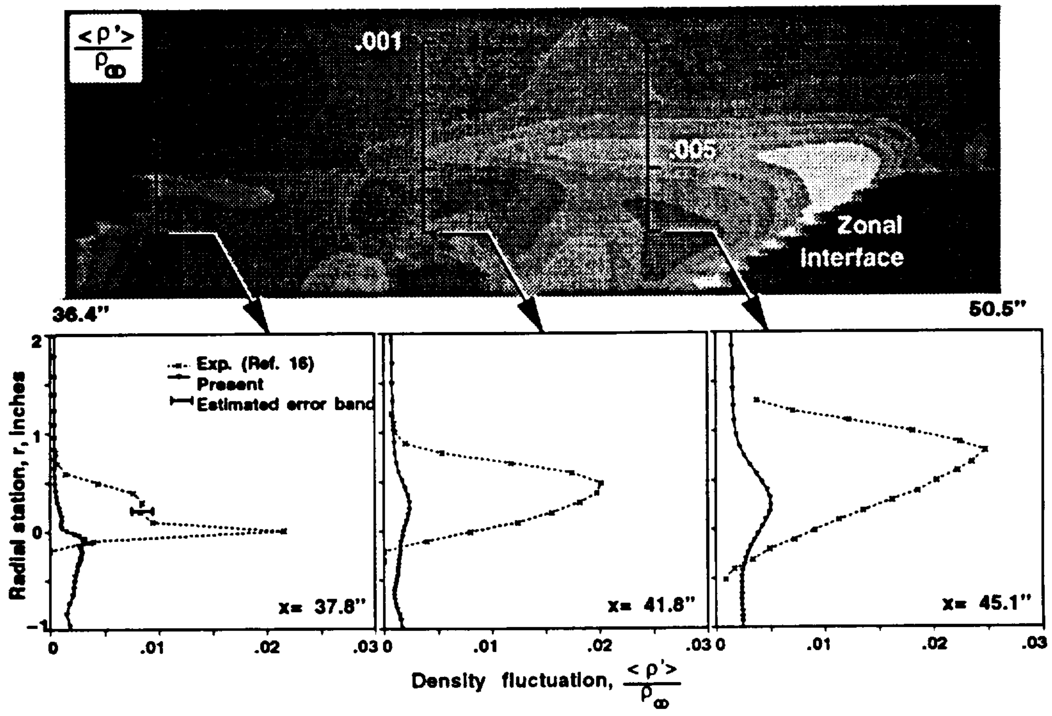

Figure 51: Configuration 100: density fluctuation at crossflow center of aperture

2.3″. Comparison of the computed results show an increment in $< OPD' >$ below the secondary mirror. This distortion increment appears to be caused by a jet of re-entrant fluid originating from the shear layer impingement upon the aft ramp. Finally, the last plot of Fig. 52 shows that curvature is imparted to the mean optical field. The dip in the fluctuating and mean $OPD$ levels at $x = 42''$ is caused by the presence of the secondary mirror, in which the index of refraction, $n$, was fixed at unity.

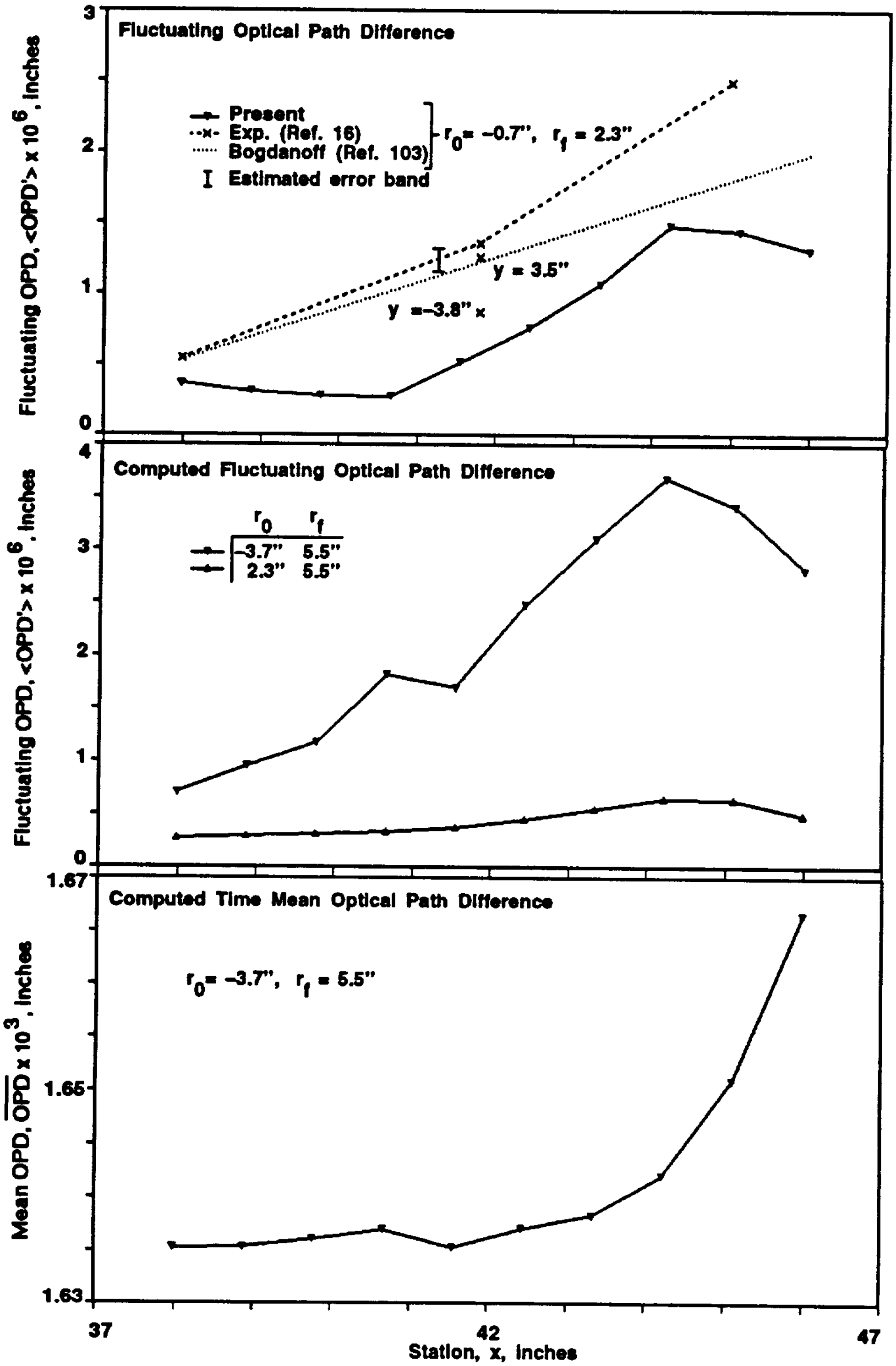

Figure 52: Configuration 100: comparison of wavefront distortion

# Chapter 6

# Conclusions

The objective of this effort was to develop and assess computational methods as applied to unsteady perfect gas flows. The developed technology was demonstrated through application to two classes of problems in which unsteady effects play a dominant role.

### 6.1.1 Blast-Wave Problem

The application of two upwind schemes to unsteady, multidimensional problems within a structured finite-volume framework has been demonstrated on the viscous three-dimensional blast-wave problem. The use of time-conservative differencing and an approximate Riemann solver coupled with total variation diminishing methods has resulted in time accurate nonoscillatory flowfield resolution. Newton subiterations are utilized to reduce the numerical approximations made, such as factorization error and the inclusion of only the first-order terms in the formation of the inviscid Jacobian. In addition, analysis and application of two flux evaluation methods produced only small differences. Finally, for the blast-wave/target interaction problem the effect of viscosity was increasingly significant at later times.

Further efforts to increase the accuracy and efficiency of these methods may be directed along the use of nonfactored schemes or implementation on parallel machines. Geometries of realistic complexity will require a zonal approach, necessarily conservative because of the strongly unsteady compressible flow regimes considered here. Efficient adaptive grid techniques will reduce the memory and time expense. Synthesis of dynamical, structural, and fluid flow effects may provide the capability for an interdisciplinary simulation of the physical processes involved in this class of problems.

### 6.1.2 Cavity Flow Problem

The work presented here is the initial effort towards development of a cavity flow design and analysis tool, specifically tailored for use throughout the SOFIA project life. Thus far, this investigation has demonstrated that self-induced cavity resonance can be accurately captured for complex geometries modelled using an overset mesh topology. Shear layer profiles and resonant behavior are consistent with previous analytic and experimental work. Generally, sound pressure levels agree to within 4%. Topology treatment has allowed the simple specification of turbulent wall and shear layer regions as well as providing a means of isolating the unsteady flow region.

Improvements in the energy distribution in frequency may be attained by use of higher-order spatial approximations or more simply by grid refinement. The use of higher order turbulence models should also be investigated.

### 6.1.3 Aero-Optical Effort

Comparison of computed and experimentally observed optical distortion levels showed similar trends, albeit with a discrepancy in magnitude. Large structures in the shear layer of the two-dimensional quieted cavity resulted in a 25% overprediction of wavefront distortion. The three-dimensional results underpredicted phase distortion by approximately 50% as compared to experiment.

Further investigation is required to determine if improved wavefront distortion results can be achieved. Quantification of the effects of shear layer flow resolution on the optical field is certainly warranted. Improvements in the optical modelling could include an empirical model to account for scattering owing to subgrid turbulent scales.

### 6.1.4 Future Directions

The development of these types of tools partially fulfills the objective of augmentation of experimental test programs, possibly eliminating the need to test certain specific configurations altogether. The use of the unsteady flowfield information appears feasible for analysis of the blast-wave/target interaction and cavity flow problem classes. However, current limits in computational speed prevent rapid solution throughput. Thus, the goal of nesting full unsteady Navier-Stokes methods within the design cycle awaits the advent of computers of increased power.

# Bibliography

[1] Opalka, K.O., "Large Blast and Thermal Simulator Advanced Concept Driver Design by Computational Fluid Dynamics," BRL-TR-3026, Aug. 1989.

[2] Kutler, P., Sakell, L., and Aiello, G., "Two-Dimensional Shock-on-Shock Interaction Problem," *AIAA J.,* Mar. 1975, pp. 361-367.

[3] MacCormack, R.W., "The Effect of Viscosity in Hypervelocity Impact Cratering," AIAA-69-354, 1969.

[4] Kutler, P. and Sakell, L., "Three-Dimensional, Shock-on-Shock Interaction Problem," *AIAA J.,* Oct. 1975, pp. 1360-1367.

[5] Kutler, P. and Shankar, V., "Diffraction of a Shock Wave by a Compression Corner: I. Regular Reflection," *AIAA J.,* Feb. 1977, pp. 197-203.

[6] Champney, J.M., Chaussee, D.S., and Kutler, P., "Computation of Blast Wave - Obstacle Interactions," AIAA-82-0227, Jan. 1982.

[7] Beam, R.H. and Warming, R.F., "An Implicit Factored Scheme for the Compressible Navier-Stokes Equations," *AIAA J.,* Vol. 16, Apr. 1978, pp. 393-402.

[8] Mark, A. and Kutler, P., "Computation of Shock Wave/Target Interaction," AIAA-83-0039, Jan. 1983.

[9] Yee, H.C., "Upwind and Symmetric Shock-Capturing Schemes," NASA TM-89464, May 1987.

[10] Hisley, D. and Molvik, G.A., "Axisymmetric Calculations for the Large Blast/Thermal Simulator (LB/TS) Shock Tube Configuration," BRL-TR-2935, Sep. 1988.

[11] Löhner, R., "The Efficient Simulation of Strongly Unsteady Flows by the Finite Element Method," AIAA-87-0555, Jan. 1987.

[12] Bennett, B.C., Abbett, M.J., and Wolf, C.J., "Viscous Effects of Blast Wave Flowfields," AIAA-86-0031, Jan. 1986.

[13] Baldwin, B.S. and Lomax, H., "Thin-Layer Approximation and Algebraic Model for Separated Turbulent Flows," AIAA-78-257, Jan. 1978.

[14] Molvik, G.A., "Computation of Viscous Blast Wave Solutions with an Upwind Finite Volume Method," AIAA-87-1290, June 1987.

[15] Rossiter, J. E., "Wind-Tunnel Experiments on the Flow Over Rectangular Cavities at Subsonic and Transonic Speeds," Royal Aircraft Establishment Reports and Memoranda No. 3438, Oct. 1964.

[16] Rose, W.C. and Cooley, J.M., "SOFIA Wind Tunnel Data Analysis and Implications for the Full-Scale Aircraft," Rose Eng. and Research, Inc., Dec. 1990.

[17] Karamcheti, K., "Acoustic Radiation from Two-Dimensional Rectangular Cutouts in Aerodynamic Surfaces," NACA TN-3487, 1955.

[18] Roshko, A., "Some Measurements of Flow in a Rectangular Cutout," NACA TN-3488, 1955.

[19] Plumblee, H.E., Gibson, J.S., and Lassiter, L.W., "A Theoretical and Experimental Investigation of the Acoustic Response of Cavities in an Aerodynamic Flow," TR WADD-61-75, Wright-Patterson Air Force Base, 1962.

[20] Maull, D.J. and East, L.F., "Three-dimensional flow in cavities," *J. Fluid Mech.,* Vol. 16, Part 4, 1963. pp. 620-632.

[21] East, L.F., "Aerodynamically Induced Resonance in Rectangular Cavities," *J. Sound Vib.,* 1966(3), pp. 277-287.

[22] Heller, H.H., Holmes, D.G., and Covert, E.E., "Flow-Induced Pressure Oscillations in Shallow Cavities," *J. Sound Vib.,* 1971(18), pp. 545-553.

[23] Bilanin, A. J. and Covert, E. E., "Estimation of Possible Excitation Frequencies for Shallow Rectangular Cavities," AIAA J., Vol. 11, No. 3, Mar. 1973, pp. 347-351

[24] Heller, H.H. and Bliss, D.B., "Aerodynamically Induced Pressure Oscillations in Cavities - Physical Mechanisms and Suppression Concepts," AFFDL-TR-74-133, Feb. 1975.

[25] Yu, Y. H., "Measurements of Sound Radiation from Cavities at Subsonic Speeds," AIAA-76-529, July 1976.

[26] Tam, C. K. W. and Block, P. J. W., "On the Tones and Pressure Oscillations Induced by Flow Over Rectangular Cavities," *J. Fluid Mech.,* Vol. 89, Part 2, 1978, pp. 373-399.

[27] Kaufman, L.G. and Clark, R.L., "Mach 0.6 to 3.0 Flows Over Rectangular Cavities," Report AFWAL-TR-82-3112, Wright-Patterson Air Force Base, 1983.

[28] Erickson, D.D. and Durgin, W.W., "Tone Generation by Flow Past Deep Wall Cavities," AIAA-87-0167, Jan. 1987.

[29] Neary, M.D., "Time Dependent Self-Sustaining Oscillations of Cavity Flow," AIAA-87-0142, Jan. 1987.

[30] Hankey, W.L. and Shang, J.S., "Analysis of Pressure Oscillations in an Open Cavity," *AIAA J.,* Vol. 18, Aug. 1980, pp. 892-898.

[31] Venkatapathy, E., Lombard, C.K., and Nagaraj, N., "Numerical Simulation of Compressible Flow Around Complex Two-Dimensional Cavities," AIAA-87-0116, Jan. 1987.

[32] Baysal, O. and Stallings Jr., R.L., "Computational and Experimental Investigation of Cavity Flowfields," AIAA-87-0114, Jan. 1987.

[33] Gorski, J.J., Ota, D.K., and Chakravarthy, S.R., "Calculation of Three Dimensional Cavity Flowfields," AIAA-87-0117, Jan. 1987.

[34] Suhs, N.E., "Computations of Three-Dimensional Cavity Flow at Subsonic and Supersonic Mach Numbers," AIAA-87-1208, June 1987.

[35] Baysal, O. and Srinivasan, S., "Unsteady Viscous Calculations of Supersonic Flows Past Deep and Shallow Three-Dimensional Cavities," AIAA-88-0101, Jan. 1988.

[36] Rizzetta, D. P., "Numerical Simulation of Supersonic Flow Over a Three-Dimensional Cavity," *AIAA J.*, Vol. 26, July 1988, pp. 799-807.

[37] Om, D., "Navier-Stokes Simulation for Flow Past an Open Cavity," *AIAA J. of Aircraft*, Vol. 25, Sep. 1988, pp. 842-848.

[38] Baysal, O. and Yen, G.W., "Implicit and Explicit Computations of Flows Past Cavities With and Without Yaw," AIAA-90-0049, Jan. 1990.

[39] Dougherty, N.S., Holt, J.B., Nesman, T.E., and Farr, R.A., "Time-Accurate Navier-Stokes Computations of Self-Excited Two-Dimensional Unsteady Cavity Flows," AIAA-90-0691, Jan. 1990.

[40] Löhner, R., "Three-Dimensional Fluid-Structure Interaction Using a Finite Element Solver and Adaptive Remeshing," *Computing Systems in Eng.*, 1, Nos. 2-4, 1990, pp. 257-272.

[41] Komerath, N.M., Ahuja, K.K., and Chambers, F.W., "Prediction and Measurement of Flows Over Cavities - A Survey," AIAA-87-0166, Jan. 1987.

[42] Rockwell, D. and Naudascher, E., "Review – Self-Sustaining Oscillations of Flow Past Cavities," *Transactions of the ASME,* 100, June 1978, pp. 152-165.

[43] Gilbert, K., "KC-135 Aero-Optical Turbulent Boundary Layer/Shear Layer Measurements," *Aero-Optical Phenomena,* Vol. 80, Progress in Astronautics Aeronautics, AIAA, New York, 1982.

[44] Stine, H.A. and Winovich, W., "Light Diffusion Through High-Speed Turbulent Boundary Layers,"NACA RM-A56B21, 1956.

[45] Sutton, G.W., "Effect of Turbulent Fluctuations in an Optically Active Fluid Medium," *AIAA J.,* Vol. 7, Sep. 1969, pp. 1737-1743.

[46] Sutton, G.W., "Aero-optical Foundation and Applications," *AIAA J.,* Vol. 23, Oct. 1985, pp. 1525-1537.

[47] Truman, C.R. and Lee, M-J., "Effects of organized turbulence structures on the phase distortion in a coherent optical beam propagating through a turbulent shear flow," *Phys. Fluids A,* Vol. 2, May 1990, pp. 851-857.

[48] Brown, G.L. and Roshko, A., "On density effects and large structure in turbulent mixing layers," *J. Fluid Mech.,* Vol. 64, Part 4, 1974, pp. 775-816.

[49] Chew, L. and Christiansen, W., "Coherent Structure Effects on the Optical Performance of Plane Shear Layers," *AIAA J.,* Vol. 29, Jan. 1991, pp. 76-80.

[50] Chew, L. and Christiansen, W., "Experimental Investigation of Free Shear Layer Optics," AIAA-91-1722, June 1991.

[51] Tsai, Y.P. and Christiansen, W.H., "Two-Dimensional Numerical Simulation of Shear-Layer Optics," *AIAA J.,* Vol. 28, Dec. 1990, pp. 2092-2097.

[52] Wissler, J.B. and Roshko, A., "Transmission of Thin Light Beams Through Turbulent Mixing Layers," AIAA-92-0658, Jan. 1992.

[53] Cassady, P., Birch, S.F., and Terry, P.J., "Aero-Optical Analysis of Compressible Flow Over An Open Cavity," AIAA-87-1399, June 1987.

[54] Clark, R.L. and Farris, R.C., "A Numerical Method to Predict Aero-Optical Performance in Hypersonic Flight," AIAA-87-1396, June 1987.

[55] Farris, R.C. and Clark, R.L., "An Integrated Navier-Stokes and Wave Optics Numerical Simulation Technique for Predicting the Aero-Optical Performance about Subsonic Surveillance Aircraft," AIAA-88-0753, Jan. 1988.

[56] Spreiter, J.R., "Lecture Notes in Fluid Mechanics," Stanford Univ., 1989.

[57] MacCormack, R.W., "Lecture Notes on the Numerical Computation of Compressible Viscous Flow," Stanford Univ., Jan. 1986.

[58] Buning, P.G. and Chan, W.M., "OVERFLOW/F3D User's Manual, Version 1.5," NASA/ARC, Nov. 1990.

[59] Birch, S.F. and Eggers, J.M., "A Critical Review of the Experimental Data for Developed Free Turbulent Shear Layers," *Free Turbulent Shear Flows,* NASA SP-321, July 1972.

[60] Liepmann, H.W. and Laufer, J., "Investigations of Free Turbulent Mixing," NACA TN-1257, 1947.

[61] Vinokur, M., "An Analysis of Finite-Difference and Finite-Volume Formulations of Conservation Laws," NASA CR-177416, June 1986.

[62] Steger, J.L., "Implicit Finite-Difference Simulation of Flow about Arbitrary Two-Dimensional Geometries,"*AIAA J.,* Vol. 16, July 1978, pp. 679-686.

[63] Warming, R.F., Beam, R.M., and Hyett, B.J., "Diagonalization and Symmetrization of the Gas-Dynamic Equations," *Math. Comp.,* Vol. 29, Oct. 1975, pp. 1037-1045.

[64] Steger, J.L. and Warming, R.F., "Flux Vector Splitting of the Inviscid Gasdynamic Equations with Application to Finite-Difference Methods," *J. Comp. Phys.,* Vol. 40, 1981, pp. 263-293.

[65] Barth, T.J., "Analysis of Implicit Local Linearization Techniques for Upwind and TVD Algorithms," AIAA-87-0595, Jan. 1987.

[66] Godunov, S.K., "Difference Method of Numerical Computation of Discontinuous Solutions of Hydrodynamic Equations," *Mat. Sb.,* Vol. 47, 1959, pp. 271-306.

[67] Roe, P.L., "Approximate Riemann Solvers, Parameter Vectors, and Difference Schemes," *J. Comp. Phys.,* Vol. 43, 1981, pp. 357-372.

[68] Chakravarthy S.R. and Osher, S., "High Resolution Applications of the Osher Upwind Scheme for the Euler Equations," AIAA-83-1943, June 1983.

[69] Chakravarthy, S.R., "A New Class of High Accuracy TVD schemes for Hyperbolic Conservation Laws," AIAA-85-0363, Jan. 1985.

[70] Yanenko, N.N., *The Method of Fractional Steps: The Solution of Problems of Mathematical Physics in Several Variables,* (M. Holt, ed.), Springer-Verlag, New York, 1971.

[71] Chakravarthy, S.R., "Relaxation Methods for Unfactored Implicit Upwind Schemes," AIAA-84-0165, Jan. 1984.

[72] Benek, J.A., Buning, P.G., and Steger, J.L., "A 3-D Chimera Grid Embedding Technique," AIAA-85-1523, July 1985.

[73] Pulliam, T.H. and Chaussee, D.S., "A Diagonal Form of an Implicit Approximate-Factorization Algorithm," *J. Comp. Phys.*, Vol. 39, Feb. 1981, pp. 347-363.

[74] Rai, M.M. and Chakravarthy, S.R., "An Implicit Form for the Osher Upwind Scheme," *AIAA J.,* Vol. 24, May 1986, pp. 735-743.

[75] Rogers, S.E. and Kwak, D., "An Upwind Differencing Scheme for the Time-Accurate Incompressible Navier-Stokes Equations," AIAA-88-2583, June 1988.

[76] Thompson, J.F., Thames, F.C., and Mastin, W.C., "Automatic Numerical Generation of Body-Fitted Curvilinear Coordinate System for Field Containing Any Number of Arbitrary Two-Dimensional Bodies," *J. Comp. Phys.*, Vol. 15, 1974, pp. 299-319.

[77] Thomas, P.D. and Middlecoff, J.F., "Direct Control of Grid Point Distribution in Meshes Generated by Elliptic Equations," *AIAA J.*, Vol. 18, June 1980, pp. 652-656.

[78] Steger, J.L. and Sorenson, R.L., "Automatic Mesh-Point Clustering Near a Boundary in Grid Generation with Elliptic Partial Differential Equations," *J. Comp. Phys.*, Vol. 33, 1979, pp. 405-410.

[79] Steinbrenner, J.P., Chawner, J.R., and Fouts, C.L., "A Structured Approach to Interactive Multiple Block Grid Generation," AGARD FDP Specialists Mtg. on Mesh Generation for Complex Three-Dimensional Configurations, Loen, Norway, May 1989.

[80] Chan, W.M. and Steger, J.L., "A Generalized Scheme for Three-Dimensional Hyperbolic Grid Generation," AIAA-91-1588, June 1991.

[81] Atwood, C.A. and Vogel, J.M., "Surface Grid Generation for Flowfield Applications Using B-Spline Surfaces," AIAA-89-2177, Aug. 1989.

[82] Merriam, M.L. and Barth, T.J., "3-D CFD in a Day: The Laser Digitizer Project," AIAA-91-1654, June 1991.

[83] Vaillancourt, K., Private communication.

[84] Parks, S.J., Buning, P.G., Steger, J.L., and Chan, W.M., "Collar Grids for Intersecting Geometric Components within the Chimera Overlapped Grid Scheme," AIAA-91-1587, June 1991.

[85] MacCormack, R.W., "Current Status of Numerical Solutions of the Navier-Stokes Equations," AIAA-85-0032, Jan. 1985.

[86] Kordulla, W. and Vinokur, M., "Efficient Computation of Volume in Flow Prediction," *AIAA J.*, Vol. 21, June 1983, pp. 917-918.

[87] Mortenson, M.E., *Geometric Modeling,* John Wiley and Sons, New York, 1985.

[88] Clark, T.T., Truman, C.R., and Masson, B.S., "Optical Propagation through Computational Turbulence Using a Parabolized Helmholtz Equation," AIAA-88-3663, July 1988.

[89] Schlichting, H., *Boundary Layer Theory,* McGraw-Hill, New York, 1979.

[90] Amann, H.O., "Vorgänge beim Start einer ebenen Reflexionsdüse," *Z. Flugwiss,* Vol. 19, 1971, pp. 393-406.

[91] Kingery, C.N. and Bulmash,G., "Effects of Shock Tube Blockage on Target Loading," BRL-TR-2689, Nov. 1985.

[92] Buning, P.G. and Steger, J.L., "Graphics and Flow Visualization in Computational Fluid Dynamics," AIAA-85-1507-CP, July 1985.

[93] Bulmash, G., Private communication.

[94] Hahn, M.M., "Flight Test Verification of the Aerodynamic Characteristics of the 767-AOA Open Viewports," Boeing Commercial Airplane Company, Doc. D041T207TN, Fall 1987.

[95] Hussain, A.K.M.F. and Zaman, K.B.M.Q., "An experimental study of organized motions in the turbulent plane mixing layer," *J. Fluid Mech.,* Vol. 159, 1985, pp. 85-104.

[96] Oster, D. and Wygnanski, I., "The forced mixing layer between parallel streams," *J. Fluid Mech.,* Vol. 123, 1982, pp. 91-130.

[97] Winant, C.D. and Browand, F.K., "Vortex pairing: the mechanism of turbulent mixing-layer growth at moderate Reynolds number," *J. Fluid Mech.,* Vol. 63, 1974, pp. 237-255.

[98] Roberts, F.A. and Roshko, A., "Effects of Periodic Forcing on Mixing in Turbulent Shear Layers and Wakes," AIAA-85-0570, Mar. 1985.

[99] Bogdanoff, D.W., "Compressibility Effects in Turbulent Shear Layers," *AIAA J.*, Vol. 21, June 1983, pp. 926-927.

[100] Rockwell, D., "Oscillations of Impinging Shear Layers," AIAA-82-0047, Jan. 1982.

[101] Rubin, D.V. and Walker, B.J., "AOA Aero-Optical Wind Tunnel Test Final Analysis Report," Technical Report RD-SS-86-8, U.S. Army Missile Command, Feb. 1986.

[102] Roscoe, D.F. and Hankey, W.L., "The Stability of a Compressible Free Shear Layer," AFWAL-TR-80-3016, Oct. 1979.

[103] Bogdanoff, D.W., "The Optical Quality of Shear Layers: Prediction and Improvement Thereof," *AIAA J.*, Vol. 22, Jan. 1984, pp. 58-64.

[104] Rose, W.C. and Johnson, D.A., "Unsteady Density and Velocity Measurements in the $6' \times 6'$ Wind Tunnel," Proceedings of the Aero-Optics Symposium on Electromagnetic Wave Propagation from Aircraft, NASA CP-2121, Aug. 1979, pp. 153-181.

[105] Cebeci, T. and Smith, A.M.O., *Analysis of Turbulent Boundary Layers,* Academic Press, New York, 1974.

[106] Johnson, D.A. and Rose, W.C., "Turbulence Measurement in a Transonic Boundary Layer and Free-Shear Flow Using Laser Velocimetry and Hot-Wire Anemometry Techniques," AIAA-76-399, July 1976.

[107] Raman, K.R., "Pressure and Temperature Fields Associated with Aero-Optics Tests," Proceedings of the Aero-Optics Symposium on Electromagnetic Wave Propagation from Aircraft, NASA CP-2121, Aug. 1979, pp. 91-121.

[108] Haslund, R.L.,"SOFIA Viewport Configuration Wind Tunnel Test Report," Boeing Aerospace and Electronics Sensors Technology, Oct. 1988.

# REPORT DOCUMENTATION PAGE

*Form Approved*
*OMB No. 0704-0188*

| | | |
|---|---|---|
| **1. AGENCY USE ONLY** ***(Leave blank)*** | **2. REPORT DATE**<br>August 1992 | **3. REPORT TYPE AND DATES COVERED**<br>Technical Memorandum |

**4. TITLE AND SUBTITLE**

Navier-Stokes Simulations of Unsteady Transonic Flow Phenomena

**5. FUNDING NUMBERS**

505-59

**6. AUTHOR(S)**

C. A. Atwood

**7. PERFORMING ORGANIZATION NAME(S) AND ADDRESS(ES)**

Ames Research Center
Moffett Field, CA 94035-1000

**8. PERFORMING ORGANIZATION REPORT NUMBER**

A-92159

**9. SPONSORING/MONITORING AGENCY NAME(S) AND ADDRESS(ES)**

National Aeronautics and Space Administration
Washington, DC 20546-0001

**10. SPONSORING/MONITORING AGENCY REPORT NUMBER**

NASA TM-103962

**11. SUPPLEMENTARY NOTES**

Point of Contact: C. A. Atwood, Ames Research Center, MS T045-2, Moffett Field, CA 94035-1000
(415) 604-3974

**12a. DISTRIBUTION/AVAILABILITY STATEMENT**

Unclassified — Unlimited
Subject Category 02

**12b. DISTRIBUTION CODE**

**13. ABSTRACT** ***(Maximum 200 words)***

Numerical simulation of two classes of unsteady flows are obtained via the Navier-Stokes equations: a blast-wave/target interaction problem class and a transonic cavity flow problem class. The method developed for the viscous blast-wave/target interaction problem assumes a laminar, perfect gas implemented in a structured finite-volume framework. The approximately factored implicit scheme uses Newton subiterations to obtain the spatially and temporally second-order accurate time history of the interaction of blast-waves with stationary targets. The inviscid flux is evaluated using either of two upwind techniques, while the full viscous terms are computed by central differencing. Comparisons of unsteady numerical, analytical, and experimental results are made in two- and three-dimensions for Couette flows, a starting shock-tunnel, and a shock-tube blockage study. The results show accurate wave speed resolution and nonoscillatory discontinuity capturing of the predominantly inviscid flows. Viscous effects were increasingly significant at large post-interaction times.

While the blast-wave/target interaction problem benefits from high-resolution methods applied to the Euler terms, the transonic cavity flow problem requires the use of an efficient scheme implemented in a geometrically flexible overset mesh environment. Hence, the Reynolds averaged Navier-Stokes equations implemented in a diagonal form are applied to the cavity flow class of problems. Comparisons between numerical and experimental results are made in two-dimensions for free shear layers and both rectangular and quieted cavities, and in three-dimensions for Stratospheric Observatory For Infrared Astronomy (SOFIA) geometries. The acoustic behavior of the rectangular and three-dimensional cavity flows compare well with experiment in terms of frequency, magnitude, and quieting trends. However, there is a more rapid decrease in computed acoustic energy with frequency than observed experimentally owing to numerical dissipation. In addition, optical phase distortion due to the time-varying density field is modelled using geometrical constructs. The computed optical distortion trends compare with the experimentally inferred result, but underpredicts the fluctuating phase difference magnitude.

**14. SUBJECT TERMS**

Optics, Cavity, Blast waves

**15. NUMBER OF PAGES**

130

**16. PRICE CODE**

A07

| | | | |
|---|---|---|---|
| **17. SECURITY CLASSIFICATION OF REPORT**<br>Unclassified | **18. SECURITY CLASSIFICATION OF THIS PAGE**<br>Unclassified | **19. SECURITY CLASSIFICATION OF ABSTRACT** | **20. LIMITATION OF ABSTRACT** |

NSN 7540-01-280-5500

Standard Form 298 (Rev. 2-89)
Prescribed by ANSI Std Z39-18